

Development of a method to measure the
polarization of laser-accelerated protons

Inaugural-Dissertation

zur

Erlangung des Doktorgrades

der Mathematisch-Naturwissenschaftlichen Fakultät

der Universität Köln

vorgelegt von

Natascha Raab

aus Bonn

Berichterstatter:
(Gutachter)

Priv.-Doz. Dr. Markus Büscher

Prof. Dr. Jan Jolie

Tag der mündlichen Prüfung: Freitag, der 15. April 2011

Zusammenfassung

Im Rahmen dieser Arbeit wurden Messungen und Simulationsstudien zu Polarisationsobservablen von Laser-induzierten Teilchenstrahlen durchgeführt. Diese Untersuchungen wurden mit dünnen Folientargets die, mit 100 TW Laserpulsen am ARCTurus Laserlabor der Heinrich-Heine Universität Düsseldorf bestrahlt, als Quelle für Protonenstrahlen von einigen MeV kinetischer Energie dienen.

Mit *Particle-in-Cell* Simulationen wurde der Einfluss der magnetischen Feldgradienten, die im Laser-induzierten Plasma vorliegen auf die Teilchentrajektorien untersucht. Es zeigte sich, dass die Ablenkung der Protonen durch eine Stern-Gerlach artige Wechselwirkung mit den magnetischen Feldgradienten vernachlässigbar klein und keine Auffächerung des Protonstrahles nach Spinzuständen zu erwarten ist.

Messungen des Energiespektrums der erzeugten Protonen wurden durchgeführt, hierzu wurde ein Dipolmagnet für ein magnetisches Spektrometer entworfen und gebaut.

Die experimentelle Methode für die Messung der Spin-Polarisation des Protonenstrahls wurde mit Hilfe von Monte-Carlo Simulationen entwickelt und optimiert. Grundlage ist die Spinabhängigkeit der hadronischen Streuung der Strahlteilchen an Kernen in einem Streutarget. Die Realisierbarkeit des Experiments wurde in einem Null-Experiment mit dem unpolarisierten Protonenstrahl demonstriert.

Abstract

In the framework of this thesis first measurements and simulation studies on polarization observables of laser-accelerated charged particle beams were performed. These investigations were carried out with thin foil targets, that were illuminated by 100 TW laser pulses at the ARCturus laser facility at Heinrich Heine University in Düsseldorf, which serve as a source for few MeV proton beams.

With Particle-in-Cell simulations the influence of the huge magnetic field gradients, that are inherently present in laser-induced plasmas, on particle trajectories has been modeled. It was found, that the deflection of the protons by a Stern-Gerlach like interaction with the magnetic field gradients is negligibly small and that no spatial separation of the protons according to their spin states is to be expected.

Measurements of proton energy spectra have been carried out with a spectrometer dipole that was specifically designed for this purpose.

The experimental method for the measurement of the spin-polarization of the proton beam was developed and optimized with the help of Monte-Carlo simulations. It is based on the spin dependency of hadronic proton scattering off nuclei in a scattering target. The feasibility of the method was demonstrated in a null-experiment with the supposedly unpolarized proton beams.

Contents

1. Introduction and motivation	9
1.1. Conventional and laser-driven accelerators	9
1.2. Search for polarization effects	11
1.3. Scope of the thesis	12
2. Laser-induced particle acceleration	13
2.1. Lasers as intense light sources	13
2.2. Interaction with matter	15
2.2.1. Ionization	16
2.2.2. Interaction with single electrons	17
2.2.3. Interactions in a target, particle acceleration	21
Electron accelerating mechanisms	22
Ion accelerating mechanisms	23
3. Spin and polarization	25
3.1. Spin formalism	25
3.2. Manipulation of particle spins	28
3.3. Stern-Gerlach effect and atomic beam source	28
3.4. Observation	31
3.5. Particles with spin in laser-plasma interactions	34
4. Experimental methods	37
4.1. Particle-in-Cell Simulations and the program BOPS	37
4.2. Analyzer target	38
4.3. The simulation toolkit Geant4	40
4.4. Detectors	44
4.4.1. RadioChromic Film detectors	44
4.4.2. CR-39 detectors	46
4.5. Magnetic spectrometer	51
4.5.1. Design and assembling of the dipole magnet	52
4.5.2. Field measurements and calibration	53

5. Düsseldorf laser facility ARcturus	55
5.1. Laser system	55
5.2. Target chambers	56
5.3. Proton production	57
6. Particle-in-Cell simulations	61
6.1. Methods and input parameters	61
6.2. Results	63
7. Spin polarization measurement	65
7.1. Setup	65
7.2. Simulations	67
7.3. Results of the first measurement	69
7.3.1. Processing the data from the CR-39 detectors	70
7.3.2. Raw data	70
7.3.3. Energy selection	72
7.3.4. Determination of the distribution center	73
7.3.5. Determination of proton rates and calculation of cross sections	75
7.3.6. Azimuthal angle asymmetries	80
7.4. Conclusion	86
8. Summary and outlook	87
A. Measurements April 2010	97

1. Introduction and motivation

1.1. Conventional and laser-driven accelerators

By directing a high-intense laser beam on a foil or a gas jet it is possible to ignite a plasma in the focus point. Electrons and ions can be accelerated from such a plasma target. In recent years, the physics of laser-induced particle acceleration has undergone a vast development. Since the possibility of laser-induced charged-particle acceleration was discovered, the potential of laser-based electron and ion sources for applications like imaging [1], hadron therapy [2], nuclear fusion [3] and high-brightness injectors for conventional accelerators [4] provided for a high surge of interest.

The sheer size of the conventional accelerators as well as the necessary maintenance renders it impossible to run such systems outside of research centres, much less to serialize the technology for an comprehensive use of the possible applications. High intense laser systems, on the other hand, are commercially available, less space-consuming and less demanding regarding maintenance.

Also, conventional accelerator technology is about to reach fundamental and technological limits of the achievable particle energies. Figure 1.1 depicts the Livingston plot of the development of conventional particle accelerators extended by plasma based particle sources and their maximum achieved electron energies. The first linear accelerator was build by Wideröe in 1927 that was able to accelerate sodium and potassium ions to 50 keV, by using RF electric fields [6]. Since then the technology of particle acceleration has evolved rapidly, the cyclotron and synchrotron technologies have been invented and improved. The current peak is reached with the LHC at CERN¹. Although cyclic accelerators have the advantage to repeatedly accelerate particles with the same acceleration unit, synchrotron-radiation losses limit the maximum energy for lepton beams. Therefore, the next lepton accelerator will be a linear collider [7, 8].

In case of hadron colliders the radiation losses are negligible at this point in time, since the synchrotron radiation is inversely proportional to the mass of the beam particles to the power four, but the magnetic field strengths of the dipole magnets

¹Large Hadron Collider at the Conseil Européen pour la Recherche Nucléaire, European Organization for Nuclear Research in Geneva, Switzerland

1. Introduction and motivation

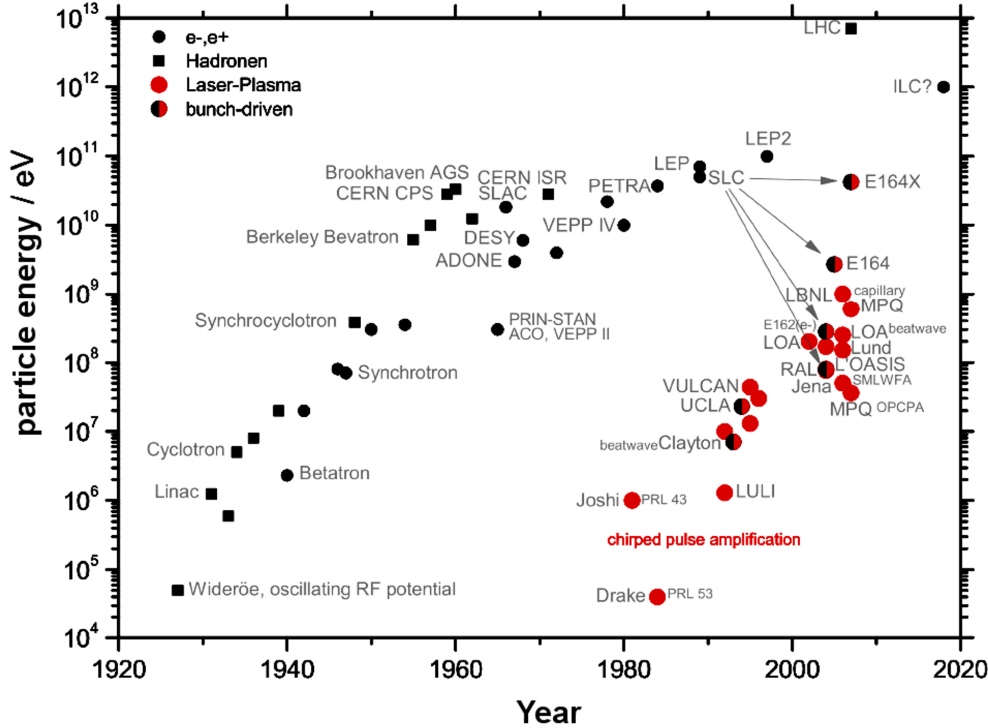


Figure 1.1.: Livingston plot for conventional accelerators (black dots), as well as plasma driven particle sources (red dots) [5].

that are needed to force the beam on a closed orbit are huge. The technical boundaries given by the limit of the field strengths that are achievable can be pushed forward by building storage rings of bigger diameter, but the LHC has already enormous dimensions with a circumference of 27 km.

Those limitations do not apply to laser-driven particle acceleration and since the invention of the so-called chirped pulse amplification laser intensities and, therefore, the possible electron energies have increased rapidly into the GeV regime. For protons the maximum energy up-to-date is 67.5 MeV, produced in the Trident Laser Laboratory in Los Alamos [9].

Fundamental and technological challenges still have to be mastered for the realization of reliable and continuously operating “table-top” accelerators. The particle beams typically are poly-energetic with a broad angular distribution. The repetition rate of high intense lasers is limited to about 10 Hz which also sets limits to the luminosity of these accelerators.

While the development of laser-induced particle accelerators is rigorously driven forward, it is yet a completely untouched issue whether the laser-generated beams are or can be spin-polarized. Since many high-energy and nuclear-physics experiments require polarized beams it is vital to investigate this possibility.

1.2. Search for polarization effects

Since every particle with spin carries a magnetic moment the spin direction can be manipulated with magnetic fields, while the trajectories can be influenced through magnetic field gradients. Therefore, there are two potential mechanisms that might cause a polarization of a particle beam from a plasma source: either due to spin alignment by the huge magnetic fields that are inherently generated in the plasma or by selection of certain spin states through the field gradients. The second scenario would make use of the same principle as in the seminal experiment by O. Stern and W. Gerlach in the year 1922, when they discovered the spin of electrons bound in electrically neutral atoms, by separating a beam of silver atoms according to the spin state of the valence electron in an inhomogeneous magnetic field [10].

At the Copenhagen conference in the year 1929 however, Bohr raised the question, whether it is possible to measure the spin of a free electron in the same way [11]. Based on the uncertainty principle he finally concluded, that electron spin states

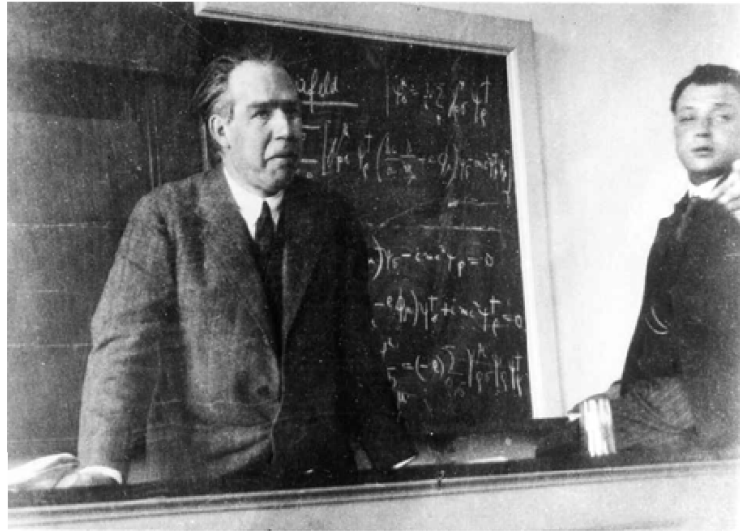


Figure 1.2.: Niels Bohr and Wolfgang Pauli. Taken during the Copenhagen conference of April 1929 (Niels Bohr Archive, Copenhagen).

cannot be spatially separated by a magnetic force acting on the dipole moment. The uncertainty introduced by the smearing of the Lorentz force, which in turn is caused by the field gradient, on the moving particle is in the same order of magnitude as the dividing force of the field gradients. In principle this should apply to all charged particles [12].

In 2002 Garraway and Stenholm showed, that it is in principle possible to achieve spin-separation for charged particles under certain conditions like a small diameter of the particle beam in the field region and a sufficiently long propagation time in

1. Introduction and motivation

an interaction free region afterwards [11] — conditions that may be fulfilled in laser-plasma experiments.

Up to the present, neither with simulations nor experimentally, it has been investigated, whether the conditions during laser-induced acceleration meet the requirements leading to an observable spin-separation. To reverse this argument, an observation of polarized beams from laser-induced plasmas could settle the long-standing discussion whether the Stern-Gerlach effect is observable also for charged particles. Another potential possibility to realize laser-driven polarized particle sources is the use of pre-polarized targets. Since the high electric field strengths of the laser-pulse lead to a rapid ionization of the material, the prospects are good that the nuclear spin is maintained during the process of ionization and acceleration.

1.3. Scope of the thesis

The main steps aiming at a clarification of the above mentioned challenges are outlined in this PhD thesis, which is structured as follows:

First it is investigated theoretically, whether laser-generated proton beams from solid targets are expected to be spin-separated by a Stern-Gerlach like effect and whether this effect is detectable. With the one-dimensional Particle-in-Cell code BOPS (Boosted Oblique Particle Simulation) the plasma target is simulated on the parallel processor JuRoPA (Jülich Research on Petaflop Architectures) of the Jülich Supercomputing Centre and the angular deflection caused by the magnetic field gradients is calculated.

Secondly, a method is developed to measure the polarization of laser-accelerated protons at the Düsseldorf ARCturus laser facility. This method is based on the spin dependence of hadronic proton scattering off nuclei in a suitable target. As a basis for the design of the setup, the proton energy spectrum had to be measured with a dipole spectrometer that was built specifically for this purpose. To make optimal use of the spin dependence of hadronic interactions, different potential materials for the scattering target need to be compared and the experimental setup it is modeled with the simulation toolkit Geant4 (GEometry ANd Tracking) for optimization of the setup geometry.

Finally, a first measurement is carried out and the analysing methods are developed.

2. Laser-induced particle acceleration

2.1. Lasers as intense light sources

Since the first functional laser¹ was built in 1960 [13], the achievable laser intensities have increased steadily. Figure 2.1 shows how the achievable focus intensity advanced over the years. The invention of Q-switching in 1961 made the pulsed operation of lasers possible and allowed the peak power to be much higher than it would be in continuous wave mode. With a Q-switch (for example an electro-optical device) the pulse is prevented from leaving the gain material until the desired amount of energy is stored in the laser medium. The pulse that is then released has a duration of several tens of nanoseconds and a peak power that is three orders of magnitude higher than the average power in continuous wave mode, values of watts and kilowatts are usual. This invention started the first rapid increase of achievable intensity and was shortly followed by the invention of the technique of mode-locking, that allowed pulse durations as short as a few ps at that time, which has been improved to less than 10 fs today. Basic principle of the method of mode-locking is the synchronization of the frequency modes, which leads to interference between them and subsequently produces a chain of regular pulses. The continuous light that is still emitted with a lower intensity is suppressed by using nonlinear effects that start to occur at high intensities. With dispersive optical elements the beam in the medium is defocused. For high intensities however, the intensity dependence of the refractive index, the Kerr non linearity, which occurs for $I > 10^{11} \text{ Wcm}^{-2}$, leads to a distortion of the wavefront and self-focusing, that compensates the defocusing if the light exceeds a certain intensity limit. The crystal acts as a nonlinear focusing lens and higher intensities get focused stronger than lower. Pulses of ps were feasible with this technique, which increased the achievable intensity by an order of magnitude.

Today less than ten fs of pulse duration can be produced with Ti:sapphire lasers. The pulse duration is limited by the bandwidth: $\tau \approx 1/\Delta\nu$. Since Ti:sapphire is the material with the broadest bandwidth, it is preferably used for the production of ultra-short pulses. While for the technique of mode-locking self-focusing can be utilized, these nonlinear effects limit the intensity of the laser light that can safely

¹the well-known acronym for light amplification by stimulated emission of radiation

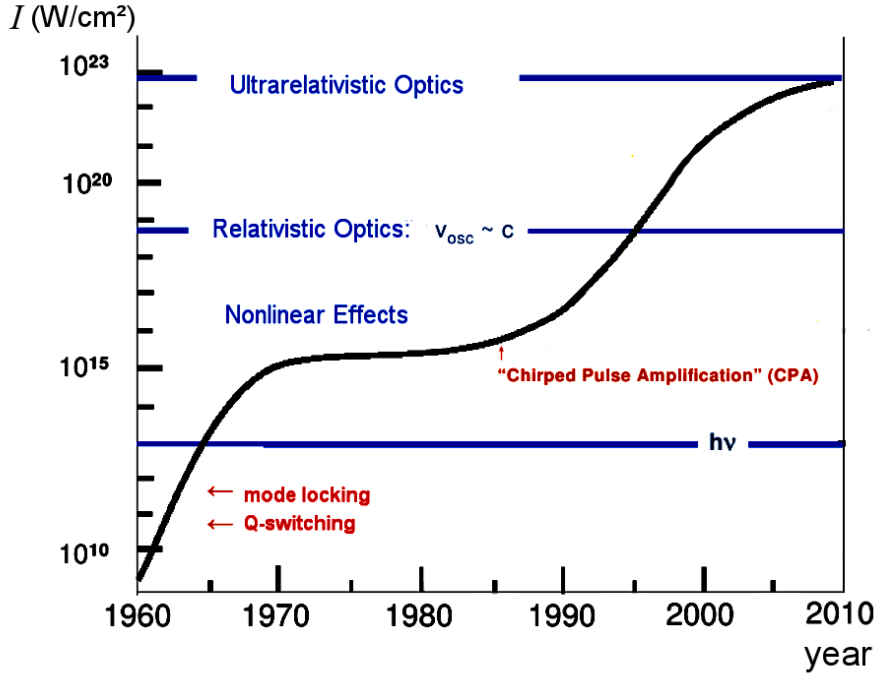


Figure 2.1.: Advancement of focused laser intensity since 1960 [14].

pass the amplifier. At intensities of more than 10^{12} Wcm^{-2} both self-focusing and beam filamentation become strong enough to deteriorate the beam quality or even damage the amplifier material. Temperature dependency of the refractive index of the material leads to the thermal lens effect, since the gain medium is hotter on the beam axis, which leads to a gradient of the refractive index.

Tera watt pulses could only be achieved by largely increasing the beam diameter and therefore the costs for the optical instrumentation. The technical limit to the extension of gratings for example is about 1 meter in diameter [15]. For this reason the advance of focused laser intensity reached a plateau in the beginning of the nineteen-eighties.

Chirped Pulse Amplification

A solution was found in 1985 by Gerard Mourou *et. al* [14], with the invention of *Chirped Pulse Amplification* (CPA). Figure 2.2 depicts the principle of this technique schematically. Starting point for this method is an initial short pulse with low energy of about a few nJ of energy. Before the pulse passes the amplifier medium it is stretched temporally by means of dispersive elements like gratings. While the energy remains constant, the peak power is reduced. The intensity of the stretched

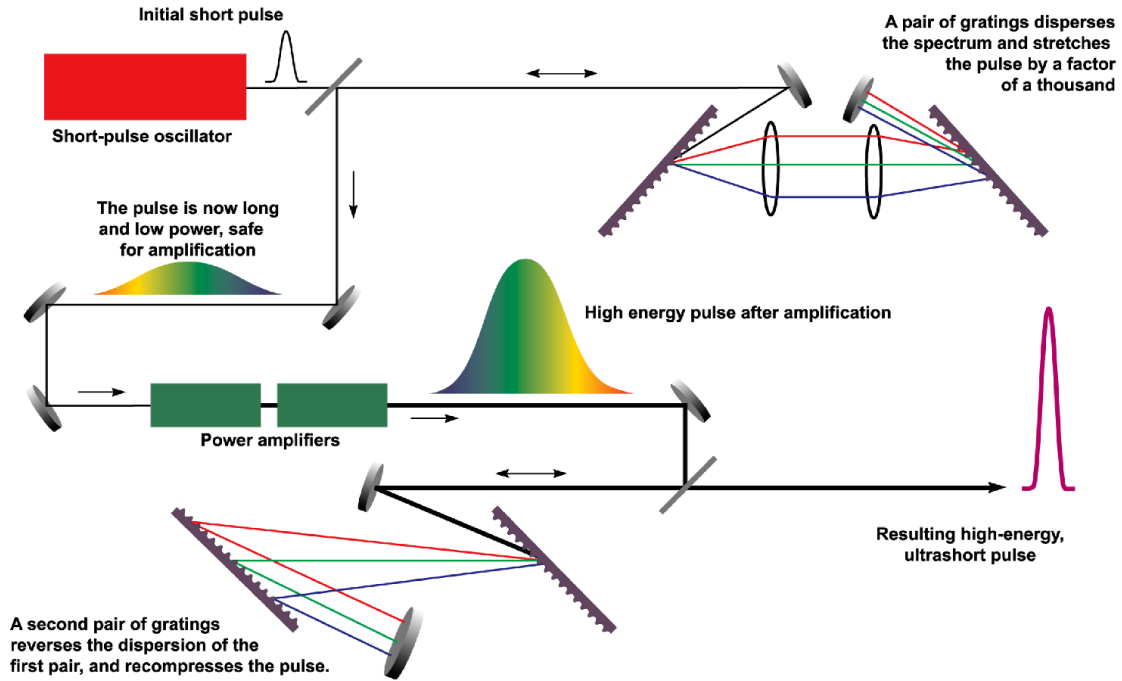


Figure 2.2.: Principle of chirped pulse amplification [14].

pulse is sufficiently far below the threshold of nonlinear effects to safely amplify the pulse by a factor of $\approx 10^6$ and the pulse can be amplified using standard techniques for the amplifier chain. After this, the process of stretching is reversed, and the pulse is compressed again temporally to a duration slightly above originally emitted by the oscillator. The result is a peak power of the final pulse that cannot pass any medium, including air, without self-focusing or even forming a plasma for which reason compressor and beam line have to be evacuated. Usual peak intensities after compression are at about hundred TW, although PW are possible. CPA is the key technique in almost every high-intensity laser system today.

2.2. Interaction with matter

When directing a high-intense ultra-short laser pulse on a target a plasma is produced in the focus. During the following interaction of laser and plasma, particles are expelled from the target. It is distinguished between overdense and underdense plasma. The former is produced when solid targets, like foils or pellets are used, the latter in case of gas jet or liquid targets. In both cases electrons get expelled from the target first, by the direct interaction between the electro-magnetic fields of the laser light with the electrons. In case of solid targets protons that are either part of the material or of impurities on the surface are accelerated in the quasi-static

2. Laser-induced particle acceleration

field that is generated by the lack of electrons. Usually in an underdense plasma higher electron energies are obtained, while solid targets are more suitable to accelerate ions. A short look on different ionization mechanisms will be followed by the interaction with single quasi-free electrons.

2.2.1. Ionization

Clearly at laser wavelengths in the infrared region the energy of the photons is too small to induce single-photon ionization. If the electric field of the laser light on the other hand matches the binding energy of the atom it is ionized instantly. The required intensity to fulfil this condition is the *atomic intensity* I_a , that provides the same field strength as is (classically) present in the hydrogen atom at the distance of 1 Bohr radius a_B^2 to the nucleus:

$$E_a = \frac{e}{4\pi\epsilon_0 a_B^2} \approx 5.1 \cdot 10^{11} \frac{\text{V}}{\text{m}} \quad \longrightarrow \quad I_a = \frac{\epsilon_0 c}{2} E_a^2 \approx 3.45 \cdot 10^{16} \frac{\text{W}}{\text{cm}^2},$$

where ϵ_0 is the vacuum permittivity and e the elementary charge.

While the atomic intensity guarantees ionization in any case, the threshold is lowered by other effects, namely multiphoton ionization, tunnel ionization and barrier suppression ionization. It is also interesting to know how many electrons will be stripped of the atom.

Multiphoton Ionization and Above Threshold Ionization

Multiphoton Ionization is the process in which several photons of the energy $E_{\text{ph}} = \hbar\omega$ are absorbed to provide the electron with enough energy to leave the coulomb potential of the atom. The time frame in which the photons have to encounter the atom is limited by the uncertainty principle to $\Delta t = 1/\omega$. Therefore, a high number of photons have to be provided to increase the probability. The cross section for this process σ_n may decrease with the number n of photons that need to be absorbed, but the ionization rate increases with I^n . If more photons are absorbed than strictly necessary this is termed *Above Threshold Ionization*, in which case the electron gains the kinetic energy of $E_{\text{kin}} = (n+m) \cdot \hbar\omega - E_{\text{ion}}$, where m is the number of photons, that are absorbed additionally. Both processes tend to dominate for shorter wavelengths, lower intensities and longer pulse duration.

Barrier Suppression Ionization and Tunnel Ionization

For strong fields and very long wavelength the processes of tunnel ionization becomes important, which can be described as the modification of the coulomb potential with a constant electric field. The model that forms the basis of *Barrier Suppression*

Ionization was developed by Bethe and Salpeter [16]. The atomic binding potential is distorted by the electric field of the laser. Figure 2.3 shows the superposition of the atomic potential and a constant external field.

$$V(x) = -\frac{Ze^2}{x} - eEx .$$

With this one can derive an *appearance intensity* that belongs to the electric field at which ions of a the charge Z start to appear:

$$E_{\text{crit}} = \frac{E_{\text{ion}}^2}{4Ze^2} \longrightarrow I_{\text{BSI}} = \frac{\pi^2 c \epsilon_0^3 E_{\text{ion}}^4}{2Z^2 e^6} .$$

At this intensity the barrier is suppressed completely and the electron can escape. Experiments have confirmed this relation for several noble gases, for example even the Xe^{8+} has an appearance intensity of less than 10^{16} Wcm^{-2} . If the external field is not strong enough to suppress the barrier completely the atomic potential can still be distorted so much that the electron is able to tunnel through the barrier. For this process longer wavelengths are preferable, so that the electron “has enough time” to tunnel. Using this model, ionization rates can be derived by calculating the tunnel probability quantum mechanically. Calculations were carried out by Keldysh [17] and Perelomov [18, 19]. So for intensities of more than 10^{18} Wcm^{-2} it can be assumed that the material in the focus region is ionized instantly and all valence electrons and even more are stripped from the atoms.

The ionization rates for complex atoms and ions are given by [21] :

$$N(t) = 1 - \exp\left(-\int_{-\infty}^t \Gamma(\tau) d\tau\right) .$$

Γ being the ionization rate and N the number of electrons produced until a time t . This is well confirmed for noble gases.

One can assume, that the main pulse interacts with ionized matter, and use the case of a single free electron as a starting point.

2.2.2. Interaction with single electrons

After an electron has been released from the atom the motion in the electromagnetic field of the laser light is described by the Lorentz equation:

$$\frac{d\vec{p}}{dt} = -e(\vec{E} + \frac{\vec{v}}{c} \times \vec{B}) .$$

In the non relativistic scenario the magnetic component can be neglected and a plane and linearly polarized electromagnetic wave traveling in x-direction, described by

$$\vec{E} = E_0 \cdot \cos(\omega t - kx) \vec{e}_y ,$$

2. Laser-induced particle acceleration

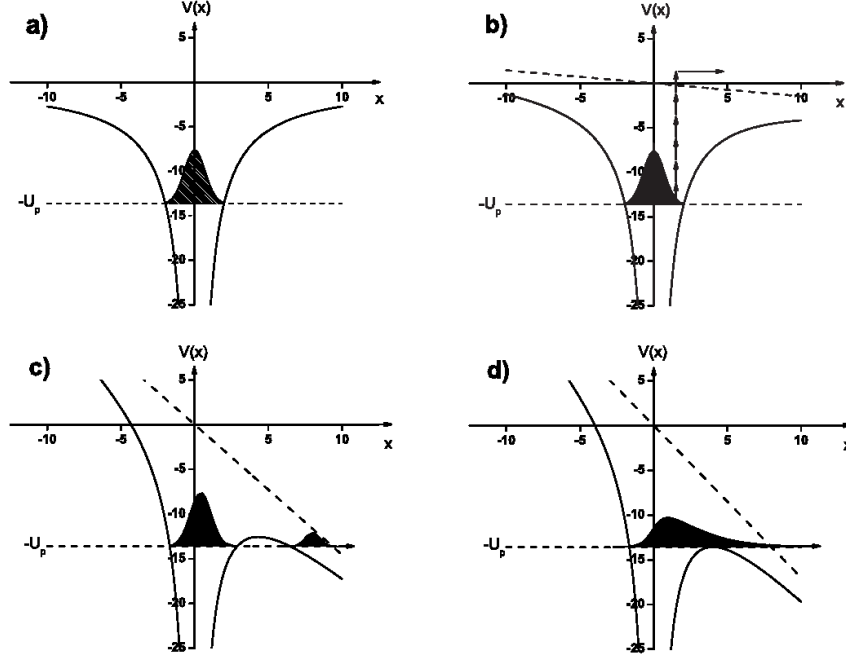


Figure 2.3.: a) Electrostatic potential $V(x)$ of an Ion with $Z = 1$ without external field. In b) - d) the external electric field is indicated by the dashed line. Different field strengths correspond to different dominant ionization processes: b) multiphoton ionization, c) tunnel ionization and d) barrier suppression ionization [20].

will cause a quiver motion with the cycle averaged velocity:

$$v_q = \frac{eE_0}{m\omega} .$$

Averaging the kinetic energy of this motion over one laser cycle gives the effective quiver energy, that is stored in the oscillation and is called the ponderomotive potential

$$\phi_p = \langle \frac{1}{2} m_e v_q^2 \rangle_{\text{cycle}} = \frac{e^2 E_0^2}{4m\omega^2} . \quad (2.1)$$

The negative gradient of this potential is the ponderomotive force, which is the resulting force also averaged over one laser cycle. This can also be derived from the equation of motion. Taylor expansion of the electric field gives:

$$E_y(r) \simeq E_0(y) \cos(\omega t - kx) + \frac{\partial E_0(y)}{\partial y} \cos(\omega t - kx) + \dots$$

to lowest order this results in the electron acceleration:

$$\frac{\partial v_y^{(2)}}{\partial t} = \frac{e^2}{m^2 \omega^2} E_0 \frac{\partial E_0(y)}{\partial y} \cos^2(\omega t - kx) ,$$

which gives for the ponderomotive force, after averaging over one cycle

$$F_p = m \frac{\overline{\partial v_y^{(2)}}}{\partial t} = -\frac{e^2}{4m\omega^2} \frac{\partial E_0^2}{\partial y} .$$

An important point is, that the force scales with the gradient of the electric field and therefore with the intensity gradient. Without an intensity gradient, as in a plane wave, acceleration and deceleration by the electromagnetic field cancel each other out. In case of a plane wave the electron will therefore quiver but return to its original place and velocity after one laser cycle. This also stands true for finite pulse duration. Since the laser beams that are used in the experiments are far from being a plane wave, but focused tightly, the strong intensity field gradient lead to a ponderomotive force perpendicular to the laser propagation direction. Quantitatively, this can be described like this: the electron quivers away from the center of the gaussian shaped pulse into a region with less intensity and will not be decelerated as effectively as it was accelerated. Therefore it gained energy and is accelerated to the region with less intensity. Electrons get pushed from regions of locally higher intensity to regions of lower intensities by the ponderomotive force.

In the relativistic case the electron dynamic becomes nonlinear and the magnetic term of the Lorentz force gains relevance, turning the direction of the electron momentum forward. The electron momenta, set in motion by a linearly polarized plane wave in the laboratory frame are given by:

$$p_x = \frac{a_0^2}{4}(1 + \cos 2(\omega t - kx)) , \quad p_y = a_0 \cos(\omega t - kx) , \quad p_z = 0 ,$$

with the normalized amplitude

$$a_0 = \frac{v_{\perp}}{c} = \frac{eE_0}{\omega mc}$$

being a dimensionless variable. Typically a_0 takes values between 0.5 and 2.5. Apart from the quiver motion the electron also starts to drift with an cycle-average velocity of

$$v_D = \frac{a_0^2}{4 + a_0^2} .$$

The motion of the single electron in the laboratory frame is shown in Fig. 2.4 a) for several different normalized amplitudes. A Lorentz transformation into a frame of reference that moves along with this velocity will lead to a solution of the equation of motion that is shown in Fig. 2.4 b). In this average rest frame the electrons move in a figure of eight

$$16x^2 = y^2(4q^2 - y^2) ,$$

2. Laser-induced particle acceleration

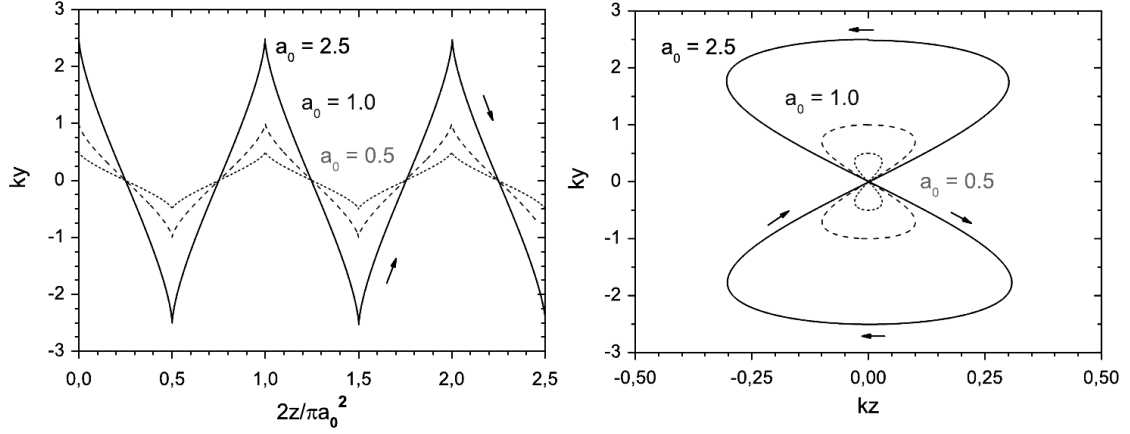


Figure 2.4.: Relativistic case for several normalized amplitudes a_0 a) in the lab frame, b) figure of eight in the average rest frame [20].

with

$$q = \frac{a_0}{2\sqrt{1 + \frac{a_0^2}{2}}} .$$

Still, in case of a plane wave and finite pulse duration the electron will travel in forward direction, but will not have gained kinetic energy after the laser pulse has passed. For acceleration an intensity gradient is necessary. In experiments this is provided, because the focusing of the pulse creates strong radial intensity gradients. The relativistic generalization of the ponderomotive force and ponderomotive potential are given by [22, 23] :

$$\vec{F}_p = -\frac{e^2}{4\bar{\gamma}m\omega^2} \nabla \vec{E}_0^2 , \quad \phi_p = \frac{e^2 E_0^2}{4\bar{\gamma}m\omega^2} ,$$

in which

$$\bar{\gamma} = \sqrt{1 + \frac{a_0^2}{2}} .$$

With 3D-simulations Quesnel and Mora have shown that independently from the polarization direction, electrons are accelerated radially out of the focus as well as in direction of the laser propagation.

The maximum kinetic energy is in the order of the ponderomotive potential. Equation 2.1 describes the ponderomotive potential, but it can also be given in practical units:

$$\phi_p = 9.33 \cdot 10^{-14} \cdot (\lambda[\mu\text{m}])^2 \cdot I[\text{Wcm}^{-2}] \text{ eV} .$$

A pulse of $0.8 \mu\text{m}$ wavelength with an intensity of $1 \cdot 10^{20} \text{ Wcm}^{-2}$ has a ponderomotive potential of 5.96 MeV . In the short time of the laser pulse duration almost none of

this energy is transferred to the kinetic electron motion. Higher particle energies are rather possible due to the collective response of the plasma to the incoming electromagnetic wave. There are many competing processes of energy transfer from the laser pulse into the plasma, increasing the electron temperature in the plasma and accelerating particles out of the target.

2.2.3. Interactions in a target, particle acceleration

When a high intense laser hits a target an plasma is created instantly. The dynamics in the plasma depend on plasma properties like the electron temperature T_e , the plasma frequency ω_p and the electron density n_e :

$$\omega_p = \sqrt{\frac{e^2 n_e}{\epsilon_0 \gamma m}} .$$

For radiation of frequencies that are higher than ω_p the plasma is transparent. The corresponding electron density to the plasma frequency is called critical density and can be given in practical units to calculate the critical density for a certain laser wavelength:

$$n_c \approx 1.1 \cdot 10^{21} \cdot \left(\frac{\lambda}{\mu\text{m}} \right) .$$

In case of solid targets field ionization rapidly creates a surface plasma layer with a density many times the critical density n_c . As an example we assume that in Aluminium the effective ion charge that is created by the leading edge of a high intense pulse of more than 10^{18} Wcm^{-2} is $Z^* = 9$ [15]. Under that assumption the electron density is $n_e = Z^* N_A \rho / A = 4 \cdot 10^{23} \text{ cm}^{-3}$, N_A being the Avogadro constant and A the atomic number, while the critical density of a Ti:sapphire laser working at 800 nm wavelength is $8.8 \cdot 10^{20} \text{ cm}^{-3}$

Similar to a mirror, the plasma reflects the incoming wave while the strength of the electric field decays exponentially inside the target, in the idealistic case of a step function for the density:

$$E(x) = E(0)e^{-x/l} ,$$

with l being the decay length, that can be approximated with

$$l \simeq \frac{c}{\omega_p}$$

for the highly overdense limit $n_0/n_c \gg 1$. At plasma densities this high the equation of motion has to be extended by a term that describes collisional damping:

$$\frac{d\vec{p}}{dt} = -e(\vec{E} + \frac{\vec{v}}{c} \times \vec{B}) - m\nu_{ei}\vec{v} ,$$

2. Laser-induced particle acceleration

where ν_{ei} is the electron-ion collision frequency and $\nu_{ei} \propto T_e^{-3/2}$. Hot plasmas are almost superconductors, with increasing temperature decreases the resistivity. The Debye-length is the distance after which the potential of a local charge in the plasma is reduced to the fraction of $1/e$:

$$\lambda_D = \sqrt{\frac{k_B T_e}{4\pi n_e e^2}}.$$

Electron accelerating mechanisms

The two main mechanisms for transferring laser energy to plasma electrons in the sub-ps-pulse regime are *Brunel type absorption* or *vacuum heating* and the relativistic $j \times B$ heating, of which the former was described first by Brunel in 1987 [24] and uses the *capacitor approximation* where magnetic fields are neglected. At a very steep density gradient, electrons that are close to the edge of the change from vacuum to plasma will be directly exposed to the laser field. The overdense plasma reflects the laser pulse similar to a mirror. Therefore, in case of oblique laser incident, a field component parallel to the target normal exists: $E_d = 2E_L \sin \theta$ if θ is the incident angle of the laser pulse. Electrons near the edge are dragged out by this component into the vacuum. When the field reverses, they are pushed back inside the plasma again. Inside the target the necessary condition for effective acceleration, a gradient of the electric field, is full filled. Since the electromagnetic field of the laser penetrates the plasma only up to the skin depth any electron that has gained enough kinetic energy to pass travel further inside the target, taking a part of the laser energy as kinetic energy with it. Beyond the skin depth it will be either be stopped by collisions and transfer the kinetic energy to the plasma or it will leave the target on the backside. In this way electron bunches are accelerated with each laser cycle parallel to the target normal. At laser intensities above 10^{18} Wcm^{-2} , when the quiver motion becomes relativistic $j \times B$ heating, originally pointed out by [25], gains relevance and other mechanisms are suppressed [15].

In principle this mechanism is similar to vacuum heating, here electrons are accelerated directly by the laser field near the edge of a step like density profile but the $v \times B$ component of the Lorentz force is now taken into account. Assuming again a linearly polarized wave $E = E_0(x)\hat{y}\sin\omega t$ the longitudinal force term is:

$$f_x = -\frac{m}{4} \frac{\partial v_y^2(x)}{\partial x} (1 - \cos 2\omega t),$$

which consists of the usual ponderomotive force, which pushes the electrons inside and through the target as in case of vacuum heating, and a high frequency component. This mechanism is most effective for normal incidence and works with any polarization of the laser light except circular.

Ion accelerating mechanisms

While the electrons can effectively be accelerated directly by the laser field, due to the much higher inertia of even the lightest ion, the ion quiver motion is negligible compared to that of the electrons. For direct acceleration of the ions to relativistic velocities intensities in the region of $I\lambda^2 > 10^{24} \text{ Wcm}^{-2}\mu\text{m}^2$ would be required², which is still not technically possible at the moment. Nevertheless, several groups have reported ion acceleration up to energies in the MeV range by irradiating thin foil targets with intensities between 10^{18} Wcm^{-2} and 10^{20} Wcm^{-2} . The record for the highest maximum proton energy of 67.5 MeV holds the Trident Laser Laboratory in Los Alamos [9]. The reason that ion acceleration in an irradiated plasma works is because the electrons mediate between laser and ions via charge separation. In the regime of relativistic quiver energies electrons are rapidly displaced from their initial positions, inducing fields in the order of magnitude of $\approx \text{GVm}^{-1}$. The principle of the process that goes by the name of *Target Normal Sheath Acceleration* (TNSA) or *plasma expansion* [27] and [28] is illustrated in Fig. 2.5. The electrons

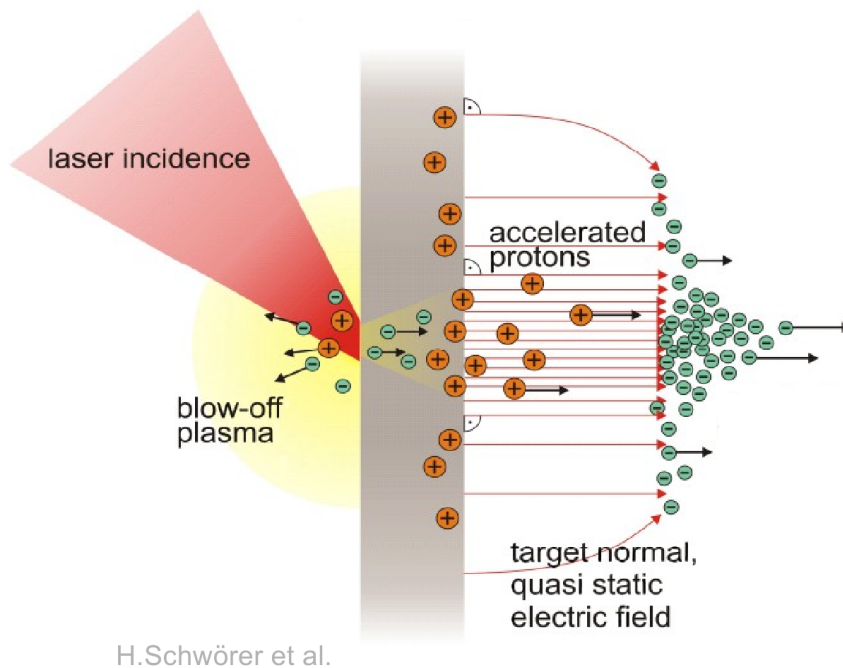


Figure 2.5.: Illustration of the process of Target Normal Sheath Acceleration [29].

are accelerated by the before mentioned mechanisms through the target and the hot electron population is fast enough to leave the plasma at the rear. This produces

²although recently a new regime for a different mechanism (light-sail) has been proposed [26], in which direct acceleration seems possible at lower laser intensities.

2. Laser-induced particle acceleration

a region of charge separation that extends typically a few μm behind the target surface of the backside. This quasi electrostatic field is directed perpendicular to the target and has a field strength of up to TVm^{-1} . These fields are strong and static enough to accelerate ions in MeV-range although the distance of acceleration is extremely short. This includes protons from impurities on the target surface, like hydrocarbons and water vapour. The result is usually an exponential spectrum of the proton energies.

3. Spin and polarization

The discovery of the spin of electrons bound in atoms by O. Stern and W. Gerlach in the year 1922, and later the discovery of nuclear spins [30] was the starting point of physics with polarized particles [10]. After the first years in which the concentrated attention was turned towards the measurement of spins and magnetic moments [31, 32], in the beginning of the 1950s the production of polarized particles became feasible [33]. A breakthrough for polarization physics was achieved with the nuclear shell model, which was able to explain the so-called "magic numbers" by introducing the LS -term, describing the coupling between the orbital angular momentum L and the spin angular momentum S [34]. Since nuclear states and reactions are closely related to spin, experiments with polarized particles are an important tool to understand the properties of nuclei.

In the experiment of Rabi in 1930, inhomogeneous magnetic quadrupole fields were first used for the selection of nuclear spin states [35]. Lamb and Retherford proposed a lambshift source to produce polarized beams in 1950, in which the long lifetime of the $2S_{1/2}$ state of the hydrogen atom is used for the separation of the hyperfine states [36]. In 1956, based on the Rabi apparatus, G. Clausnitzer, R. Fleischmann and H. Schopper proposed the atomic beam source [37], which was first implemented in the year 1960 in Basel [38]. Today the most common method is the last one mentioned and the principle of an atomic beam source will be described in 3.3 using the example of the polarized source at the **CO**oler **SY**nchrotron **COSY** at Forschungszentrum Jülich.

3.1. Spin formalism

Alongside with mass and charge the spin is a fundamental characteristic property of a particle, and an additional degree of freedom. All observed fermions have half-integer spin, bosons have integer spin. Quantum mechanically the spin is described by a spin operator $\mathbf{S} = (S_x, S_y, S_z)$. The corresponding eigenfunctions $|s, m\rangle$ are eigenfunctions to \mathbf{S}^2 with eigenvalue $s(s+1)$ as well as to S_z with the eigenvalue of m :

$$\mathbf{S}^2|s, m\rangle = s(s+1)|s, m\rangle, \quad S_z|s, m\rangle = m|s, m\rangle,$$

3. Spin and polarization

with possible values of $m = -s, -s+1, \dots, s$. With a given direction z the projection on this axis can take $2s + 1$ possible values $s_z = m\hbar$. One single particle is always completely polarized, and therefore, an example of a pure quantum state, while an ensemble of particles is a mixed state, a superposition of pure quantum states. If a measurement of the polarization corresponds to the operator \mathbf{P} , the expected value for \mathbf{P} is

$$\langle \mathbf{P} \rangle = \sum_{i=1}^n p_i \langle \psi^{(i)} | \mathbf{P} | \psi^{(i)} \rangle ,$$

where $\psi^{(i)}$ are the pure quantum states of single particles and p_i the probability to find the quantum state $\psi^{(i)}$ in the ensemble. The density operator ρ describes the statistical properties of the beam and is defined as:

$$\rho = \sum_{i=1}^n p_i |\psi^{(i)}\rangle \langle \psi^{(i)}| .$$

With this formula the expected value can be written as the trace of the product of the two operators:

$$\langle \mathbf{P} \rangle = \text{tr}(\rho \mathbf{P}) .$$

In case of protons the spin operators are

$$S_x = \frac{\hbar}{2} \cdot \sigma_x, S_y = \frac{\hbar}{2} \cdot \sigma_y, S_z = \frac{\hbar}{2} \cdot \sigma_z ,$$

with σ_x, σ_y and σ_z being the Pauli matrices:

$$\sigma_x = \begin{pmatrix} 0 & 1 \\ 1 & 0 \end{pmatrix}, \sigma_y = \begin{pmatrix} 0 & i \\ -i & 0 \end{pmatrix}, \sigma_z = \begin{pmatrix} 1 & 0 \\ 0 & -1 \end{pmatrix} . \quad (3.1)$$

The polarization $\mathbf{P} = (P_x, P_y, P_z)$ of a beam of spin 1/2 particles is then defined as the expected value of the Pauli matrices:

$$P_i = \langle \sigma_i \rangle, i = x, y, z . \quad (3.2)$$

If we choose \vec{e}_z as the reference axis with the probabilities p_+ and p_- for the projection of $\pm 1/2\hbar$ along the z -axis, the polarization is the expectation value of the corresponding Pauli matrix:

$$P_z = \langle \sigma_z \rangle = \sum_{i=1}^n p_i \langle \psi^{(i)} | \sigma_z | \psi^{(i)} \rangle = \sum_{i=1}^n \sum_m \sum_{m'} p_i \langle \psi^{(i)} | m \rangle \langle m | \sigma_z | m' \rangle \langle m' | \psi^{(i)} \rangle ,$$

with $\langle m | \sigma_z | m' \rangle = 2m\delta_{mm'}$ follows:

$$P_z = \sum_{i=1}^n \sum_m 2mp_i \langle \psi^{(i)} | m \rangle \langle m | \psi^{(i)} \rangle = \sum_m 2mp_m = p_+ - p_- .$$

For a particle beam consisting of N_+ particles with spin projection "up" and N_- particles with spin projection "down" the probabilities are

$$p_{\pm} = \frac{N_{\pm}}{N_+ + N_-} .$$

This gives for the polarization of a proton beam in terms of particle numbers:

$$P_z = p_+ - p_- = \frac{N_+ - N_-}{N_+ + N_-} .$$

Values of the polarization may thus vary in the region $-1 \leq P_z \leq 1$.

Reactions mediated by the strong interaction like elastic and inelastic scattering of particles off nuclei are sensitive to the spin of the involved particles. First consider the spin-less case of a particle scattering at some nucleon. Far away from the scattering point the particle wave can be described as

$$\psi_{\text{out}} = e^{i\vec{k}_{\text{in}}\vec{r}} + f(\vec{k}_{\text{out}}, \vec{k}_{\text{in}}) \cdot \frac{e^{ik_{\text{out}}r}}{r} , \quad (3.3)$$

with the form factor $f(\vec{k}_{\text{out}}, \vec{k}_{\text{in}})$ being a scalar. The first term describing the incoming plane wave, the second term describing the outgoing spherical wave. The cross section is then given as:

$$\frac{d\sigma}{d\Omega}(\text{in} \rightarrow \text{out}) = |f|^2 .$$

The wave function of a particle with spin is the product of the aforementioned wave function in space multiplied with the spin wave function:

$$\psi_{\text{in}} = e^{i\vec{k}_{\text{in}}\vec{r}} |\phi\rangle_{\text{in}} .$$

While in Eq. (3.3) the form factor is a scalar, for the description of the wave function including the spin an operator $M(\vec{k}_{\text{out}}, \vec{k}_{\text{in}})$, that works on the spin wave function, takes the place of $f(\vec{k}_{\text{out}}, \vec{k}_{\text{in}})$:

$$\psi_{\text{out}} = e^{i\vec{k}_{\text{in}}\vec{r}} + M(\vec{k}_{\text{out}}, \vec{k}_{\text{in}}) \cdot \frac{e^{ik_{\text{out}}r}}{r} ,$$

with

$$M(\vec{k}_{\text{out}}, \vec{k}_{\text{in}}) |\phi\rangle_{\text{in}} = |\phi\rangle_{\text{out}} .$$

Again, the particle beam has to be described in terms of spin quantum states $|\phi\rangle$ with the density operator

$$\rho_{\text{in}} = \sum_n |\phi\rangle_{\text{in}} \langle \phi|_{\text{in}} ,$$

and the density operator of the outgoing wave

$$\rho_{\text{fin}} = M \rho_{\text{in}} M^+ .$$

In the general case the cross section then is:

$$\frac{d\sigma}{d\Omega}(\text{in} \rightarrow \text{out}) = \frac{k_{\text{out}}}{k_{\text{in}}} \text{tr}(\rho_{\text{out}}) = \frac{k_{\text{out}}}{k_{\text{in}}} \text{tr}(M \rho_{\text{in}} M^+) .$$

3.2. Manipulation of particle spins

Connected to the spin is the magnetic moment of a particle, which can interact with a magnetic field and, therefore, allows a manipulation of the particle trajectory depending and spin-flip. For a particle with charge q , mass m and spin \vec{s} the magnetic dipole moment is given by

$$\vec{\mu}_s = g \frac{q}{2m} \cdot \vec{s}, \quad (3.4)$$

where the dimensionless number g is 2.0023 for electrons and 5.586 for protons. Since the projection of the spin on the direction of the magnetic field is the quantization axis, this is also the case for the magnetic moment. The magneton

$$\mu_s = \frac{q}{2m} \cdot \hbar \quad (3.5)$$

is the Bohr magneton $\mu_B = e\hbar/2m_e = 9.27400915 \cdot 10^{-24}$ J/T or the nuclear magneton $\mu_N = e\hbar/2m_p = 5.05078324 \cdot 10^{-27}$ J/T for electrons or protons, respectively. Therefore, the potential energy U of a particle due to its magnetic dipole moment μ in a magnetic field is quantized:

$$U = -\vec{\mu} \cdot \vec{B} = \pm \frac{1}{2} g \mu_{B/N} \cdot B .$$

If the thermal energy of the particle is below this difference it is possible to orient the spins of the particles towards a magnetic field. For an ensemble of particles the ratio between the number of particles with spin up N_+ and N_- is given by

$$\frac{N_+}{N_-} = \exp\left(\frac{\Delta U}{k_B T}\right),$$

where k_B is the Boltzmann constant and T the absolute temperature. In this way a manipulation of proton spins directly by a magnetic field is possible, although technically demanding. This principle is used in frozen spin targets. For example in the frozen spin target operated at Bonn University the necessary conditions are provided with a temperature of 70 mK and a magnetic field of 1.1 T and a polarization of more than 98 % can be achieved [39].

In a typical laser field with field strengths of $B = 10^4$ T the difference of the potentials ΔU is in the order of magnitude of 10^{-4} eV but the temperature in plasmas are typically of several thousand Kelvin.

3.3. Stern-Gerlach effect and atomic beam source

The Stern-Gerlach effect was first observed by Stern and Gerlach in 1922. Based on this Rabi could observe with his apparatus the hyperfine-splitting due to the

nuclear spin in 1930 [35]. A modified version can be used to produce polarized particle beams in atomic beam sources. Figure 3.1 shows a schematic view of the Stern-Gerlach apparatus. The principle of the experiment was to send a beam of silver atoms through an inhomogeneous magnetic field and observe the resulting deflection caused by the interaction between the magnetic moment of the atom and the gradient of the magnetic field. In case of silver atoms, the spin of the whole

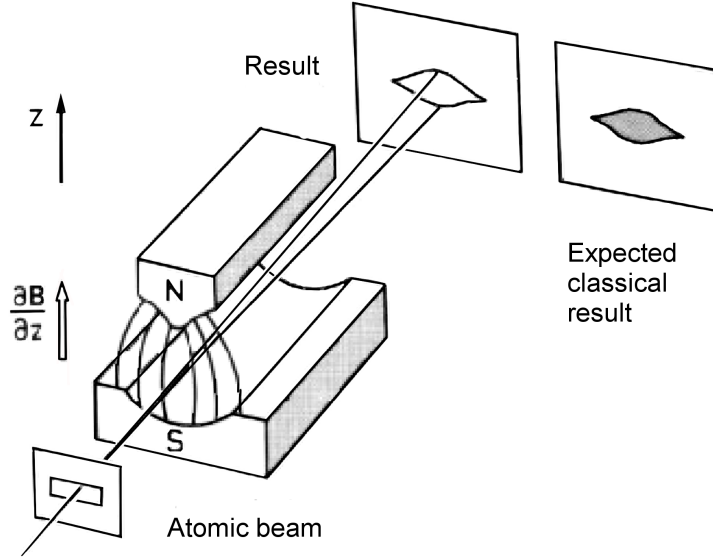


Figure 3.1.: Principle of the Stern-Gerlach experiment [10].

atom is given by the spin of the single valence electron. The classical expectation would be a smooth distribution, but since the magnetic moment and the resulting force takes only certain quantized values:

$$\vec{F} = -\nabla U = -\frac{\partial U}{\partial B} \frac{\partial B}{\partial z} \vec{e}_z = \pm \frac{1}{2} g \mu_{\text{eff}} \frac{\partial B}{\partial z} \vec{e}_z \text{ for } m_s = \mp \frac{1}{2}, \quad (3.6)$$

while, in case of the silver atom, μ_{eff} is the magnetic momentum of the electron spin. Therefore, the beam is divided, which was observed on the detection screen as illustrated in Fig. 3.1. With this experiment the spin of the electron bound in the silver atom was discovered.

In the apparatus of Rabi, high frequency was first used induce transitions between spin states and transfer electron spin polarization to nuclear spin polarization. This method was developed further to the atomic beam source for the production of polarized hydrogen beams. Starting point is a controlled flow of hydrogen molecules, which are dissociated into single hydrogen atoms. In the 1 s ground state the hydrogen atoms have an orbital angular momentum quantum number $L = 0$, an electron spin $S = 1/2$, $m_s = \pm 1/2$ and proton spin of $I = 1/2$, $m_I = \pm 1/2$. The

3. Spin and polarization

hydrogen atoms are then guided by a beam formation unit into the first set of spin separation magnets. In a magnetic field with an axial symmetric potential and a radial field gradient the force, that operates on the hydrogen atoms, is quantized like described in Eq. (3.6) except for the quantization axis, which in this case is \vec{e}_r . Therefore, protons with spin orientation $m_s = +1/2$ are focused on the beam line, while protons with spin orientation $m_s = -1/2$ are driven away from the axis. At the polarized ion source of COSY sextupole magnets are used, which are the usual choice for separation magnets because the force on the protons increases proportionally with the radius. In the strong field of the sextupole magnets electron and nuclear spins are decoupled and the energy levels of the hydrogen atom are no longer degenerate. The states with the electron spin direction $m_s = -1/2$ are sorted out in the magnets by defocusing. Afterwards the beam has nearly 100% polarization regarding the electron spin. While drifting adiabatically to weaker field strengths, electron and nuclear spin couple again to the total spin \vec{F} . The states $|F, m_F\rangle = |1, 1\rangle$ and $|1, 0\rangle$ are found in the hydrogen atom only, which correlate to electron and nuclear spin like

$$|1, 1\rangle = |m_I = 1/2, m_s = 1/2\rangle$$

and

$$|1, 0\rangle = \frac{1}{\sqrt{2}} \left(\sqrt{1+a} |m_I = 1/2, m_s = -1/2\rangle + \sqrt{1-a} |m_I = -1/2, m_s = 1/2\rangle \right) ,$$

with

$$a = \frac{\frac{B}{B_c}}{\sqrt{1 + \left(\frac{B}{B_c}\right)^2}}$$

and $B_c = 50.7$ mT in case of hydrogen. A magnetic field is considered weak if $B \ll B_c$. The number of Atoms is distributed equally between the two states, the probability p_+ to find $m_I = +1/2$ is

$$p_+ = \frac{1}{2} p_+(|1, 1\rangle) + p_+(|1, 0\rangle) = \frac{1}{2} + \frac{1+a}{4} ,$$

which gives for the nuclear polarization of the beam

$$p = p_+ - p_- = \left(\frac{1}{2} - \frac{a}{4} \right) .$$

Since in a weak field $a \ll 1$, a part of the electron polarization was transferred to the protons. To enhance the polarization, changes in the population of hyperfine state are induced by radio frequency. Transitions are induced between the states $|m_I = -1/2, m_s = -1/2\rangle$ and $|m_I = +1/2, m_s = +1/2\rangle$. After another set

of sextupole magnets the state $|m_I = -1/2, m_s = -1/2\rangle$ is sorted out and only $|m_I = -1/2, m_s = +1/2\rangle$ remains. Another high frequency transition from this state to $|m_I = +1/2, m_s = -1/2\rangle$ leaves the atomic beam with 100% nuclear spin polarization. Afterwards the atoms are ionized and accelerated.

3.4. Observation

The polarization of a particle beam is measured by detecting a left-right asymmetry in a reaction (scattering process) that is sensitive to the particle polarization. A new observable has to be defined at that point, the analyzing power A_i , which describes the dependence of the differential cross section of a reaction on the spin orientation due to the coupling of spin and angular momentum. In case of a beam of spin $1/2$ particles the cross section can be written as

$$\frac{d\sigma}{d\Omega_{\text{pol}}} = \frac{d\sigma}{d\Omega_0} (1 + P_x A_x + P_y A_y + P_z A_z) .$$

Since observables like the polarization and analyzing power depend on the coordinate system, it is useful to agree on a coordinate system. Here, the Madison convention will be used.

For the coordinate system of the incoming particle (x, y, z) the z -axis is defined along the momentum of the particle \vec{k}_{in} . If the experiment is not a double scattering experiment, where the coordinates are given by the first scattering process, the two other coordinate directions are free to choose for the moment. For the outgoing particle (x', y', z') we keep the z -axis, ($\vec{e}_z = \vec{e}_{z'}$), the y' -axis is defined along the direction of the normal vector

$$\vec{n} = \frac{\vec{k}_{in} \times \vec{k}_{out}}{|\vec{k}_{in} \times \vec{k}_{out}|} ,$$

with \vec{k}_{out} being the momentum of the outgoing particle, the x' -axis completes the left-handed system.

The two systems are transformed from one to another by a rotation around the z -axis by the angle ϕ as depicted in Fig. 3.2. During the scattering reaction the only component of the analyzing power different from zero is the one parallel to \vec{n} , $A_{y'}$, since this is the only one invariant to parity transformations. The component $P_{y'}$ of the polarization along this axis is given by the transformation between the coordinate systems:

$$P_{y'} = \vec{P} \cdot \vec{e}_{y'} = -\sin \phi P_x + \cos \phi P_y .$$

3. Spin and polarization

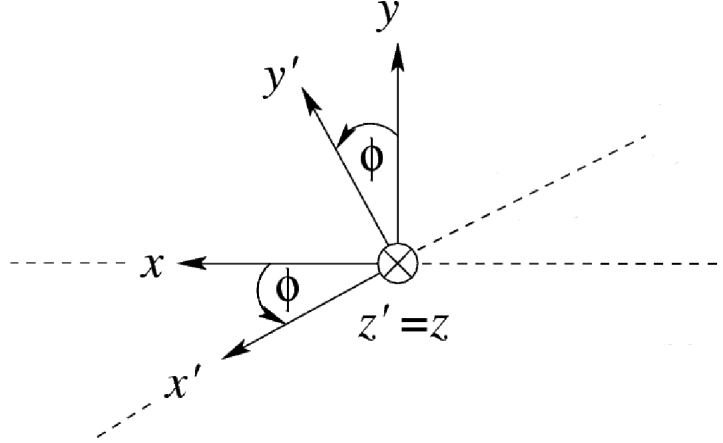


Figure 3.2.: Transformation between initial and final coordinate systems via rotation angle ϕ [40].

If we choose the y -axis for the system of the incoming particle parallel to the beam polarization, this leaves for the differential cross section

$$\frac{d\sigma}{d\Omega_{\text{pol}}} = \frac{d\sigma}{d\Omega_0} (1 + A_{y'} P_y \cos \phi) .$$

The indices of polarization and analyzing power will be omitted in the following equations. With known analyzing powers for a target material the polarization of a particle beam can be studied by measuring the angular distribution of the scattered particles. The maximum and minimum of the cross section, and, therefore, the number of particles that are detected, can be found in the plane perpendicular to the beam polarization. The numbers of particles N_ϕ detected in the solid angle $\Delta\Omega$ can be calculated as

$$N_{\phi=0} = nN_A\Delta\Omega D \left(\frac{d\sigma}{d\Omega_0} \right) \cdot (1 + PA) \quad (3.7)$$

$$N_{\phi=180} = nN_A\Delta\Omega D \left(\frac{d\sigma}{d\Omega_0} \right) \cdot (1 - PA) , \quad (3.8)$$

where ϕ is the azimuth angle of the coordinate system (x, y, z) and n is the number of incoming particles, N_A the target density, $d\sigma/d\Omega_0$ the unpolarized cross section and D is a factor that describes the detection probability of the detector. By measuring the asymmetry

$$\epsilon = \frac{N_0 - N_{180}}{N_0 + N_{180}} = PA$$

the degree of polarization can be derived with known analyzing power.

A polarimeter basically consists of a scattering target and detectors to measure

the angular distribution behind the target. If the direction of the polarization is known two detectors located at the maximum and minimum of the distribution are sufficient to measure the degree of polarization. Obviously, it is useful to choose a target with a high absolute value of the analyzing power in the energy region of the incoming particle beam. To maximize the accuracy of the experiment it is important to minimize the statistical uncertainty, which depends on the analyzing power and the intensity of the particle beam.

With a beam polarization of

$$P_{\text{beam}} = \frac{1}{A} \frac{N_0 - N_{180}}{N_0 + N_{180}}$$

the statistical error of the polarization according to the law of error propagation of Gauss is given by

$$(\Delta P_{\text{beam}})^2 = \left(\frac{\partial P}{\partial N_0} \cdot \Delta N_0 \right)^2 + \left(\frac{\partial P}{\partial N_{180}} \cdot \Delta N_{180} \right)^2 .$$

Assuming, that the statistical error of each measurement of N_ϕ is $\Delta N_\phi = \sqrt{N_\phi}$ partial differentiation and inserting N_ϕ from the Eqs. (3.7) and (3.8) leads to

$$\Delta P_{\text{beam}} = \frac{1}{\sqrt{n N_A \Delta \Omega D}} \sqrt{\frac{(1 - \epsilon^2)}{\frac{d\sigma}{d\Omega} A_y^2}} . \quad (3.9)$$

Apart from the statistical uncertainty, fluctuations of the background level may also limit the accuracy of the measurement. Given background signals of $B_{\phi=0}$ and $B_{\phi=180}$ with an asymmetry of $\epsilon_B = (B_0 - B_{180}) / (B_0 + B_{180})$ the statistical error of the polarization is given by [41]:

$$\begin{aligned} \Delta P &= \frac{1}{A \sqrt{N_0 + N_{180}}} \sqrt{(1 - \epsilon)^2 + \frac{2(B_0 + B_{180})}{N_0 + N_{180}} (1 + \epsilon^2 - 2\epsilon\epsilon_B)} \\ &= \Delta P_{\text{beam}} + \frac{1}{n N_A \Delta \Omega D} \sqrt{\frac{2(B_0 + B_{180})}{\left(\frac{d\sigma}{d\Omega}\right)^2 A^2} (1 + \epsilon^2 - 2\epsilon\epsilon_B)} . \end{aligned}$$

Defining the *figure of merit* F of a polarization measurement as being proportional to ΔP^{-1} two cases have to be distinguished:

1. The background is negligible in comparison to $N_0 + N_{180}$ and the error of the measurement is basically ΔP_{beam} , in this case the figure of merit is

$$F \propto A \sqrt{\frac{d\sigma}{d\Omega}} . \quad (3.10)$$

2. In case of high background:

$$F \propto A \frac{d\sigma}{d\Omega} . \quad (3.11)$$

3.5. Particles with spin in laser-plasma interactions

During the acceleration of particles in laser-generated plasmas high magnetic fields are formed behind the foil target by the current of escaping hot electrons and the return current at the target surface. These fields usually have values in the order of 10^4 T in the center of the focus and decrease over 10 or 20 μm radially away from the beam axis of the laser pulse, producing very high field gradients.

Analogical to the case of the radial gradients in the magnetic system of an atomic beam source one might expect protons to encounter forces, that are quantized according to their spin orientation either in direction to the beam axis or radially away. There are several concerns however about the quantitative effect on the proton trajectories. Since the target material is ionized instantly by the leading foot of the laser pulse, the force described in Eq. (3.6), that occurs due to the magnetic field gradients, has to accelerate the protons directly. A fundamental concern is the "thesis of Bohr" (described by Pauli [12]), who stated that according to the uncertainty principle, spin states of electrons, or any other charged particle, cannot be separated by a magnetic force on the electron dipole moment. Bohrs argument stands true for protons as well, since it is based on the uncertainty in the Lorentz force, that acts on the particle. Because of Maxwell's equation $\nabla \cdot \vec{B} = 0$ and under the assumption, that in flight direction x the magnetic fields are constant (as usually the case for a Stern-Gerlach apparatus, although not necessarily in a plasma) the uncertainty of the force in z -direction is

$$\Delta F_z = q \frac{p_x}{M} \frac{\partial B_y}{\partial y} \Delta y .$$

With the requirement of $\Delta F_z \ll F_z$ the necessary condition for the separation of the spins is:

$$\frac{\Delta F_z}{F_z} = 4\pi \frac{q}{e} \frac{m}{M} \frac{\Delta y}{\lambda_x} \ll 1 . \quad (3.12)$$

With q being the charge of the particle and λ_x the de Broglie wavelength. M is the mass of the particle, while m is the proton or electron mass, if the force F_z acts on the dipole moment of the nuclear spin or the electron spin, respectively. In the case of electrons or protons, where $q \neq 0$ and $m/M = 1$ it is necessary to achieve $\Delta y < \lambda_x$. Garraway and Stenholm showed, that it is possible to achieve this condition and obtain spin-separation in the momentum space, which will eventually lead to a spatial separation after a sufficiently long propagation time in an interaction free region [42], as well as the possibility to use classical trajectories for the calculation of the problem [11]. These studies are related to the situation in a Stern-Gerlach apparatus, where the magnetic fields are static, constant in propagation direction of the particle and small enough to neglect higher order corrections. All this does not apply during laser-plasma interaction, so dedicated calculations and simulation studies are necessary.

Figure 3.3 shows the quasi-static magnetic field in a laser target obtained by a simulation program. The fields stretch not more than $10 \mu\text{m}$ in space and the time the

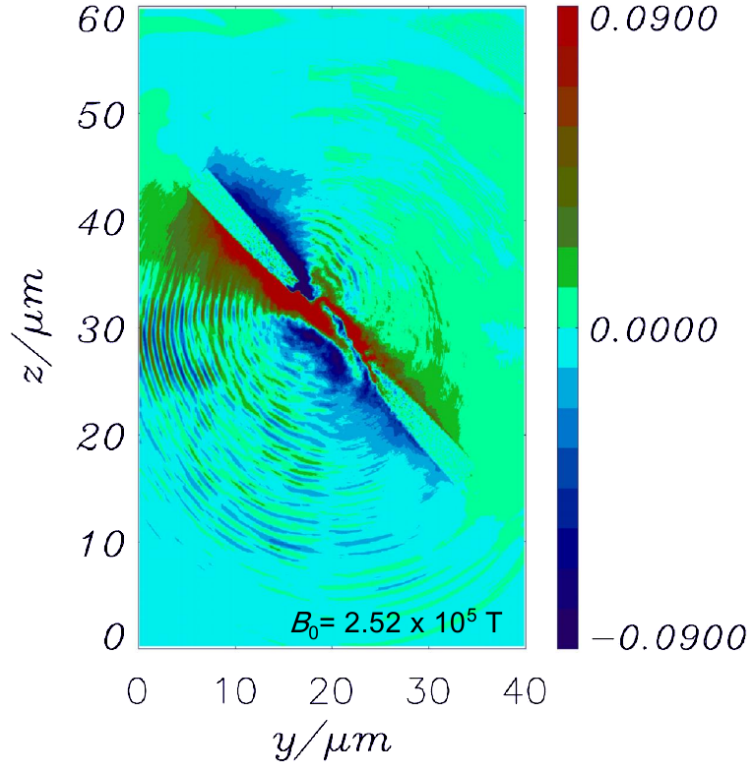


Figure 3.3.: Quasi-static magnetic fields in and around a plasma target from a two-dimensional simulation [43]. The target is tilted 45° with respect to the laser beam direction.

protons are under the influence of the dividing force is less than 100 fs.

A more detailed description of the program and more detailed calculations of the expected effects of the magnetic fields on the particle trajectories in case of plain foil targets will be given in Sect. 6. Even with this naive approach, that neglects the uncertainty of the Lorentz force no measurable separation of spin up and spin down protons is expected. One has to take into account, that the nuclear magneton μ_N is much smaller than the Bohr magneton μ_B , so that the high field gradients have to compensate for a factor of approx. 10^3 . While the magnets in an atomic beam source can be extended in order to prolong the time the protons stay under the dividing force of the gradients, the extent of the magnetic fields behind the target is very limited.

Although no polarization is expected based on the naive arguments above, we have carried out our first measurements with foil targets to establish the method by a null-experiment. This will be described in Sect. 7.

3. Spin and polarization

On the other hand, if no effect on the particle due to the magnetic fields of the plasma is possible, this clears the way for the second scenario, which is to use polarized targets, like frozen spin targets for protons. If the polarization of the particles is preserved during the laser-induced acceleration of the particles the produced particle beams would carry a polarization in the order of magnitude of the polarization of the target.

4. Experimental methods

In the frame of this thesis simulation and experimental studies were carried out. To simulate the processes in the plasma target and to provide a first estimate about the possible polarization of the proton beam, Particle-in-Cell codes were used, the principles of which are presented in the first section of this chapter.

For the measurement of the polarization a scattering target was used, where the spin-dependent analyzing reaction takes place. The target material has been chosen carefully, considering analyzing powers, available data and practical criteria, which is described in Sect. 4.2.

With the help of the Geant4 package from CERN Monte-Carlo studies were used to optimize the design of the experimental setup as well as for the verification and better comprehension of the experimental results. A general description of Geant4 follows in Sect. 4.3, while details of the specific simulations for the measurements will be given in Sect. 7.

In the last section of this chapter the detectors that were used during the measurements are described.

4.1. Particle-in-Cell Simulations and the program BOPS

The simulation program BOPS has been originally written by Paul Gibbon and Tony Bell in the Plasma Physics Group of Imperial College, London. It is a one and three halves (1 spatial, 3 velocity coordinates) Particle-in-Cell (PIC) code [44]. As a third particle species protons have been added to electrons and ions of the target material in order to provide an additional proton-rich layer, that mimics the impurities and dirt on the surfaces of foil targets.

Particle-in-Cell codes

In PIC codes the particle velocity distribution is represented by a number of discrete macro-particles with fixed charges and masses. Figure 4.1 schematically displays one time step Δt of the program. The particles are mapped on a grid, defining charge density $\rho(r)$ and charged current $J(r)$ on each grid point. Electric and magnetic

4. Experimental methods

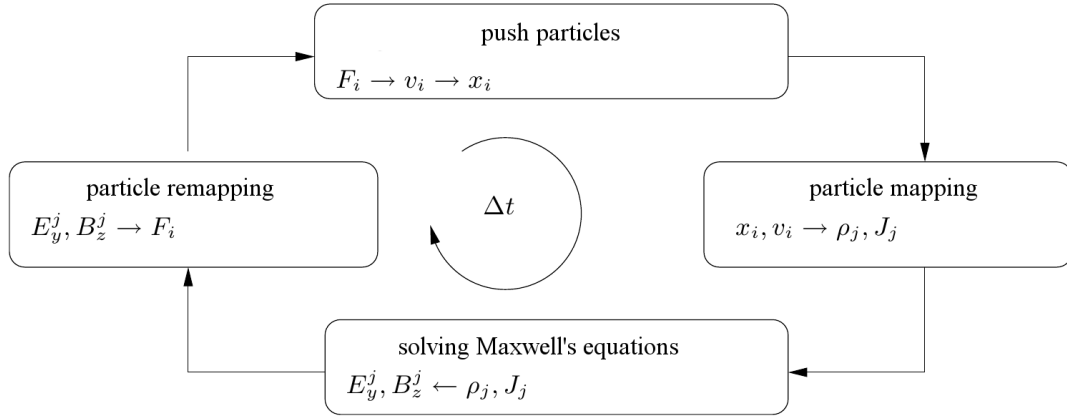


Figure 4.1.: Schematic illustration of the PIC algorithm [45].

fields are then calculated by solving Maxwell's equations. After remapping the grid points to the particle positions they are moved according to the Lorentz equation, before the cycle starts again with the mapping of the particles.

Relativistic boost technique

To save computing time during each time step the code is reduced from a two-dimensional spatial geometry to a one-dimensional making use of the relativistic boost technique. By performing a Lorentz transformation along the target surface moving at $v_0 = c \cdot \sin \phi$, with ϕ being the incident angle of the laser pulse, the problem is transferred to a simulation frame where laser incidence is perpendicular to the target surface. The technique was invented in 1990, and later applied to absorption of fs laser pulses on solid targets in Ref. [46]. A detailed description of the method can be found in Ref. [44]. The huge reduction in computing time makes it possible to study many different target configurations or perform high-resolution simulations at reasonable computational effort.

4.2. Analyzer target

There are several potential materials than can be used to analyze the polarization of a proton beam in the few MeV region. Data sets of cross section and analyzing power were available for helium, carbon and silicon [47, 48, 49]. Helium was excluded, since it has severe practical disadvantages compared to the solid state materials. The construction of a cell for the gaseous material inside the vacuum of the experimental chambers would have been necessary. Due to the low density, the path of the protons through the material would have to be prolonged to increase

the probability of a hadronic interaction, while in case of a solid target a thin slice is sufficient. This made it possible to construct a very compact measurement setup, which fitted well inside of the experimental chambers. In case of a solid state target no windows are required for the entrance and departure of the particle beam, so that the protons will not lose kinetic energy before arriving at the target.

For the choice of the target the figure of merit F was used, that is given by Eq. (3.11) and is explained in Sect. 3.4. The figure of merit $F \propto A \cdot d\sigma/d\Omega$ in case of high background was chosen due to the low signal to background ratio that was expected.

Another aspect that has to be taken into account is the energy spectrum of the laser-generated proton beam. In chapter 5.3 the measurement of the spectrum, that is produced at the laser facility in Düsseldorf is described. The exponential shape of the spectrum has to be taken into account, since the usable particle rate varies drastically with the kinetic energy. Carbon and silicon were studied more closely as possible analyzing materials.

In case of carbon, data for cross sections and analyzing powers are available starting at a beam energy of 4.5 MeV. Figure 4.2 shows the available data of both for scattering angles ϑ of 40° and 50° . According to the data the measurement at

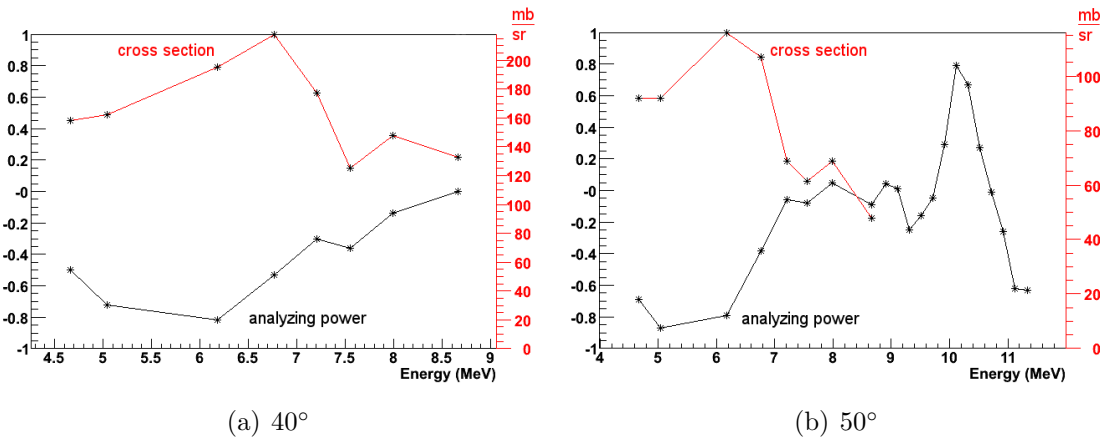


Figure 4.2.: Analyzing powers (black) and cross sections (red) for the C(p, p')C reaction [48].

energies between 5 and 6 MeV is preferable. At a scattering angle of about 50° the analyzing power is $A = -0.8$ and the differential cross section $d\sigma/d\Omega \approx 100$ mb/sr. Assuming the high background of the CR-39 detectors, the figure of merit is $F \propto d\sigma/d\Omega \cdot A \approx 80$ mb/sr. At a smaller scattering angle of 40° the cross section doubles approximately which gives ≈ 160 mb/sr

In case of silicon as target material Fig. 4.3 shows the complete data set of analyzing powers and cross sections, while for clarity purposes in Fig. 4.4 the analyzing

4. Experimental methods

power for 45° and 60° is shown separately. For energies between 2.5 and 3.5 MeV the analyzing power in silicon passes through a minimum at approx. 2.9 MeV. At 60° the analyzing power in the minimum and the cross section for this energy are $A = -0.6$ and $d\sigma/d\Omega \approx 600$ mb/sr. Disadvantage of the silicon is the strong energy dependence of cross section and analyzing power. Since in our experiments the particle energy cannot be selected as precisely as 0.1 MeV the averaged analyzing power over an energy range that spans the minimum of the function is higher than -0.6 . Assuming an effective analyzing power of ≈ -0.4 the figure of merit is still $F \propto d\sigma/d\Omega \cdot A \approx 240$ mb/sr.

In case of a scattering angle of 45° the analyzing power in the energy range of 2.8 to 3.3 MeV is approx. -0.2 and the cross section ≈ 1400 mb/sr, which gives for the product ≈ 280 mb/sr.

Finally a strong argument for the choice of silicon as analyzing material becomes obvious if one takes into account the energy spectrum that is produced in the laser-induced plasma. In this energy region silicon is an adequate analyzing material for the polarization of protons [50], because the number of protons at around 3 MeV is by an order of magnitude larger than at 5 MeV. On the whole, the use of a silicon target promised better statistics and therefore a more accurate measurement.

A silicon target with a thickness of $24 \mu\text{m}$, originally intended for the use in a semiconductor detector, was purchased at *micronsemiconductor*. The purity of the silicon material was given as less than 10^{13} foreign atoms per cm^2 , compared to $5 \cdot 10^{18}$ silicon atoms per cm^2 , so that scattering events that might occur at foreign atoms could be neglected.

4.3. The simulation toolkit Geant4

The original software toolkit Geant4 and the object-oriented library ROOT were developed by CERN [51]. Basis of both ROOT and Geant4 is the object oriented programming language C++. ROOT provides packages for applications of data analysis like histogramming, curve fitting, interpolation and man more, while Geant4 provides facilities for the handling of a setup geometry, particle tracking, detector response, run management, visualization and user interface.

After the geometry of the measurement setup is defined, particles can be sent through the setup from a particle source. The trajectories of the particles are calculated, considering the geometry, electromagnetic fields and the processes that occur in the materials. From known cross sections or theoretical calculations the probability of the occurrence of a process is calculated. Physics processes have to be assigned to the particles to occur, which gives the opportunity to "switch of" processes and

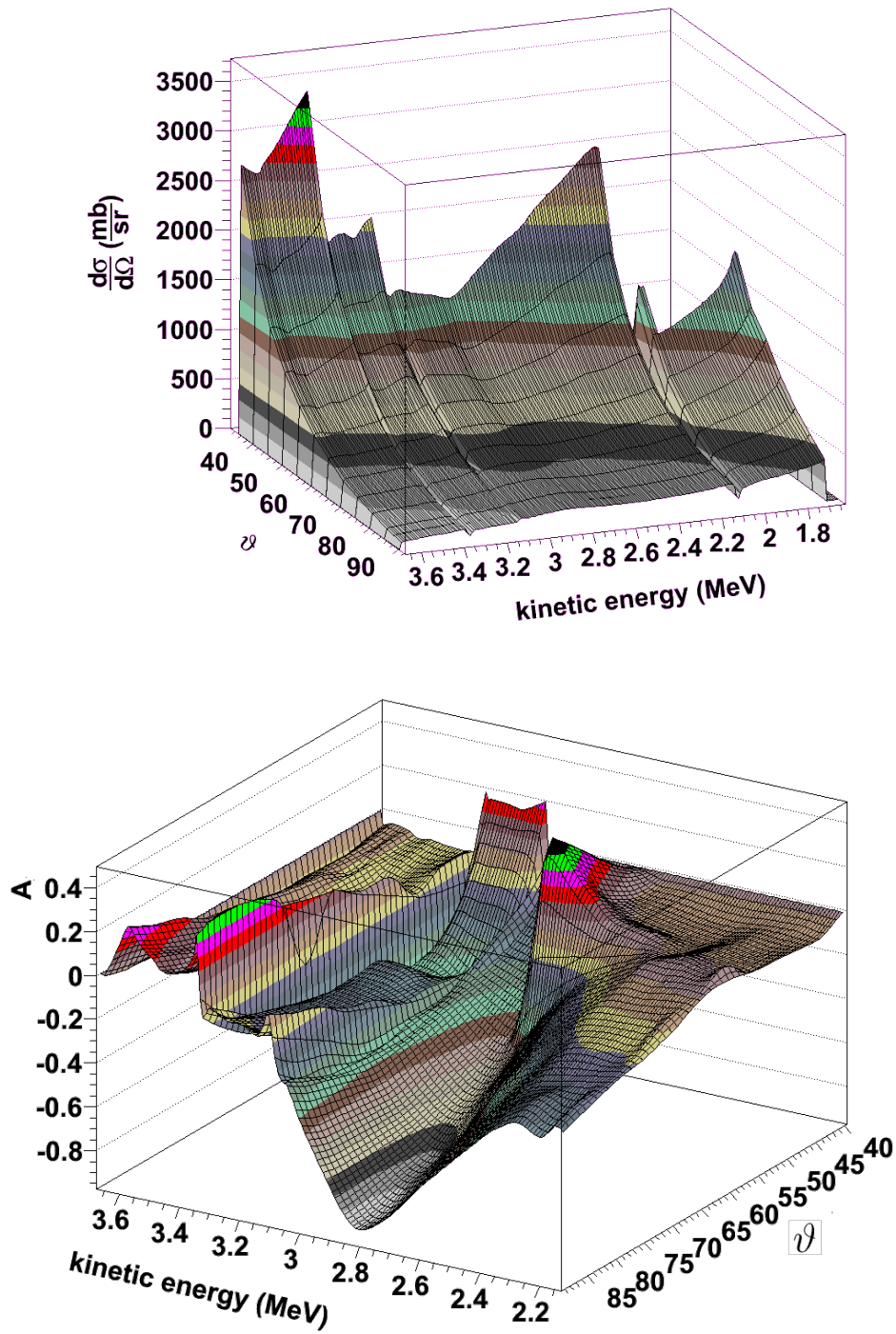


Figure 4.3.: Differential cross section and analyzing power for the $\text{Si}(p, p')\text{Si}$ reaction [49].

4. Experimental methods

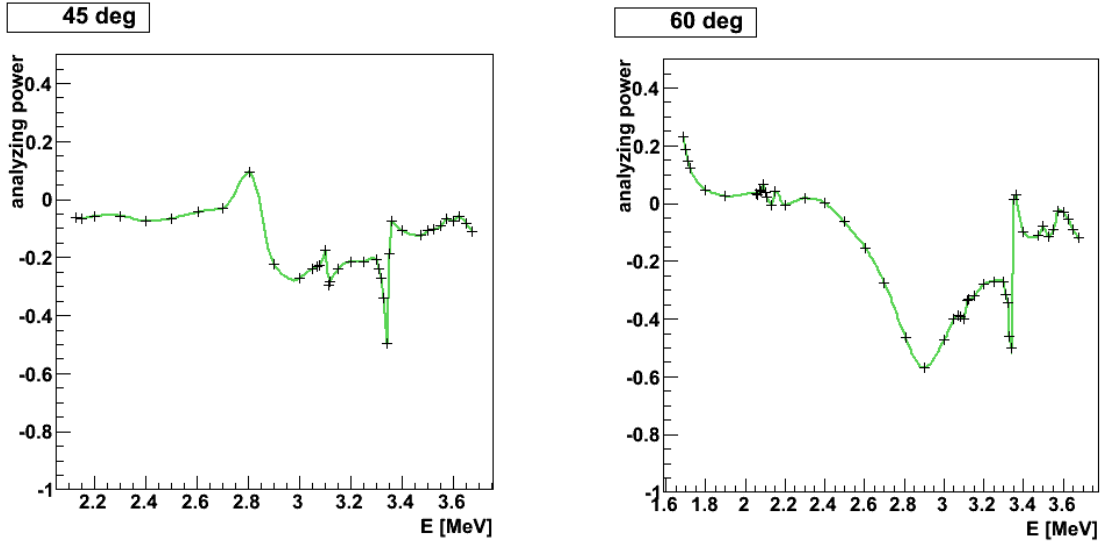


Figure 4.4.: Analyzing power for proton scattering on silicon for 45° and 60° [49].

study other processes separately.

For the simulation of the measurement setup Geant4 was used for particle tracking and detector response, ROOT was used to handle input and output data for and from the simulation program.

The simulation is divided in two separate programs: simulation of laser accelerated protons (*slap*) for simulation of the background and silicon polarimeter *sipol* for the simulation of the hadronic interaction. The program *slap* contains the complete setup, with the plasma target as point-like particle source. To study multiple scattering and energy loss by ionization separately from the hadronic scattering, the hadronic processes were switched off.

The hadronic interaction in the silicon target is simulated in the program *sipol*. In principle in this simulation the silicon target is the particle source emitting only protons that have just encountered in a nuclear reaction and are scattered under angles between 30° and 70° . Geant4 is used as a frame, analyzing powers of hadronic interactions are not provided by the toolkit. So these numbers have been put in manually from the available data set. The necessary preparation of the data for the use in the program will be described here, further details of both programs and the simulation studies will follow in Sect. 7 after the measurement setup has been explained.

Preparation of the analyzer data

The data sets provided by the University of Cologne contains cross sections and analyzing powers for energies between 2.2 and 3.5 MeV protons for scattering angles

of more than 40° . For proton energies between 3.5 and 3.67 MeV values for 35° are also available. Since there are several resonances in this energy region, more values have been taken closer to the resonances than in the parts lying between them. In order to provide cross section data for the program *sipol*, the data was pre-processed via ROOT, to obtain data in constant steps of 0.01 MeV and 1° . Starting with a two-dimensional histogram of the available data the first step was to interpolate between the values for different energies to obtain a histogram with a bin width of 0.1 MeV in this direction. For the interpolation the akima algorithm of the *mathmore* package of ROOT was used. In the second step for each energy bin of the histogram a one-dimensional histogram is produced that contains the cross section depending on the scattering angle. Between the data points again the akima interpolation is used to produce steps of 1° . Also the data was extrapolated to scattering angles of 35° for energies of less than 3.3 MeV. Figure 4.3 shows the data and the results of different extrapolation algorithms for the example of 3.1 MeV. For the extrapolation it was decided to use the polynomial algorithm. Since this extrapolation is afflicted with higher uncertainties, the data for more than 3.3 MeV was used whenever possible. A ROOT file has been produced, that is used as input

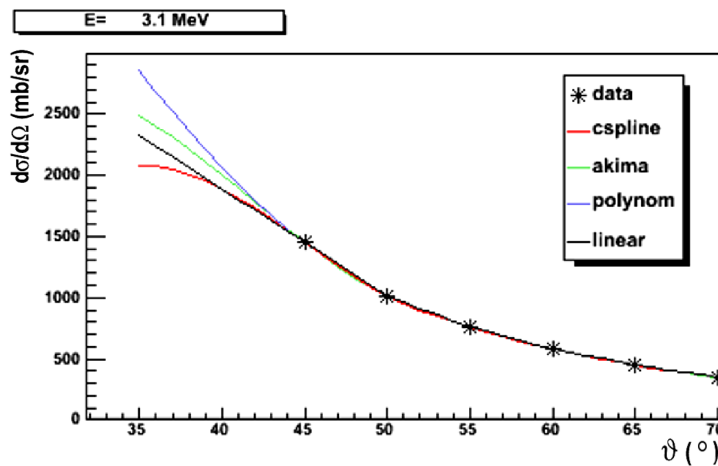


Figure 4.5.: Extrapolation with different algorithms for the example of 3.1 MeV.

for the program *sipol* containing 154 histograms for energies between 2.13 MeV and 3.67 MeV, each containing the cross section depending on the scattering angle. In a similar way, a two-dimensional histogram was produced, that contains the analyzing powers in dependence of energy and scattering angle.

4.4. Detectors

Laser induced plasmas are particle sources that provide extremely short bunches at very high numbers of particles. It is not unusual for 10^{10} particles to hit a detector within nanoseconds. Additionally there is strong x-ray and γ radiation from the plasma. Detectors that are used for these sources have therefore to be able not only to detect a high particle flux at practically zero dead time and without radiation damage. Detectors, that are usually employed in accelerator experiments like ionization chambers or semiconductor detectors do not meet these requirements, since the dead times of these detectors and the time it takes to read out the data on line is too high.

While the development of detectors, that will provide data on line is on going [52], standard detectors for this application are film detectors and solid state nuclear track detectors, that store the information of the deposited energy. These are read-out later and are usable usually only for a single laser shot. The detector types that were used during the measurements will be described now in more detail.

4.4.1. RadioChromic Film detectors

RadioChromic Films (RCF) are self-developing films that were designed for the measurement of absorbed dose of high-energy photons. The usefulness of these detectors for proton detection has been demonstrated in a number of experiments in laser plasma physics (see for example Refs. [53, 54]).

Apart from transparent support layers of polyethylene terephthalat, also known as Mylar, each film contains one or more layers of an active dye. Being exposed to radiation, colour and optical density of this layer change depending on the radiation dose they were exposed to. Reason for this is a polymerization process that takes place after the irradiation and is described in Ref. [55]. The result is an increase of the absorption in the spectral range at around 660 nm wavelength in the active layer. High doses are visible directly by a change of the colour of the detector. Figure 4.6 shows the cross section through one of the detectors of the type HD-810 and an example of such a radiated detector. For the quantitative determination of the dose that was absorbed by the detector, the films are scanned with a trans optical scanner, producing uncompressed 48 bit RGB TIFF files. The RCFs were calibrated as described in Ref. [56] and IDL scripts were used for the post-processing and the transformation of RGB value to an absorbed dose. With known average deposited energy of the particles this transfers to the number of detected particles.

In order to achieve a coarse energy resolution stacks of RCFs can be used. Since protons reach the highest energy deposition right before stopping in the so-called bragg peak, the amount of the deposited energy is dominated by the particles that

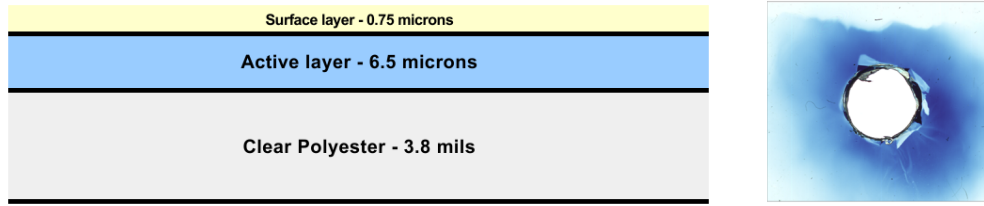


Figure 4.6.: Cross section of RCF detector type HD-810 (3.8 mils correspond to 97 μm) and an example of an irradiated detector of that type.

are stopping in the active layer. In case of HD-810, if the stack is wrapped in $\approx 13 \mu\text{m}$ of aluminium to prevent them to be irradiated by the laser light, these are protons of about 1 MeV in the first layer and 3.1 MeV in the second layer.

To calculate the particle density on the detector an estimation has to be made about the average deposited energy per particle. This differs much for different energy distributions of the incoming particle beam. Laser plasma sources typically produce protons with exponential energy distributions. Figure 4.7 shows the spectrum of deposited energy in the first and second layer of a stack of HD-810 detectors, assuming an exponential energy spectrum of the incoming particles, as described in section 5.3. With a given dose D the deposited energy per cm^2 in the active layer of

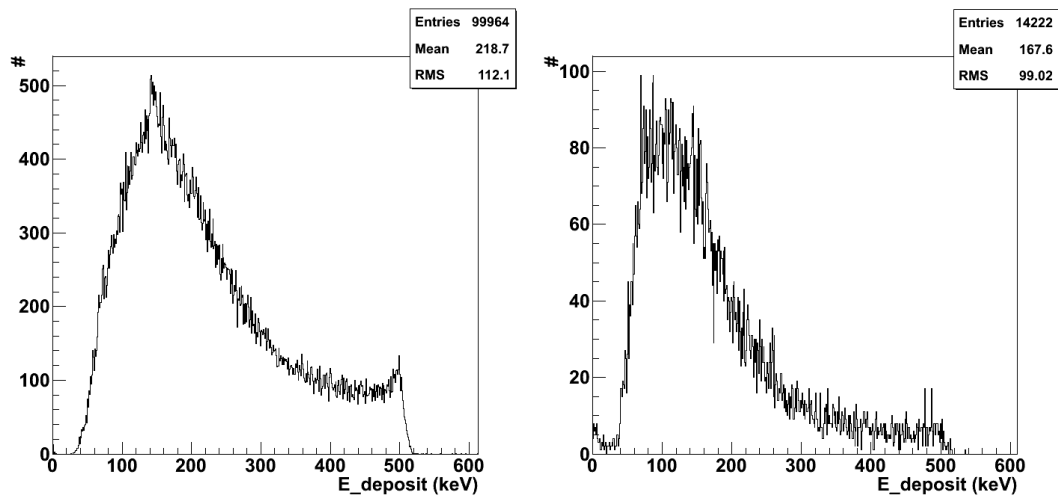


Figure 4.7.: Distribution of energy deposition in the first and second layer of a stack, assuming an exponential distribution of the start energy $e^{-0.9E[\text{MeV}]}$.

the thickness Δz can be calculated. Assuming an average deposited energy E_{av} of 219 keV, as indicated from the simulation, the number of protons n_p that impinged

4. Experimental methods

on the surface can be obtained:

$$n_p = \frac{E_{\text{deposit}}}{AE_{\text{av}}} = \frac{D\rho\Delta z}{E_{\text{av}}},$$

where ρ is the density of Mylar.

4.4.2. CR-39 detectors

The plastic polymer **allyl diglycol carbonate**, known under the abbreviation CR-39 ¹ was patented in the year 1940 and has been used as a recorder of particle tracks for a wide range of applications, especially heavy charged particles and fission products, but also for the measurement of α activity, detection of neutrons and protons [57]. An important feature for the application of CR-39 detectors in this measurements was its insensitivity to light and X-rays.

When irradiated by a beam of massive charged particles, each particle causes strong damage to the chemical structure of the polymer close to the particle trajectory. It is distinguished between the core, the region of high damage due to interaction with the primary particle and the surrounding halo. The precise mechanism of how the damage in the polymer structure of the halo region takes place is not yet resolved. The “ion explosion spike mechanism“ [58, 59] explains this by the repulsion of the positively charged ions, that have been left after the particle has passed, while other sources see the cause mainly in the knock-off electrons or δ -electrons produced by the primary particle [60]. The latter is a good description for the track formation if an energy cutoff is applied to the energy of the δ -electrons, which leads to the definition of the restricted energy loss REL:

$$\text{REL} = \left(\frac{dE}{dx} \right)_{W \leq W_{\text{cutoff}}} = \frac{Z^2 e^4 n_e}{4\pi \epsilon_0^2 m_0 c^2 \beta^2} \left(\ln \frac{2m_0 c^2 \beta^2 W_{\text{cutoff}}}{\bar{I}(1 - \beta^2)} - 2\beta^2 \right),$$

where Z is the charge of the incident particle, β its velocity, m_0 the rest mass, n_e the number of electrons per unit volume, \bar{I} the average excitation potential of electrons in the stopping material and W_{cutoff} the maximal value of transferred energy. This is the well-known Bethe-Bloch-formula, restricted to a maximal value W_{cutoff} of energy that is transferred to the electrons. In case of particles with a few MeV per nucleon this cutoff energy is assumed to be 350 eV [61].

In the regions affected by the δ -electrons the properties of the material like density, molecular weight distribution and solubility change [62]. With a suitable etchant, such as sodium hydroxide solution these regions will dissolve in the corrosive fluid faster than the surrounding material.

¹which stands for “Columbia Resin #39”, since it was the 39th formula for the plastic developed by the Columbia Resins project

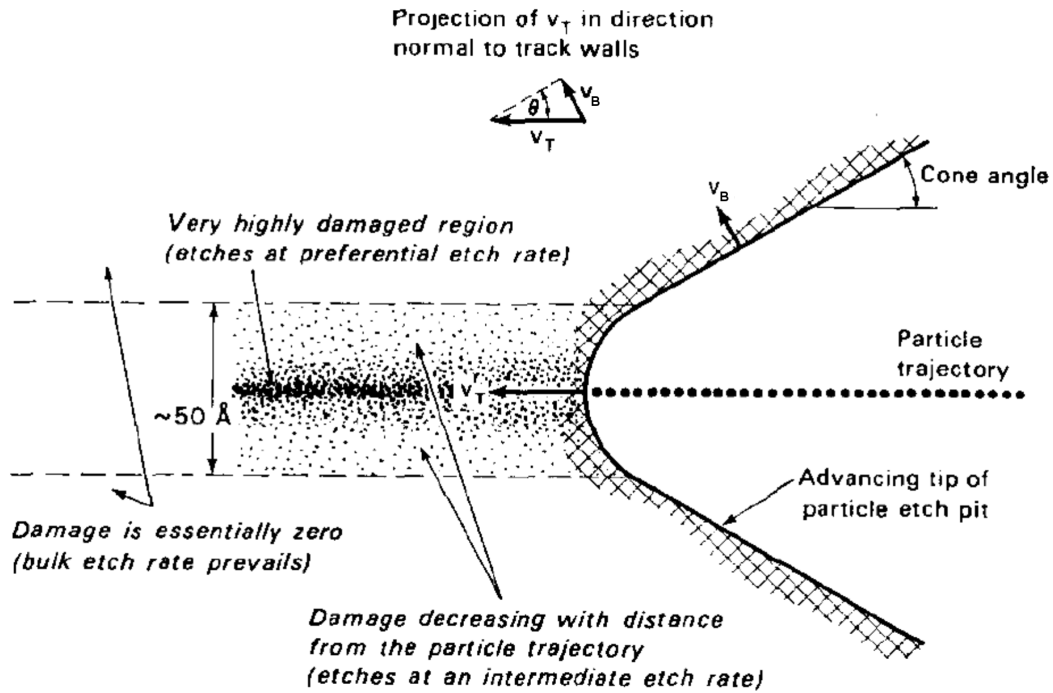


Figure 4.8.: Illustration of track formation during the etching process [60].

The whole surface is etched at a constant etch rate, the so-called **bulk etch rate** V_B , which is typically a few μm per hour. Along the particle trajectories the etching takes place at an enhanced rate of V_T , the **track etch rate**. V_T is proportional to the degree of damage in the material and therefore a function of the restricted energy loss REL in the halo region of the track. The result is a cone-shaped etch pit in the surface of the material, with an opening angle of $\theta = \arcsin(V_B/V_T)$. If the detectors are etched a sufficiently long time the etch pits are enlarged enough to be seen under a microscope, like shown for an example of 3 MeV protons in Fig. 4.9(a). The formation of a track due to the different etch rates is illustrated in Fig. 4.8. Because of the dependency of the track etch rate on the restricted energy loss V_T increases with the depth until it reaches its maximum in the region of the bragg peak of the respective particle and decreases very fast afterwards. If the etching goes beyond the range of the particle, the tracks will still increase in diameter but decrease in depth until they vanish. Figure 4.9(b) shows the development of the track with increasing etching time.

An important quantity for the detector response is the etch efficiency

$$\eta = 1 - \frac{V_T}{V_B} .$$

4. Experimental methods

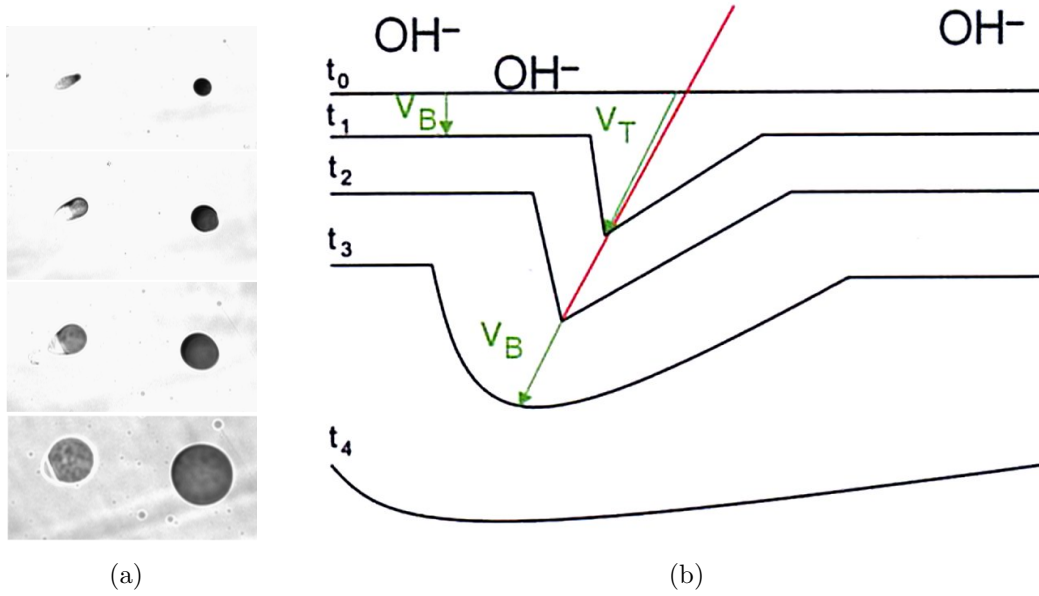


Figure 4.9.: (a): Proton particle tracks under a microscope. (b): Track development with etching time [63]. In red the particle trajectory is indicated, with green arrows the etch velocities V_B and V_T .

Bulk etch rate and track etch rate show a strong dependency on the temperature:

$$V_B = C_B e^{-E_B/k_B T}$$

$$V_T = C_T e^{-E_T/k_B T},$$

with C_B, C_T being constants, E_B, E_T the activation energy for the respective etching processes and k_B the Boltzmann constant. The activation energies have been determined by Rana and Qureshi [64] as $E_B \approx 0.939$ eV and $E_T \approx 0.310$ eV. Considering this, the etch efficiency has a maximum at 60° and decreases for higher temperatures. Studies of the dependency of the etch rates have also shown a decrease with increasing concentration of the sodium hydroxide solution [64]. For some practical reasons, like maintaining a constant concentration and temperature during the etching procedure it is desirable to have higher etch-rates and therefore lower etching times. For a solution of 7.25 mol/l at 70°C the efficiency still is greater than 93%. Additionally, for this etching configuration detailed measurements of track diameters and etch rates of protons in the energy region of one to eight MeV have been performed by Dörschel et al. [65].

Although photons and high energy particles leave no tracks in the CR-39 detectors, gamma irradiation leads to an increase of the bulk etch rate, which alternates the track development, leading to enlarged final etch pits [66]. Irradiation with light

from ultraviolet to infrared was also reported to affect the ratio V_T/V_B [67, 68, 69]. As a consequence, lead shielding in the experimental setup was necessary, whenever the detectors were located near the laser target during measurements to protect the material from the radiation of the plasma.

The detectors were read out with a readout system purchased by TasImage. Main part of the system is an optical microscope with a magnification factor of 20 and a green LED as light source. For the recording of the tracks the detectors are positioned on a microscope slide that is movable in the plane with stepper motors. Images are acquired of an area of $625 \times 470 \mu\text{m}$ at a time via a CCD camera mounted on the microscope, the images have a resolution of approx. $0.82 \mu\text{m}$ per pixel. Every picture taken is analyzed by the software "TasImage" for particle tracks. To find tracks the grey-level is measured and where a region is found with a sufficiently high grey level, the software registers an event. By adjusting the gain of the camera the contrast of the pictures can be increased to enhance the probability that a track is declared as an event. During the measurements a gain of 95 has proved to be efficient although this also increases the background, which has to be reduced later by post-processing. Each event is further analyzed and a number of parameters are saved that can be used to characterize the track and to draw a conclusion about the origin of the track. In Fig. 4.10 the parameters are illustrated at a schematic track shape. Most important for track selection are the major and minor axis of the ellipse that is formed at the surface, labeled as MAJ and MIN respectively. In case of high incident angles the parameter XT exceeds MAJ and is used instead. The parameter labeled with m in Fig. 4.10 indicates if the trajectory of the particle continues within the material, in which case the size of m is about a few μm . If the stopping point of the particle has been reached by the receding surface level m starts to grow as the cone of the track flattens out, the tracks also tend to become circular. If the major axis exceeds the value of $40 \mu\text{m}$ or falls below $3 \mu\text{m}$ the tracks are discarded by the software.

As in the case of other kinds of detectors reduction of the background is an important issue for solid state nuclear track detectors as well. It can be distinguished between background that is caused during the analysis of the pictures by the software, if impurities are considered tracks and background due to actual tracks in the surface, that were not produced by the particles that were to be detected.

The camera on the microscope will identify impurities on the surface as events if the grey level is dark enough, therefore the detectors have to be handled carefully and rinsed thoroughly with distilled water before scanning. Nonetheless there is a high level of background tracks with very small track diameters. These events are not rejected by the software but can be selected by post-processing of the data. By increasing the etching time until the actual tracks outgrow the background and rejecting the events with small diameters this background can be efficiently sup-

4. Experimental methods

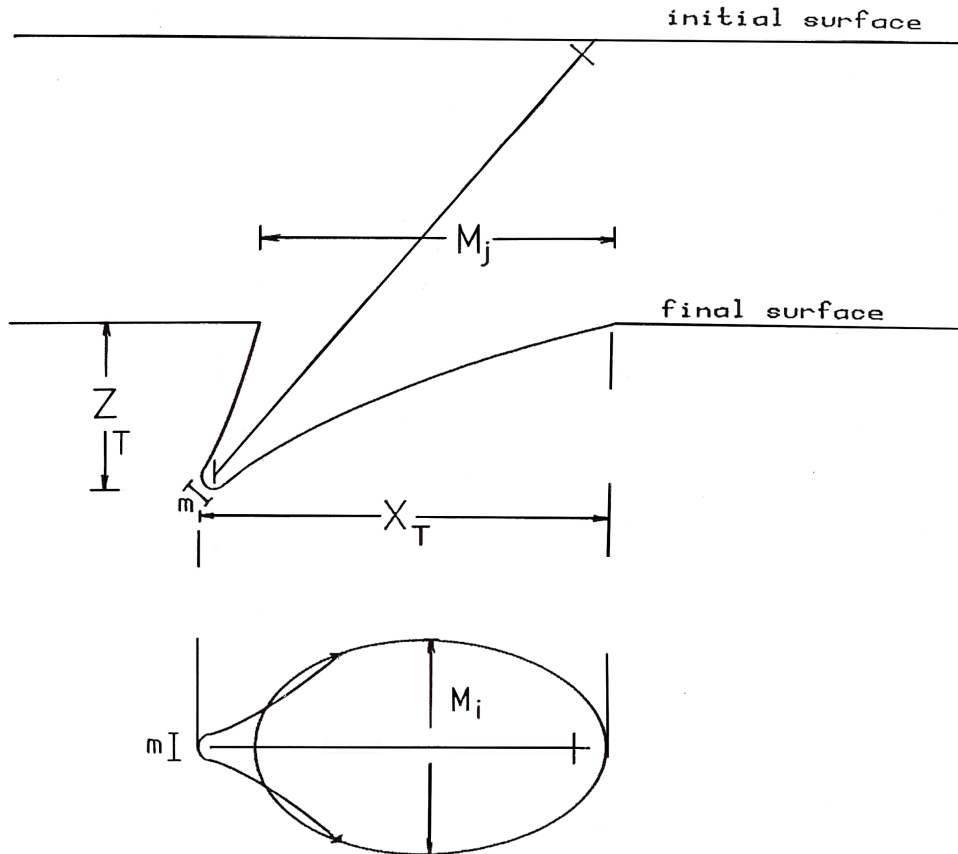


Figure 4.10.: Schematic illustration of the parameters of a particle track, that are saved by the software “TasImage” [70].

pressed.

Since the detectors record every particle during their lifetime the background includes tracks that originate from natural radioactivity, especially from radon sources in the air. The detectors are therefore delivered by the company in airtight aluminium packaging to prevent an increase of background signal during shipment and storage. For the purpose of this measurement the α background posed no problem. Due to the short range and the high energy deposit along the trajectory, tracks from α particles grow to diameters of more than $40 \mu\text{m}$ much faster than the proton tracks and can therefore be identified and rejected.

A usual way to depict the parameters of particle tracks is shown in Fig. 4.11. The frequency of occurrence of the parameters MIN and the larger of MAJ and XT is plotted for the case of a CR-39 plate that was irradiated with a radium source. Alpha tracks and the background can be distinguished. After 14 hours of etching with a concentration of 7.25 mol/l and a temperature of 70°C the tracks of the α

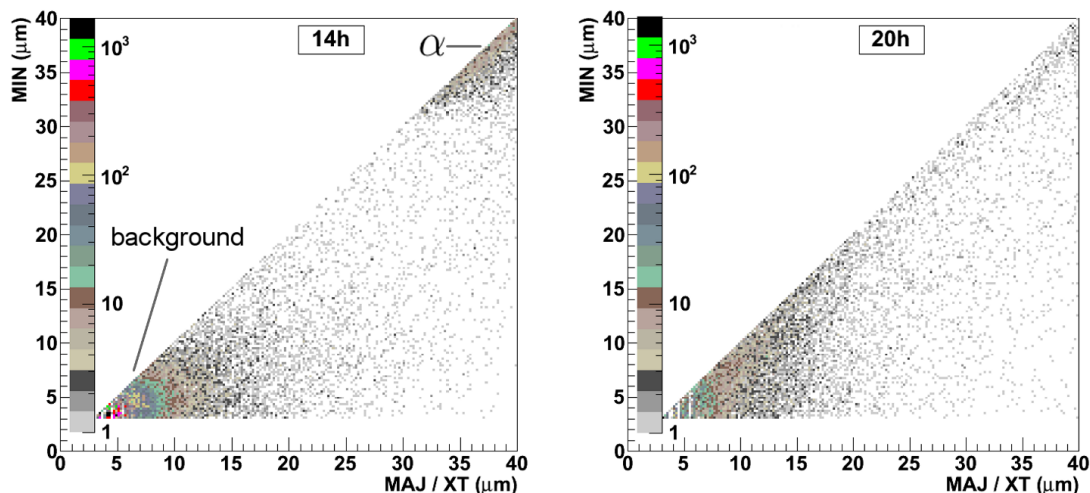


Figure 4.11.: Distribution of the parameters MIN and MAJ / XT for etch times of 14 and 20 hours.

particles are still detected, while the majority of the tracks is not detectable by the software if the etching time exceeds 20 hours. Particle tracks from protons of incident energies between 3 MeV have reached track diameters of 20 to 30 μm after this etching time [65].

Even after rejection of these tracks there is a constant background noise. The major part of these tracks stems from defects on the surface [71], which produce tracks that grow with the etching time like the proton tracks. To minimize this background the detectors have to be pre-etched before used in the experiment, until the background tracks are big enough to be rejected by the analysing software.

4.5. Magnetic spectrometer

Since the method of stacking RCF detectors provides only a very rough energy resolution for small protons energies, the method of momentum spectroscopy by means of a homogeneous magnetic field was adopted. Nevertheless the RCF detectors were used to monitor the particle rates for each shot, since the measurement of the spectrum and the polarization cannot take place during the same measurement. An electric dipole magnet that supplies the necessary momentum resolution was either too big to fit in the vacuum chamber or would have to be operated with a current that was unpractical to use inside the vacuum. Although kapton foils of 50 μm thickness are capable of withstanding a pressure of 2.5 bar and would therefore be suitable for a safe vacuum window, a significant part of the proton spectrum would

4. Experimental methods

be stopped in the foil. Also, estimations with Geant4 have shown that multiple scattering in air would lead to high uncertainties of the energy measurement of the protons. Therefore it was necessary to design and build a spectrometer magnet that could be placed inside the vacuum chamber.

4.5.1. Design and assembling of the dipole magnet

Permanent magnets of neodym were used to provide high magnetic field strength at a compact dipole size. The dipole magnet is H-shaped with a gap of 2 cm and length of 30.6 cm. It consists of an overall of 24 neodym magnets of 5.08 cm x 5.08 cm x 2.54 cm that are placed in the return yokes of magnetit. In order to obtain the highest feasible field strength, the software Pandira was used to calculate the optimum shape of the return yokes. Figures 4.12(a) and 4.12(b) show the flux of the magnetic field and the perpendicular component of the field, respectively. Instead

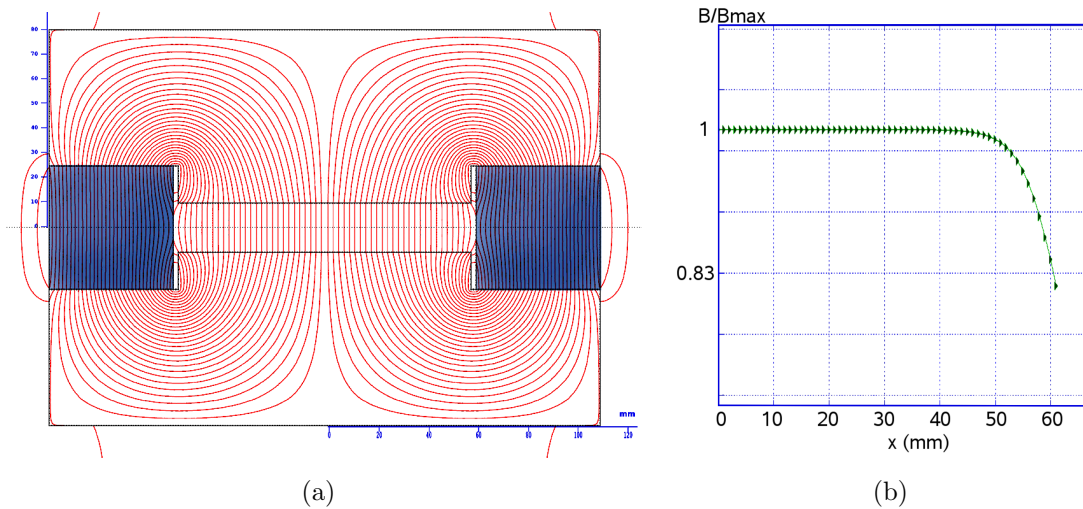


Figure 4.12.: (a): Cross section of the dipole magnet (blue: permanent magnets) with lines of magnetic flux as calculated with Pandira, (b): vertical component of the magnetic field.

of designing pole caps to improve the shape of the field at distances of more than 40 mm away from the middle axis it was decided to place the detectors within the homogeneous part of the magnetic field.

Each of the 24 single magnets, that are installed in the dipole are strong enough to sustain a weight of approximate 100 kg if attached to a metal surface. Therefore assembling of the magnets in the return yoke proved to be a mechanical challenge, since it was necessary to place several of these magnets with the same orientation next to each other. By dividing the return yoke into six segments it was possible to first assemble each segment with 4 magnets, like depicted in Fig. 4.12(a), which

does not pose a problem because in this configuration the magnets are pulled to each other and to the magnetit so that no other mechanical attachment was necessary. After building six of these segments they were forced in one row by putting an all-thread rod in prefabricated holes at each corner of the segment and slowly pressing them together by turning four pairs of counter-rotated screw nuts before the first and after the last segment.

4.5.2. Field measurements and calibration

A map of the magnetic field strength inside of the gap and in front of the dipole was created and is depicted in Fig. 4.13. The distance between individual measurement points is 1cm.

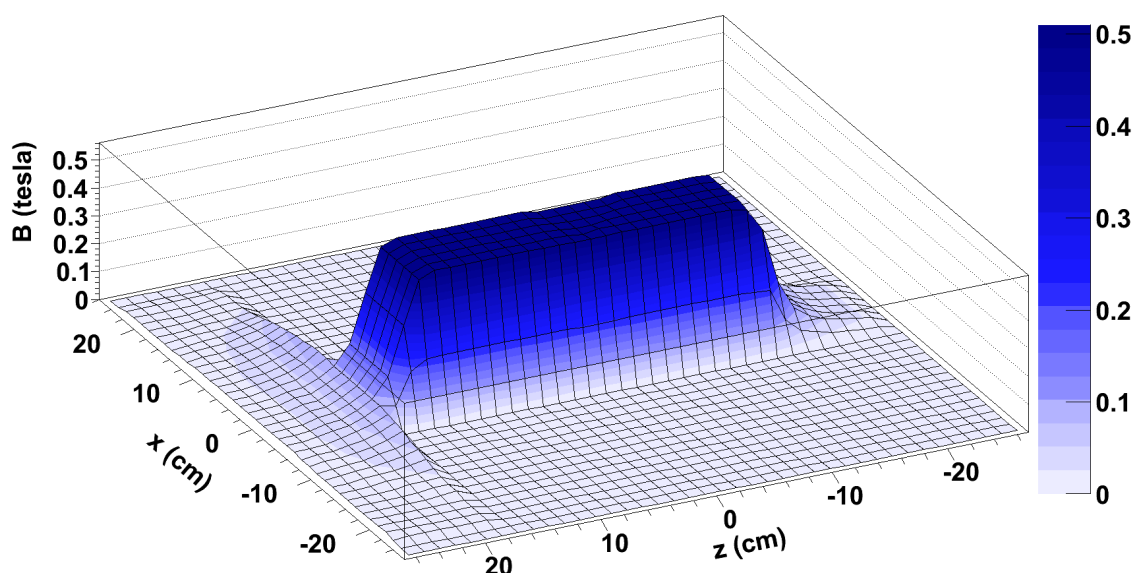


Figure 4.13.: Measured distribution of the vertical field component B_y of the dipole magnet with stray fields.

In the homogeneous area of the gap the field strength is 0.505 ± 0.05 T. The variation of field strength along the symmetry axis can be explained by differences between the single permanent magnets which have been arranged compensational to minimize this effect. Due to these stray fields in front of and behind the magnet the effective length of the magnet is 34.8 cm.

Since a box-field approximation cannot fully take into account the stray fields of the dipole, the calibration curve of the particle energy depending on the proton deflection

4. Experimental methods

was obtained by a simulation. To determine the kinetic energy E in dependence of the deflection z and the spectral resolution of the spectrometer for a given setup, a field map of the spectrometer was measured and embedded in a Geant4 program by means of the G4MagneticField class. For the tracking in Geant4 the field strength was interpolated linearly between the data points of the field strength measurement. Figure 4.14 shows the calibration curve obtained from the simulation for a distance of the spectrometer to the source of 56 cm and an aperture of 2 mm of the entrance collimator.

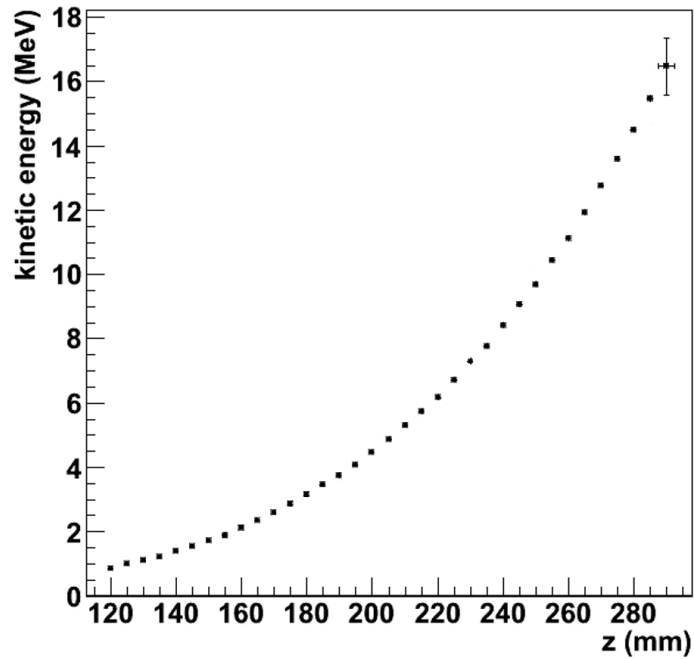


Figure 4.14.: Calibration curve for the estimation of the kinetic energy depending in the deflection z . The error bar indicates the energy spread of protons with this deflection in z -direction.

5. Düsseldorf laser facility ARcturus

5.1. Laser system

The measurements were carried out with the laser facility ARcturus at the Institute of Laser and Plasma Physics (ILPP) of Heinrich Heine University, Düsseldorf. This

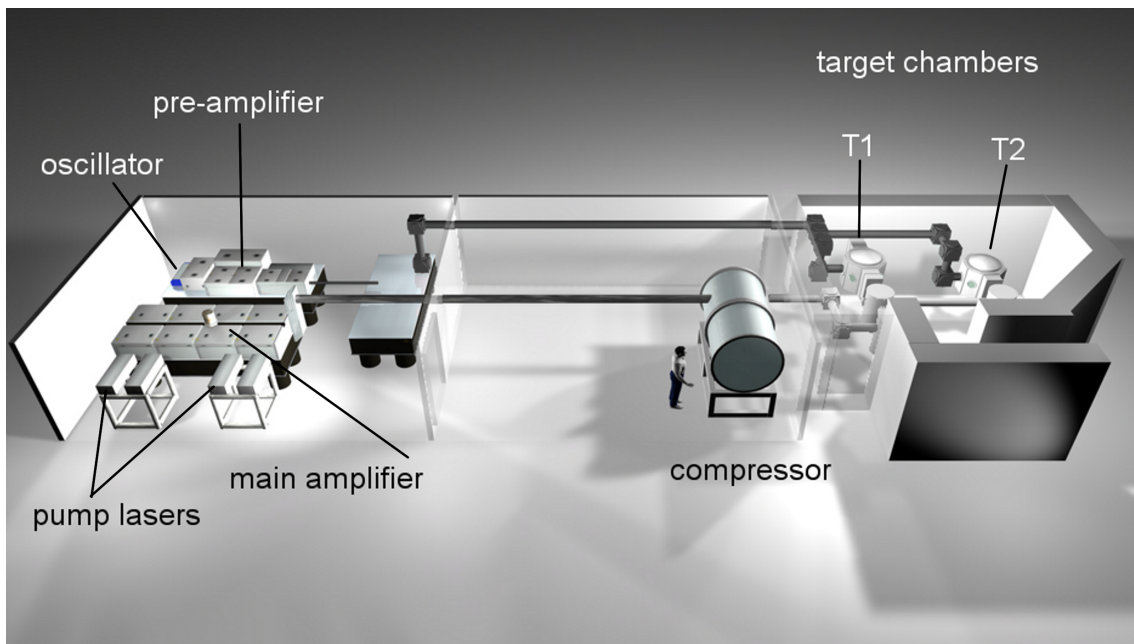


Figure 5.1.: Schematic view of the laboratory of the Düsseldorf laser facility [72].

is a commercial PULSAR-100 system by Amplitude Technologies. At the time of the measurements described in this thesis, a single beam line providing maximum pulse powers of 100 TW at pulse durations of about 30 fs was available. ARcturus employs the CPA technique to produce high intense pulses and therefore the main parts of the system are the oscillator, the stretcher, the amplifier, consisting of three stages, and the compressor. The oscillator delivers a train of sub-20fs pulses of 4.5 nJ energy at a repetition rate of 75 MHz. Between oscillator and stretcher the booster preamplifies the pulses and reduces the repetition rate to 10 Hz, which is the limit given by the pump lasers. A saturable absorber cleans the pulse from spontaneous emission background produced in the oscillator. In the stretcher the

pulse is expanded to a pulse length of 600 ps. Core of each multi pass amplification state is a Ti:sapphire crystal pumped by Nd:YAG lasers. At each stage the beam is lead through the crystal several times, amplifying the power of the pulse to 18 mJ and 300 mJ after the first and second stage, respectively. The Ti:sapphire crystal of the third multipass amplifier is cryogenically cooled to decrease the thermal lens effect in the material. The pulse contains 3.2 J, when it leaves the third stage and enters the compressor. From this point, the beam line has to be evacuated, since the pulse intensity after compression is sufficient to produce a plasma out of air. By means of high reflective, gold-coated gratings the pulse is compressed to the designated pulse length, the lower limit is 23 fs. Depending on the quality of the coating, up to 80% of the energy is transmitted to the target. Assuming a Gaussian-shaped intensity profile at the focus point with a FWHM of 10 μm , a maximum intensity at the target point of $5 \cdot 10^{20} \text{ Wcm}^{-2}$ can be reached. The laser system can be operated in one-shot mode during the measurements or at lower power with a repetition rate of 10 Hz in adjustment mode [73].

5.2. Target chambers

After the pulse has left the compressor, it is directed to one of the two target chambers, which are identical in construction, but vary in the kind of target that is installed inside. The chambers are evacuated to 10^{-4} mbar before the shutters to the compressor are opened.

In the plasma chamber T1 the laser is focused on a gas jet target, producing an underdense plasma. These targets usually are used to produce electron beams.

All the experiments, that took place in the frame of this thesis were carried out with solid targets in the overdense plasma chamber T2. Here the pulse is directed onto a thin foil target. Since an overdense plasma reflects the light similar to a mirror, vertical incidence of the laser beam would bring the risk of reflections back through the compressor and into the amplifier, which would cause serious damage in the material. Therefore the target normal is tilted to the axis of the incoming laser beam at an angle of 45° .

Each target chamber is equipped with an optical system, the so-called focus diagnostics, to find the precise focus position and to monitor the shape of the intensity profile in the focus point in adjustment mode for focus optimization. The chambers are octagonal and every side can be opened to add extension boxes that house diagnostics systems, that do not fit inside the chambers. Figure 5.2 shows a schematic top view of chamber T2 with focus diagnostic, dipole and the paths of the laser beams. The place of the setup for the polarization measurement is indicated by the rectangle.

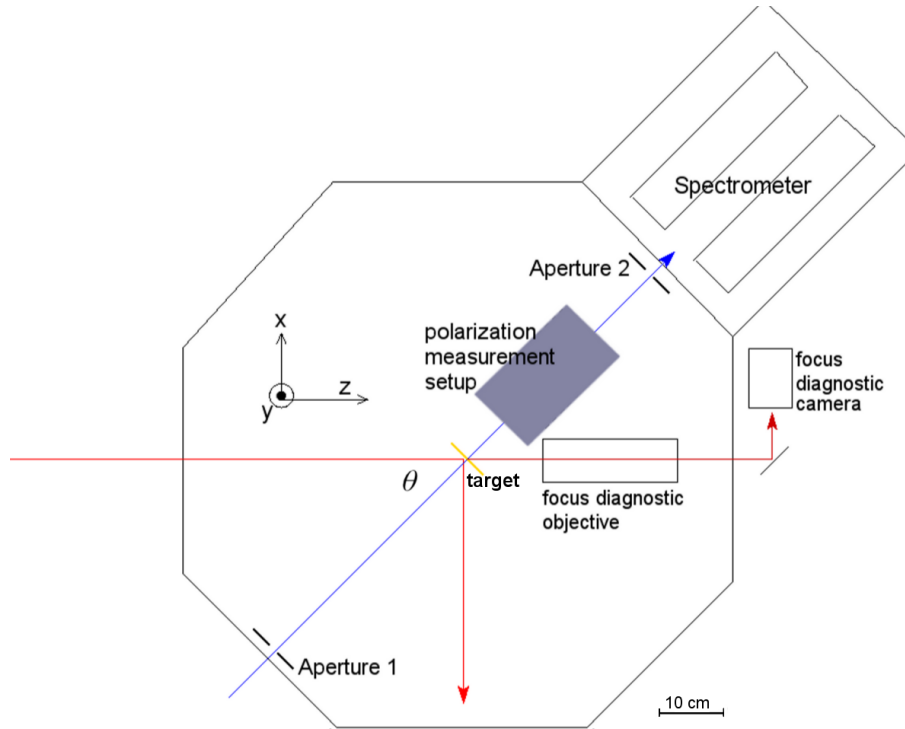


Figure 5.2.: Top view of the solid-target chamber T2, the path of the main laser beam is indicated by the red line, the blue line shows the path of the continuous laser for the spectrometer adjustment and the polarization measurement setup.

5.3. Proton production

For the production of the proton beam the laser was directed on a gold foil target of $3 \mu\text{m}$ thickness. The target had a typical lateral size of a few mm and was attached to a target holder with which it could be moved in two dimensions and rotated around the z -axis. Since the targets are not perfectly plane each of them had to be fine adjusted, to the nominal incident angle of 45° . Apart from this it is also crucial to position the target precisely in the focus point of the laser beam to provide the maximum light intensity inside the plasma. The steps during the adjustment procedure were:

1. The target is moved approximately to the focus point, so that it reflects the continuous adjustment laser, indicated by the blue line in Fig. 5.2. This axis is defined by two apertures (labeled with 1 and 2 in the figure). By tilting the target holder around the z -axis until the light is reflected back through the aperture 1 the incident angle $\theta = 45^\circ$ is adjusted.
2. While the laser focus is optimized during the adjustment mode, the target is

5. Düsseldorf laser facility ARCTurus

moved out of the beam path. After the optimization the lens of the focus diagnostic system is focused on the interaction point.

3. The target is moved in place again for the fine adjustment of the target position. First the target is moved in the x - and z -direction until the edges can be seen sharp by the focus diagnostic system.
4. Then the target is moved until it covers the beam and the intensity is increased just enough to burn a small hole of a few μm in the target.
5. The position of the target is adjusted until the edges of the hole are sharp, then the target is moved $\approx 100 \mu\text{m}$ upwards. This is used as the shot position.
6. While the target is temporarily been removed from the focus point by moving it in y -direction, the focus can be optimized with help of the focus diagnostic.

The energy that was delivered on the target amounts to approx. 1.2 J, the intensity profile at the focus point was of Gaussian shape with a full width half maximum (FWHM) of $7 \mu\text{m}$, which is monitored by the focus diagnostic during adjustment mode.

Energy spectrum of the laser-accelerated protons

While stacks of RCF detectors were used by as on-line beam monitors during each shot, a higher resolution measurement of the energy spectrum has been carried out, using the spectrometer described in Sect. 4.5. The spectrometer was aligned parallel to the target normal at a distance of 56 cm. With an aperture of 1 mm radius a solid angle of 10^{-5} sr was defined for the beam entering the spectrometer. To obtain absolute particle numbers, CR-39 detectors were used and placed in the homogeneous region of the magnetic field. For the final spectrum several scans at different etch times of the detectors were averaged. Figure 5.3 depicts the raw data of one scan. As indicated in the figure, a region next to the radiated part of the detectors was used for background correction of every scan.

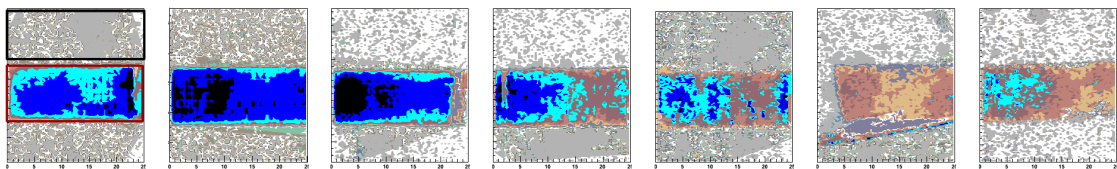


Figure 5.3.: Distribution of tracks on the CR-39, red and black rectangles indicate signal and background area, respectively.

An example of an obtained energy spectrum can be seen in Fig. 5.4. Like it is expected from the mechanism of Target Normal Sheath Acceleration, an exponential spectrum was observed with a tail of a low number of protons with energies up to 10 MeV. An exponential fit describes the data in the low-energy region, in which the polarization measurements were carried out (*i.e.* around 3 MeV).

During a later measurement with a beam energy of approx. 1.9 J the shape of the

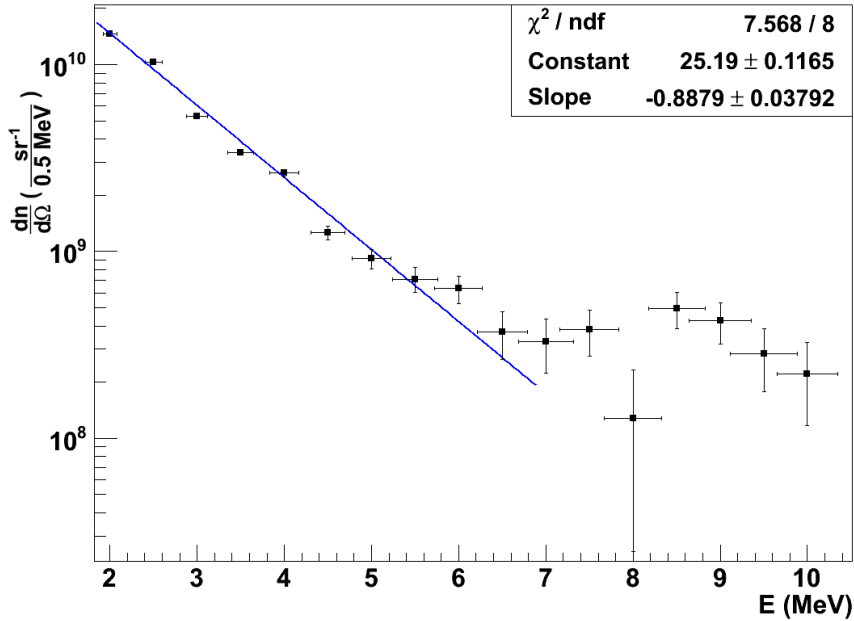


Figure 5.4.: Energy spectrum of the protons obtained with CR-39 and magnetic spectrometer.

spectrum could be reproduced, which confirms that the proton energy distribution is not affected by variations of the laser power during the polarization measurements. Since the higher pulse energy leads to an increase of the proton number per solid angle by nearly an order of magnitude, a signal, usable for a coarse energy determination, from the second and third layer of the stack of RCF detectors was observed. The number of protons in the given energy ranges was obtained by scanning the calibrated detectors as described in Sect. 4.4.1. Figure 5.5 shows the first 3 layers of the RCF stack, the extracted peak doses are given for every layer. It can be seen that protons, that were accelerated to higher energies are also more collimated, resulting in a smaller spot on the detector. The values of the dose were determined in all three layers at the point of the apparent center of the beam in the first one. The spectrum obtained from the doses is depicted in Fig. 5.6. Given the inhomogeneity of the angular distributions the slopes of Figs. 5.4 and 5.6 are in good agreement.

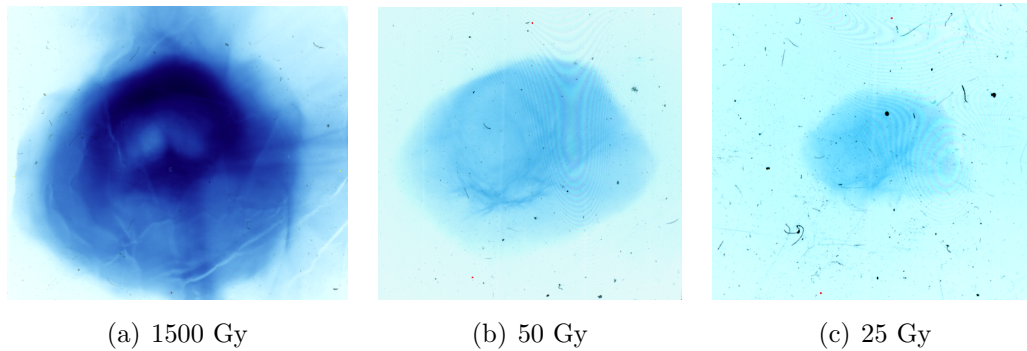


Figure 5.5.: Three layers of a stack of RCF detectors irradiated with protons from a $3 \mu\text{m}$ thick gold target. The doses at the beam center are given for each layer.

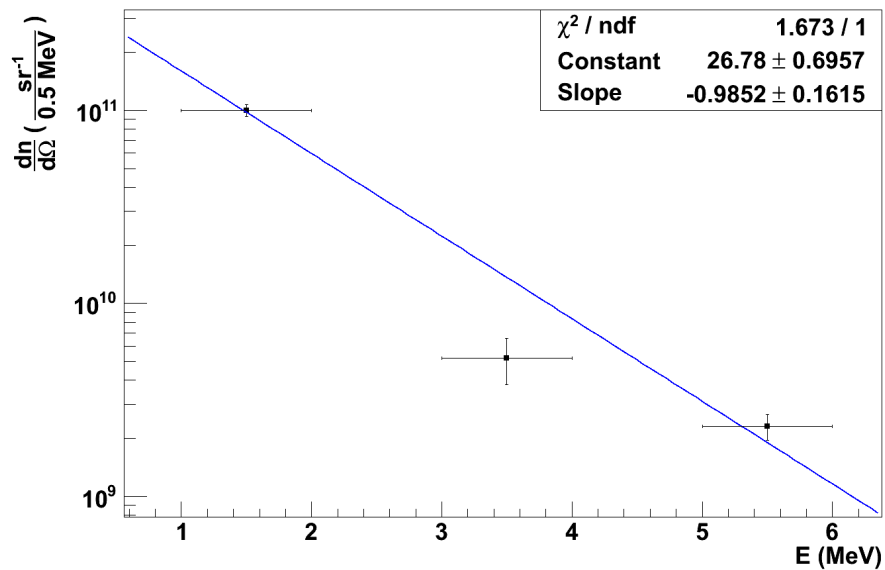


Figure 5.6.: Energy spectrum according to the RCF data of the second measurement at higher laser-pulse energy of 1.9 J.

6. Particle-in-Cell simulations

6.1. Methods and input parameters

For the simulation of the processes in the foil target the program BOPS was used, which employs the method of the relativistic boost technique and was described in Sect. 4.1. While the reduction to a one-dimensional code minimizes the computational effort for each simulation run, for polarization studies it is necessary to explore the radial field gradients, for which one dimension is not sufficient. A workaround for this issue is to start several one-dimensional runs with intensities that correspond to the distribution at different distances from the symmetry axis of the laser beam, like illustrated in Fig. 6.1. In the simulation program the target normal is by default parallel to the x -axis and the electric field of the laser beam points in direction of the y -axis. This convention is used here, while in the other chapter the z -axis is defined as the direction of the incident beam. At the focus point the laser spot is assumed to have a two-dimensional gaussian intensity profile. The magnetic field

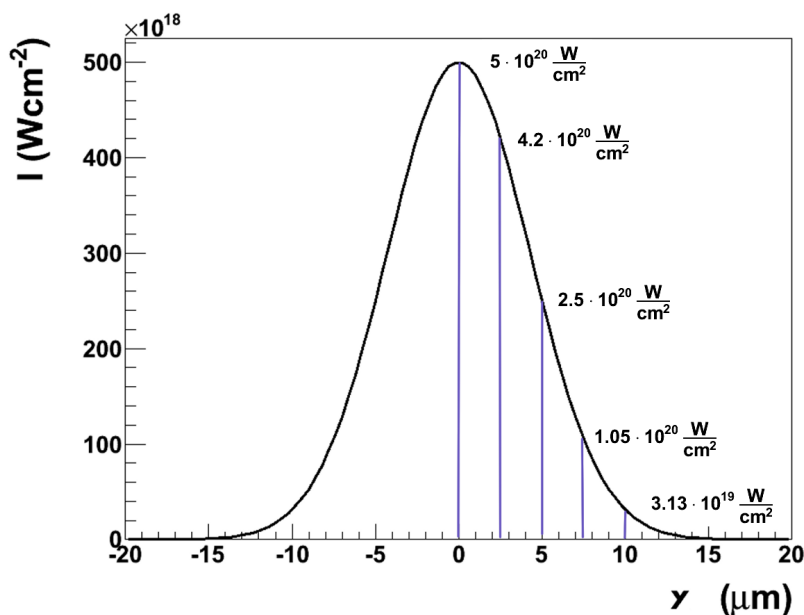


Figure 6.1.: Intensity profile of the laser beam at the focus point. The intensities, for which separate runs have been started are shown.

6. Particle-in-Cell simulations

gradients can be approximated as the difference of the magnetic field strength in two different runs at a fixed point in y -direction. The protons on the target back-side are accelerated in x -direction due to the quasi-static electric field produced by the hot electrons at the same time as they are accelerated by the magnetic Stern-Gerlach force in radial direction. To obtain the acceleration in the lateral direction, the force that operates on the protons has to be integrated over the period of time in which it effectively works. This is the time the protons need to pass through the magnetic fields. Assuming constant acceleration up to a final velocity v_{fin} the average velocity parallel to the beam axis of a proton can be approximated with $v_{\parallel} = v_{\text{fin}}/2$. The lateral velocity then can be calculated as

$$v_{\perp} = \frac{1}{m_p} \int F dt = \frac{\mu_p}{m_p v_{\parallel}} \int \frac{\partial B}{\partial z} dx .$$

Integration along the x -axis starts right behind the target foil and ends at the end of the simulation box, which is the approximated path of the protons, possible lateral components have been neglected. Prestudies have shown, that the magnetic fields are adequately static and do not decrease significantly until the protons have left the field region.

The proton trajectory is deflected by an angle of $\vartheta = \arctan \frac{v_{\perp}}{v_{\parallel}}$. Therefore it is expected, that the deflection of the protons will decrease with increasing final velocity. A program for the automatic start of a set of runs and the integration of the magnetic field gradients has been developed in the scope of a diploma thesis at the Institut für Kernphysik (IKP) [74].

The runs have been started on the parallel processor JuRoPA at the Jülich Supercomputing Centre for high resolution and to simulate a sufficiently high number of particles. For this study a target configuration has been chosen that resemble the experimental conditions at the laser laboratory in Düsseldorf:

- Peak intensity of the laser pulse: $5 \cdot 10^{20} \text{ Wcm}^{-2}$
- Pulse length: 30 fs
- Incident angle: 45°
- Target thickness: $3 \mu\text{m}$
- FWHM of the lateral intensity distribution in the focus point: $10 \mu\text{m}$

At the side of the target away from the incident laser pulse a layer of protons is added to imitate the impurities usually found on foil targets.

6.2. Results

Figure 6.2 depicts the quasi-static magnetic fields that have evolved 150 fs after the start of the simulation run. At this point in time the laser has already been reflected by the plasma and the electrons have been expelled from the target. The protons start to gain kinetic energy in the quasi-static electric fields behind the target.

In the simulation program the magnetic field B is normalized to $m\omega_0/e$, with m being the electron mass, ω_0 the laser frequency and e the electron charge. For a laser wavelength of $0.8 \mu\text{m}$ and a normalized peak field as seen in Fig. 6.2 this gives a maximum field strength of $5.5 \cdot 10^4 \text{ T}$, right behind the laser plasma target at the full intensity. For half of the intensity, which corresponds to a distance from the focus center of $5 \mu\text{m}$ the field strength decreases by a factor of 2. The magnetic field gradient at this point is approx. $5 \cdot 10^6 \text{ Tm}^{-1}$. Since exponential proton spectra were observed during the measurement (see Sect. 5.3), the deviation angle was calculated for a broad range of final kinetic energies, see Fig. 6.3.

The expected deflection angles are several orders of magnitude too small to be observed, especially considering the fact, that the proton beam itself has an angular divergence of about 20° . For the measurement described in Sect. 7 it is therefore expected, that no polarization is observed and this experimental conditions can serve as a null-measurement. If, however, a polarization was observed, the effect of the magnetic field gradients are not able to serve as an explanation.

6. Particle-in-Cell simulations

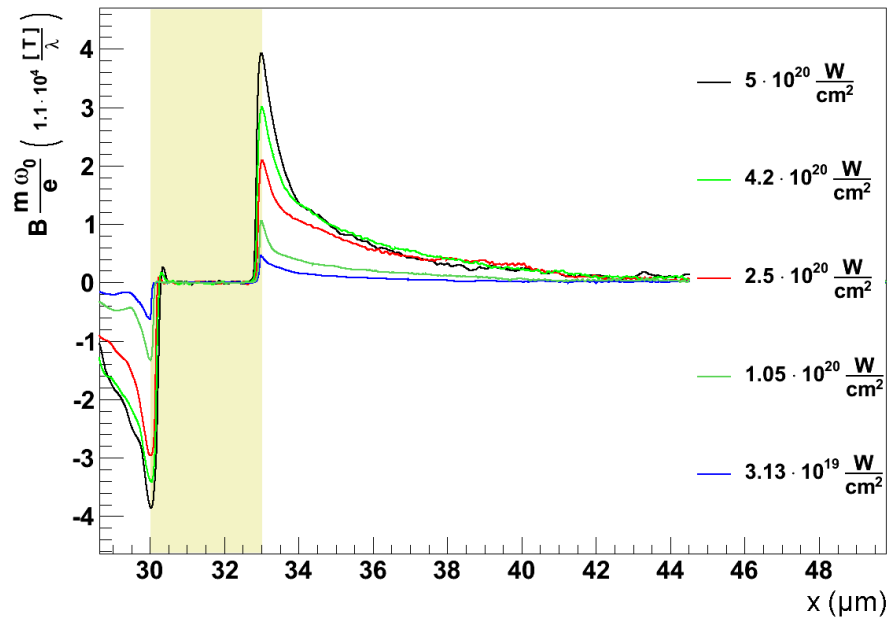


Figure 6.2.: Magnetic fields behind the target for different peak intensities, the foil target is located at $30 < x < 33 \mu\text{m}$.

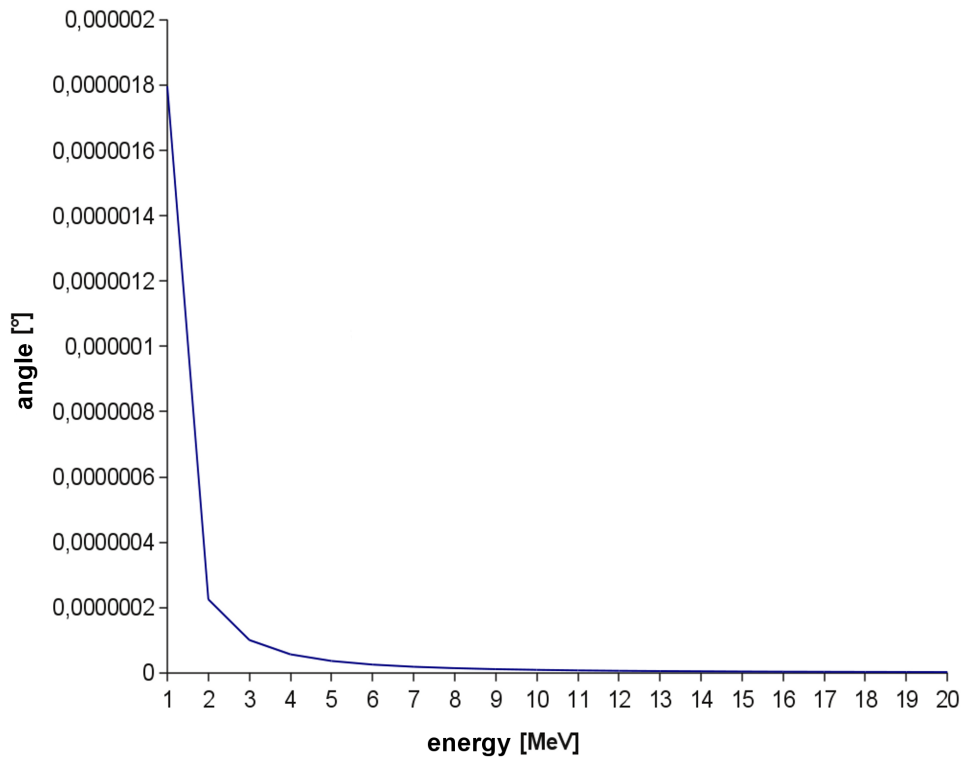


Figure 6.3.: Calculated deflection angles for several different kinetic energies [74].

7. Spin polarization measurement

To measure the degree of polarization of the proton beam, the spin dependence of the elastic proton scattering off silicon nuclei was used. Data for the analyzing powers and cross sections of the reaction $\text{Si}(p, p)\text{Si}$ reaction were provided by measurements at the tandem accelerator at University of Cologne [49]. These data are described in more detail in Refs. [40, 75]. Their pre-processing is described in Sect. 4.3.

7.1. Setup

The principle of the setup is schematically depicted in Fig. 7.1, while 7.2 shows a 3d technical drawing. The proton beam is produced at the plasma target, ap-

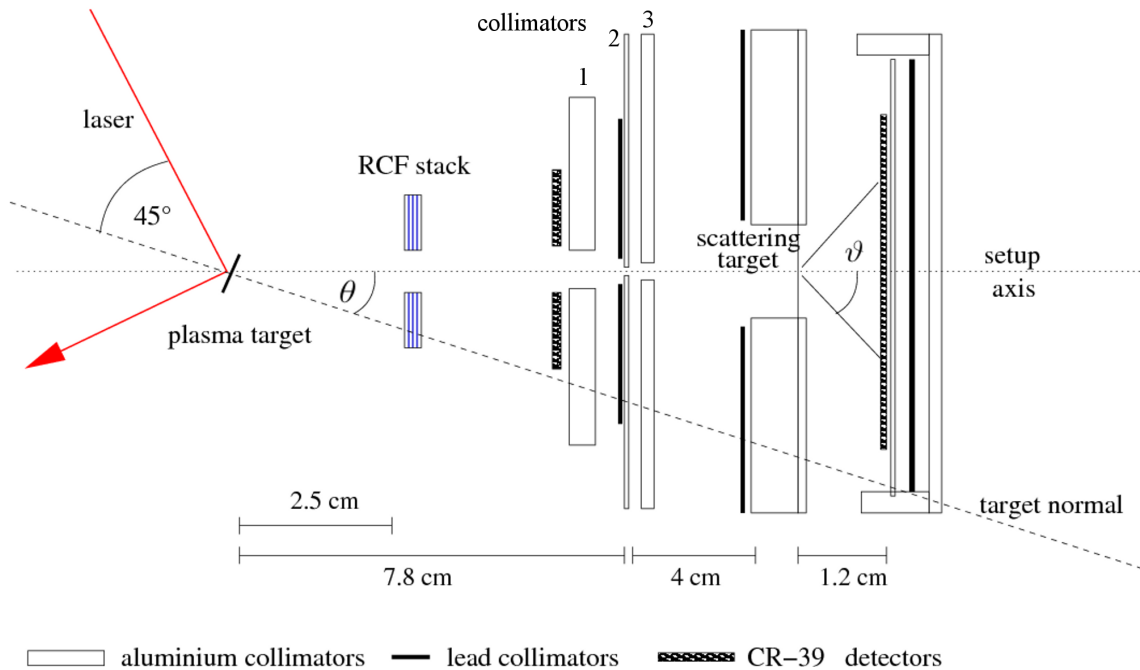


Figure 7.1.: Schematic view of the setup for the polarization measurement.

proximately parallel to the target normal with an opening angle of about 20° . The symmetry axis of the setup for the polarization measurement is inclined with respect to the target normal by an angle θ , that was varied in the range of 0° to 10° . At

7. Spin polarization measurement

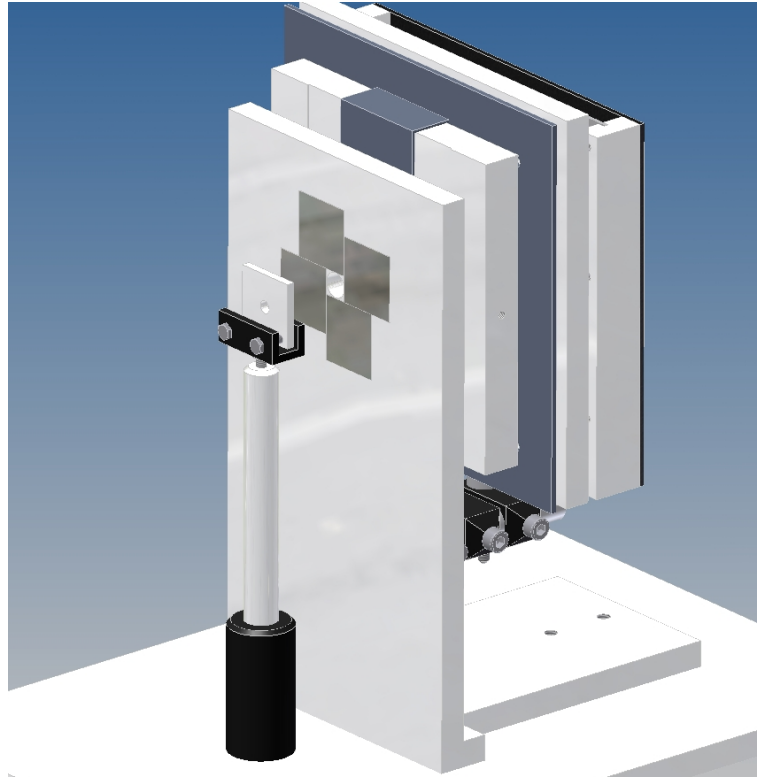


Figure 7.2.: Technical drawing of the measurement setup.

a distance of 2.5 cm from the plasma target a stack of RCF detectors is placed for the monitoring of the particle rates. Through a hole with 0.5 cm diameter a part of the beam passes the RCF detectors and arrives at a first set of collimators.

An aluminium collimator with an aperture of 0.5 cm in diameter and a collimator of lead with an aperture of 2.5 cm serve as radiation shielding. With a second aluminium collimator a part of the beam is selected and passes the hole of 1 mm diameter. The small thickness of 0.1 mm of this aperture to minimize the amount of solid material in the selected beam since scattering of the protons at the edges produces secondary particles, but protons up to energies of 10 MeV are stopped in the material. One centimeter behind this, the third collimator of aluminium with a thickness of 0.5 cm and an aperture of about 2 mm blocks any secondary particles that are still produced at the edges of the first collimator. More lead shielding is placed in front of the target holder for further reduction of the γ radiation background. For the scattering of the protons a silicon target of 24 μm thickness was used. The target rests in a 1 cm thick target holder, that serves as additional collimator. Particles that are scattered upstream at the collimator edges will most likely be absorbed in the material. The main beam to be analyzed has an angular divergence of approx. 1° and hits the target in an area of 2 mm diameter. Behind

the scattering target, detectors are placed, which cover a scattering angle ϑ of up to 68° and the complete azimuthal range ϕ from 0° to 360° . Solid state nuclear track CR-39 detectors have been used since the level of γ background radiation is high and is not detected directly by the CR-39. Still, the radiation on the CR-39 detectors might influence the track development during the etching process later (see Sect. 4.4.2), this is why the lead collimators were added to the setup. The beam spot of γ rays in the center of the detector does not extend to more than a circle of one centimeter in diameter, which is well below scattering angles of 30° .

The adjustment of the whole setup along the beam axis is achieved by laser alignment with a small continuous laser, 45° to the incident of the accelerating main pulse. It is useful to first adjust the foundation plate by taking out the target and replacing collimators and the detector with apertures. If the foundation plate is placed in a way that the laser beam passes through the apertures while they are almost closed, the collimators can be adjusted. The third collimator is adjusted, while the one in front is taken out. After that the front collimator is put in its place and the whole construction can be tilted for re-adjustment of the front collimator. Since the rotation axis of the two connected collimators runs through the aperture of the second one, the tilting will not cause misalignment. The detector and target holder is adjusted parallel to the collimator by measuring the distance on both sides.

7.2. Simulations

The simulation program *slap* (see Sect. 4.3) contains the complete setup for the polarization measurement with the collimator system. Its purpose is to model shots that have been made without the silicon target and to study the influence of multiple scattering on the lateral particle distribution on the detector. Several detector types can be chosen for the simulations without recompiling. If RCF-detectors are chosen, two-dimensional histograms are generated in the file “slap.root” in which the x,y distribution of the deposited energy in the active layers of the respective detector is given. In case of a CR-39 detector, which was the one used for the experiments, a text file is generated, that is similar to the output of the readout program of the CR-39 detectors described in Sect. 4.4.2, so that the ROOT scripts, that were used for the analysis of the data could be used just slightly altered for the simulated data as well. The file contains the x - and y -distribution of the particle tracks on the detector and the kinetic energy at that point, which corresponds to the parameters MIN/MAX of the CR-39 tracks (Sect. 4.4.2). Also the vertex energy and the incident angle is given. The ROOT file that is generated by the program also contains several histograms for monitoring. A virtual detector in front of the silicon target monitors the number and x,y distribution of the protons that reach the target, as well as

7. Spin polarization measurement

the difference of start energy and the kinetic energy at the moment the particles reach the target. Figure 7.3 shows an example of the generated histograms, here in case of a vertical disalignment of the target collimator by 1 mm. The main beam

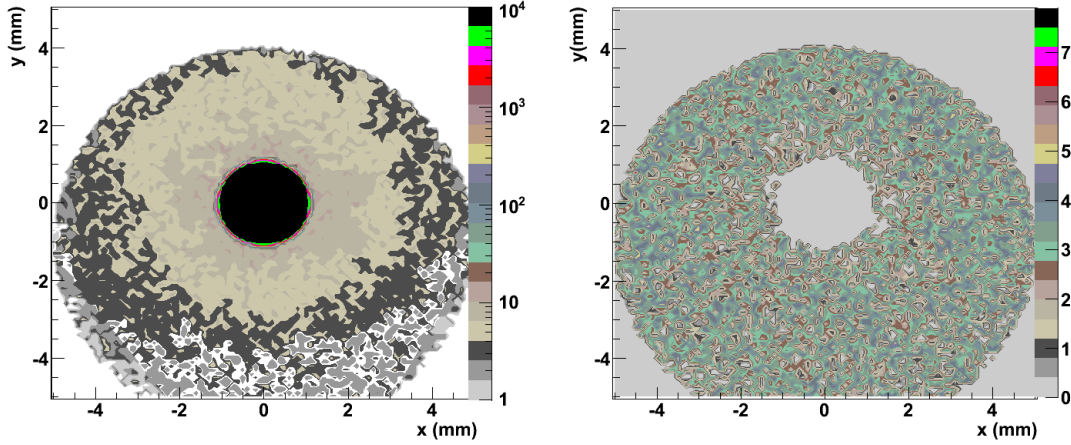


Figure 7.3.: (a): Distribution of the number of particles in the target, (b) distribution of the energy difference $E_{\text{start}} - E_{\text{kin}}$ of the particles that arrive at the silicon target.

coming from the first collimator can be seen as well as particles that are scattered and reach the silicon target in the outer region. The number of particles that reach the target outside of the area of the main beam spot is smaller by several orders of magnitude smaller. Also the energy of these particles is reduced by approx. 3 MeV. Only particles that have a remaining kinetic energy of at least 2.2 MeV, when they reach the detector, are relevant for the simulation because protons with lower energy will be rejected later during the analysis of the experimental data. Given that the particles in the outer regions still have to pass the target, the start energy would have to be in the range of 6 MeV or more. Since the plasma produces the exponential energy spectrum depicted in Sect. 5.3, the contribution of such particles can be neglected. From these histograms the number of particles that hit the target can be calculated, which is used as an input parameter for the simulation of the scattering in the next step with the program *sipol*.

The geometry of the program *sipol* consists of the silicon target and the CR-39 detector. All Geant4-processes apart from the LowEnergy-Ionization process are switched off. First the number of particles, that fall into this category have to be determined as a function of the number of particles arriving at the target. Since the available data for cross sections and analyzing powers is limited to the energy region $2.2 \text{ MeV} < E < 3.67 \text{ MeV}$ the number of incoming particles has to be restricted to this energy range. As given by Eq. (3.7), the number of particles that is to be

started in the second part of the simulation amount to

$$N = 2\pi\rho\Delta z \int_{E=2.2}^{E=3.67} N(E) \int_{\vartheta=30^\circ}^{\vartheta=70^\circ} \frac{d\sigma}{d\Omega}(\vartheta)\Omega(\vartheta)d\vartheta dE .$$

A run of the simulation program *sipol* is then started with this number of protons. The start energy of the protons before they enter the target is distributed according to the measured exponential energy spectrum. To obtain the proton energy just after the hadronic interaction, which will be referred to as the vertex energy, the energy loss of each particle until the interaction has to be taken into account. The coordinates of the vertex point are uniformly distributed within a cylinder inside the target, which has the same height as the target thickness and the radius of the beam spot on the target. Simulations with *slap* suggest, that the loss of kinetic energy can be approximated linearly, see Fig. 7.4(a). The vertex energy is therefore calculated with $E_{\text{vertex}} = E_{\text{start}} - p_1 z$ with the slope p_1 being obtained by a fit of the simulation data, see Fig. 7.4(b). The angle $\vartheta(E_{\text{vertex}})$, under which the proton is

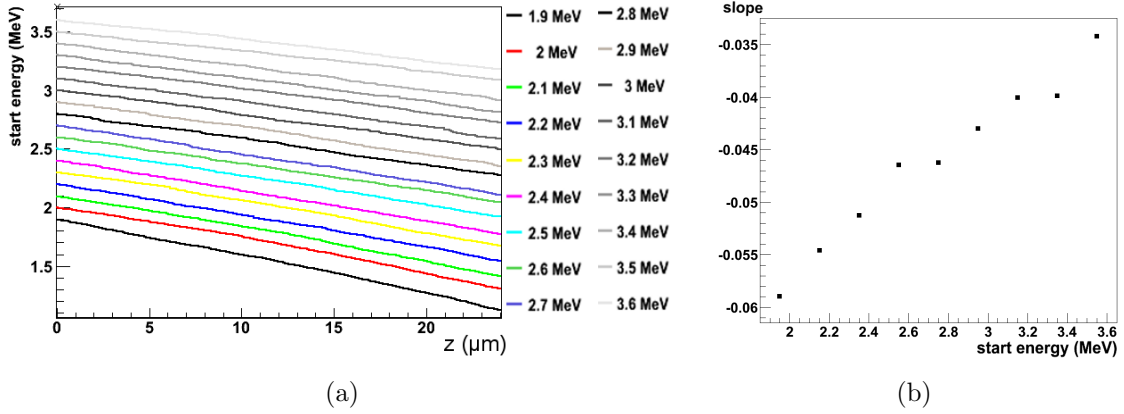


Figure 7.4.: (a): Kinetic energy of the protons in the target at different start energies, (b) fitted slopes.

started will then be distributed according to the cross section data provided to the program as ROOT histograms and the azimuth angle ϕ according to $(1 + PA \cos \phi)$ with $A(E_{\text{vertex}}, \vartheta)$ being the analyzing powers from the data, interpolated linearly from a two-dimensional histogram.

7.3. Results of the first measurement

During the measurement time in April of 2010 an overall of 16 shots were recorded. Apart from the measurement of the proton-energy spectrum, that is described in

7. Spin polarization measurement

Sect. 5.3, four of the measurements were carried out without silicon target at test of the calibration and background check. For six shots, including two without scattering target, the symmetry axis of the polarization measurement setup was at an angle of 45° with respect to the direction of incoming laser beam and therefore was intended to be parallel to the normal vector of the target surface. Another 6 shots obtained under 55° , thereof two without silicon and 5 shots at 53° , thereof one without the scattering target. For reasons, that will be explained in the next section in context of data analysis, some of the measurements were not usable. Six of the data sets contained useful information in all sub-detectors, as will be described in the following. A list of all measurements and their parameters is given in the appendix.

7.3.1. Processing the data from the CR-39 detectors

To obtain the angular distribution of the protons behind the scattering target, several analysis steps had to be carried out. First the CR-39 detectors were etched and scanned. As a second step the center of the angular distribution had to be determined and scratches and impurities were excluded from the data, to minimize background-induced asymmetries. Then the differential cross section of the scattering reaction was extracted and compared to the available data. Finally, the asymmetries along the azimuth angle ϕ was calculated for four quadrants of the CR-39 surface.

For each step a certain range of the kinetic energies of the incoming particles was selected. After a general description of the raw data and the energy selection, the steps will be explained in more detail.

7.3.2. Raw data

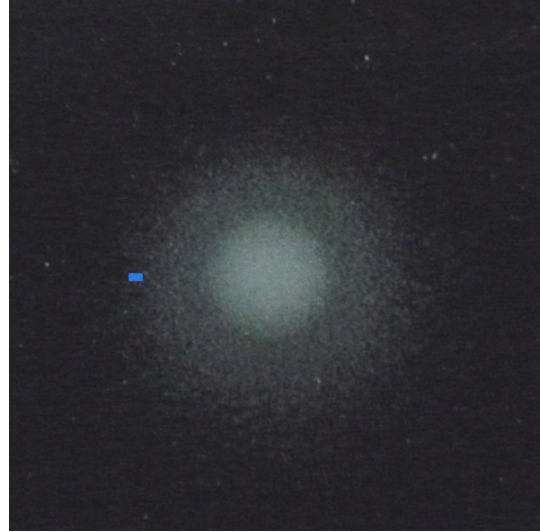
Even after etching, single particle tracks are not visible by eye, but if the track density is very high the CR-39 surface turns opaque. Figure 7.5 shows photos of the irradiated detectors and images taken by the microscope for measurements with and without the silicon scattering target.

In case of Fig. 7.5(a) protons in the whole energy spectrum, that is produced in the plasma target, arrive at the detector, while in case of a measurement with scattering target (Fig. 7.5(b)) particles of kinetic energies of less than ≈ 1.5 MeV are stopped in the silicon.

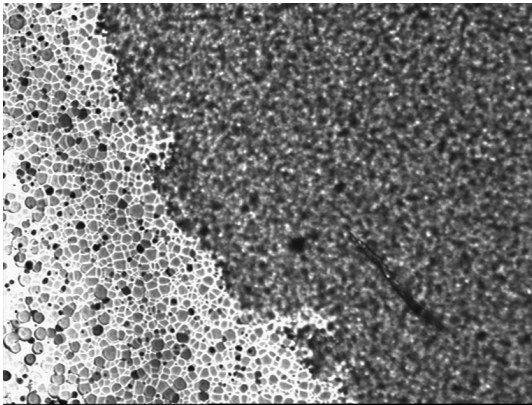
Within the direct beam area the detector is overexposed and it is not possible to identify any tracks. This can clearly be seen in Fig. 7.5(c). In the region between the beam spot and $\vartheta \simeq 20^\circ$, tracks can be identified and counted, but seen from Fig. 7.5(d), neighboring etch cones affect the shape of each other and analysis of the



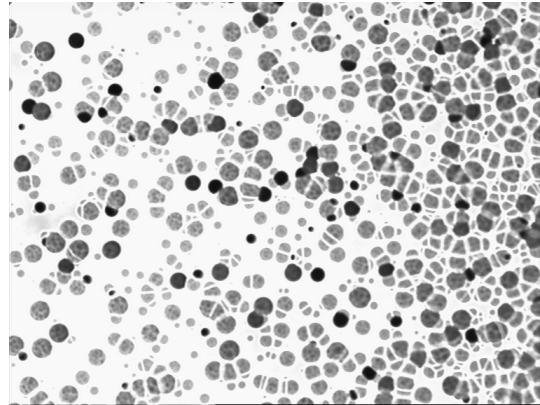
(a) CR-39 detector used in a measurement without silicon target



(b) CR-39 detector used in a measurement with silicon target



(c) Overexposed (upper right) region and region without the possibility to analyse the track parameters



(d) Transition to the region where tracks can be analyzed with the TASLImage software

Figure 7.5.: Top: photographs of two CR-39 detectors. Bottom: corresponding microscope images of $625 \times 470 \mu\text{m}$ size. The approximate location of the microscope image is marked in each photographs by the blue rectangle.

7. Spin polarization measurement

tracks depending on parameters like the major and minor axis is not possible in this region. For $\vartheta > 20^\circ$ the tracks are sufficiently separated to develop independently during etching times up to 30 hours.

7.3.3. Energy selection

The CR-39 detectors that were used in the polarization measurement were etched for 20 hours at 70°C and a NaOH concentration of 7.25 mol/l. The work of Dörschel et al. [65] was used to determine the energy of the detected particle according to the track diameters.

For the given etching conditions, with track diameters between 20 and $22\ \mu\text{m}$ kinetic energies between 2.8 and 3.5 MeV are selected, as indicated in Fig. 7.6. In this way a

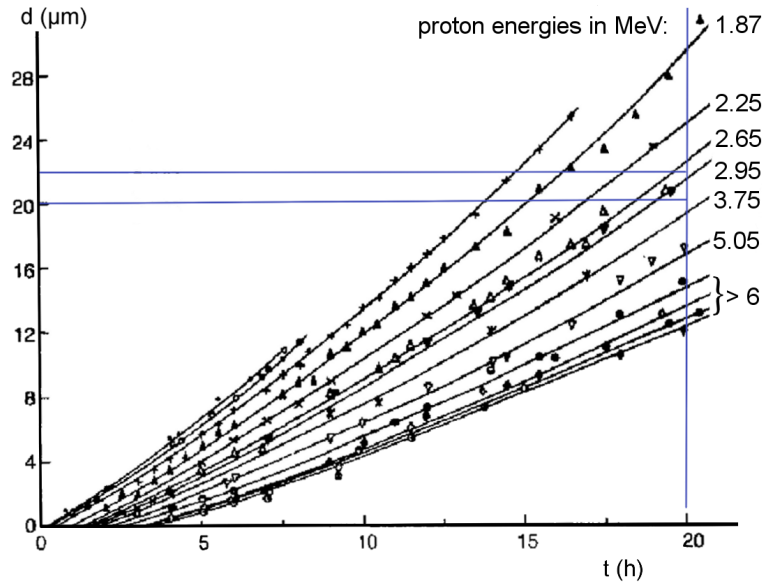


Figure 7.6.: Track diameters in dependence of the etching time for several incident energies by Dörschel et al. [65].

selection of the kinetic-energy range of the incoming particles is possible. Minimum track diameters correspond to a maximum energy and vice versa.

In order to obtain the kinetic energy of the particle at the time of the hadronic interaction, the energy loss along the path through the silicon target after the interaction has to be taken into account. Figure 7.7 depicts the distribution of this vertex energy for a $24\ \mu\text{m}$ silicon target, an assumed exponential energy spectrum of particles from the source, a selection of a kinetic energy at the detector between 2.65 and 3.5 MeV and scattering angles of more than 30° . The average vertex energy for this selection is about 3.2 MeV with a root mean square of 0.2 MeV. Uncertainties

during the etching procedure like variations in temperature and reading errors during the determination of the concentration give an additional systematical error of 0.3 MeV.

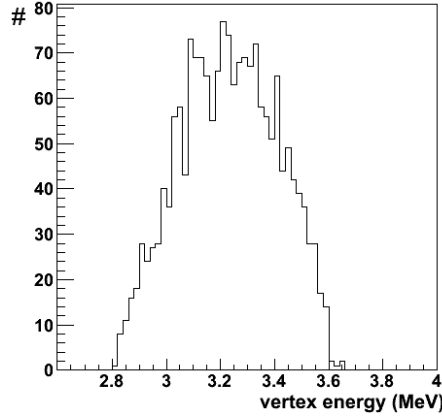


Figure 7.7.: Distribution of the vertex energy of protons that arrive at the CR-39 detectors with energies between 2.8 and 3.5 MeV.

7.3.4. Determination of the distribution center

To minimize false asymmetries it is necessary to accurately define the point of origin of the proton distribution (Fig. 7.7) for the calculation of the distribution along the azimuth angle ϕ . During the scanning process, the point of origin is by default the bottom left corner of the CR-39 plate. For the transformation of the coordinates $(x, y)' = (x - x_0, y - y_0)$ the coordinates of the center point (x_0, y_0) have to be determined.

Under the assumption that the Coulomb scattering of the protons is not spin-dependent, since the angular distribution of the coulomb-scattered protons is generated by multiple scattering processes, a range of ϑ , where this process is dominant, is used to find the true center of the distribution. Figure 7.8 shows the simulated angular distributions of the track densities for both, the multiple scattering and the hadronic interaction. Up to approx. 30° multiple scattering is the dominant process, while for higher scattering angles the signal of the protons from hadronic interactions becomes dominant. Angles between 20° and 26° were used for the estimation. For the center determination tracks with diameters between 15 and $30 \mu\text{m}$ were used, corresponding to protons incident energies between ≈ 1.8 and 5 MeV, while the low diameter background of the CR-39 detectors is excluded as well as potential α tracks. The ϕ angular distribution of the track density on the detector for an angular range of $20^\circ \leq \vartheta \leq 26^\circ$ and for a series of points (x_0, y_0) is obtained.

7. Spin polarization measurement

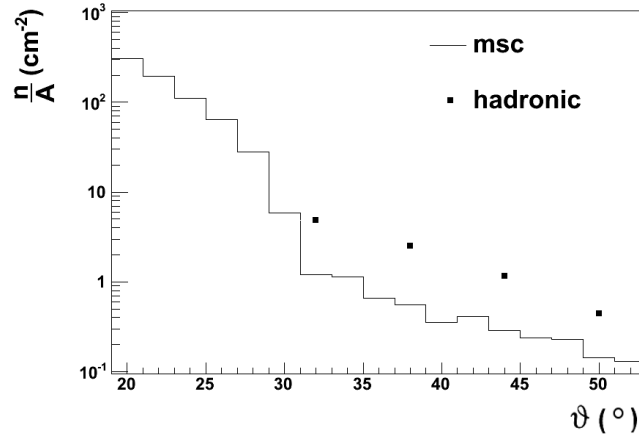


Figure 7.8.: Comparison of simulated track density originated by multiple scattering (msc) and hadronic scattering.

After fitting with a constant function the χ^2 of the data in comparison to the fitted function is plotted in dependence of $-(x_0, y_0)$ and the point of the minimum χ^2 is defined as the point of origin. Figure 7.9 shows examples of the χ^2 distributions depending on the two components of the assumed center point.

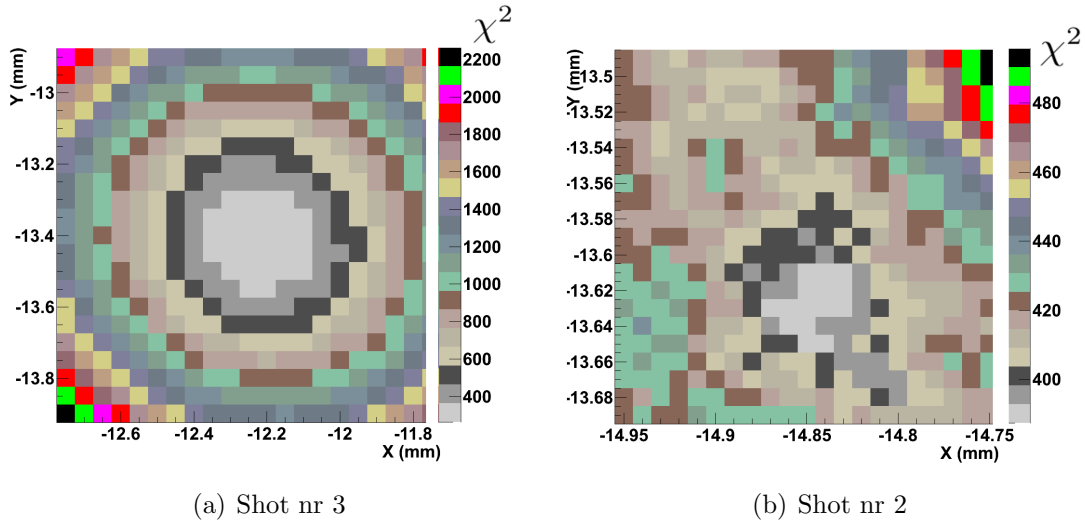


Figure 7.9.: Examples of χ^2 distributions in dependence of (x_0, y_0) for two different shots. The value of χ^2 is given in the palette.

The statistical error of the center determination is below $100 \mu\text{m}$, therefore, the influence of this error on hadronic asymmetries is negligible.

The second graph is an example of a detector, where the center part was destroyed

during the etching process. In this case a center point cannot be reliably determined, which might lead to the observation of an asymmetry that is caused by the geometrical contortion instead of polarization. Effects from non-homogeneous illumination of the scattering area are intrinsically compensated by the method.

After the center calculation the CR-39 detectors are checked for scratches and impurities. The overall background level was higher than expected on CR-39 detectors by a factor of four. Figure 7.10 shows 3 examples of the track density on the detector area. The first detector has a relatively constant background level. In the

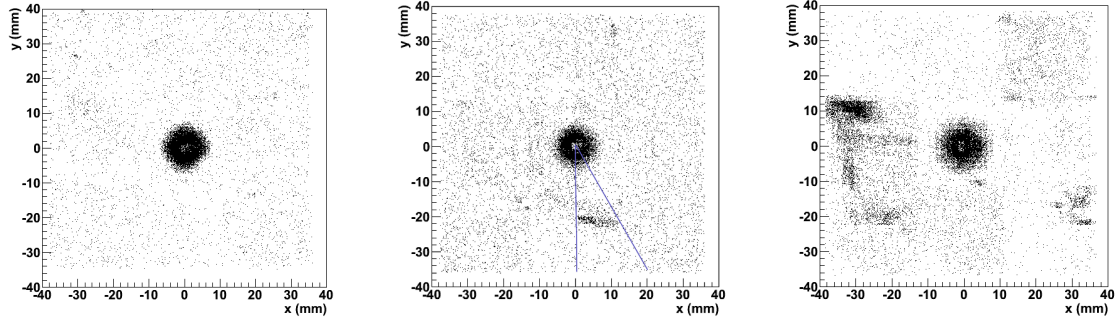


Figure 7.10.: Examples of different levels of CR-39 background.

second example a patch is visible on the detector. The area, that is excluded from the analysis because of this, is indicated by the blue lines. In the third image an example of a detector is shown that could not be used for the calculation of the asymmetry. It can be seen that several plates of the detector area had an increased background level and several large patches and more than a third of the area had to be excluded.

7.3.5. Determination of proton rates and calculation of cross sections

According to Eq. (3.7) the number of incoming protons n_0 can be calculated from the differential crosssection as:

$$\frac{\partial\sigma}{\partial\Omega} = \frac{\Delta n}{n_0 N_A \Delta\Omega} . \quad (7.1)$$

While N_A is given by the thickness and density of the silicon target in atoms / cm². Two methods have been employed to calculate n_0 , which will be explained and compared in this section. First, the number of particles n_0 , that arrive at the scattering target was evaluated from the dose on the RCF detectors that was recorded during each measurement, and second this was cross checked by a comparison of the data

7. Spin polarization measurement

on the CR-39 using the expectations according to the available cross section data. For the estimation of the asymmetries and, therefore, of the polarization, a precise determination of the absolute values of the cross section is not needed. Nevertheless, if both calibrations are in agreement, this indicates that the extraction of the proton data from the background of the detectors was successful.

The left side of Figs. 7.11 and 7.12 show the upper layer of the RCF detectors for 6 different shots. The corresponding dose distributions — along the red lines — are shown on the right. Beam center and center of the aperture are indicated by the black dots, the black circles serve as a guide to the eye, where the beam spot is assumed. In the dose histograms the center of the aperture in the polarization setup and the evaluated dose at this point are indicated. Since the angular distributions are very inhomogeneous the estimation of the dose of a point inside the aperture is afflicted with a sizable systematic uncertainty.

The RCF images were also used for the determination of the angle between the symmetry axis of the setup and the beam center, by a measurement of the distance between the center of the holes and the proton distribution.

In Table 7.1 the extracted doses and the errors of the estimation for the 6 shots are summarized. The angles between the symmetry axis of the setup and direction of the incident laser beam are given as well as the angles between setup and beam center obtained from the RCF detectors. The number of incident protons was also

Table 7.1.: nr: shot number, α_i : the angle between the setup and the incident laser beam, α_a : angle between symmetry axis of the setup and the proton beam center

nr	d (cm)	α_i (°)	α_a (°)	dose (Gy)
1	7.8	45	6.8	400 ± 50
2	7.8	45	3.4	350 ± 100
3	7.6	55	9.2	500 ± 100
4	7	53	13	200 ± 100
5	7	53	14	100 ± 50
6	7	53	16	200 ± 100

determined from a comparison of the data from the CR-39 detectors behind the scattering target and the cross section data from the measurement at the University of Cologne [49]. First the density of tracks with a diameter between 20 and 22 μm depending on the scattering angle is obtained. This corresponds to an average vertex energy of about 3.2 MeV. The background level of the track density n/A on the detectors is calculated by a χ^2 fit in the region of more than 50° , where the

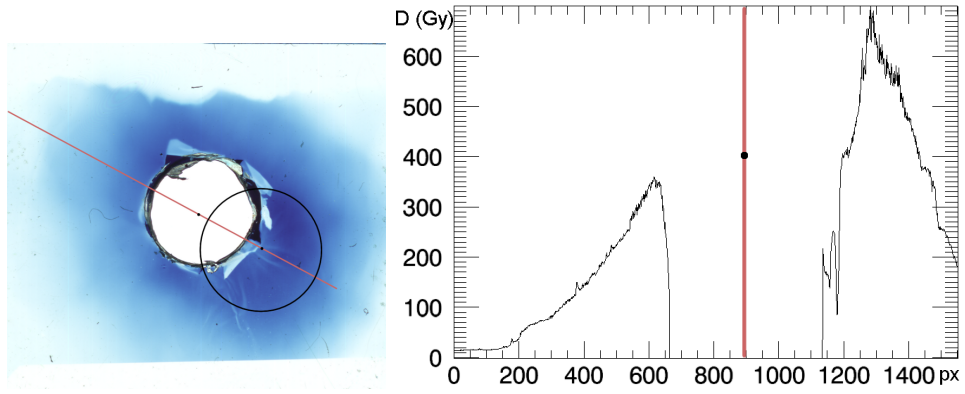
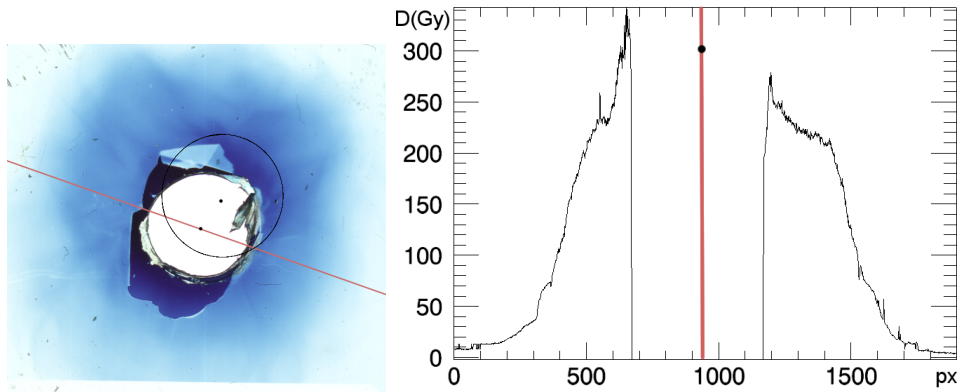
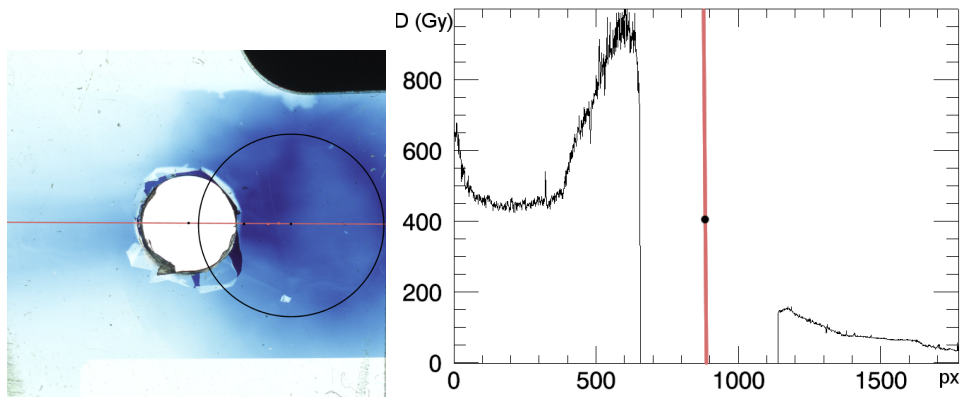
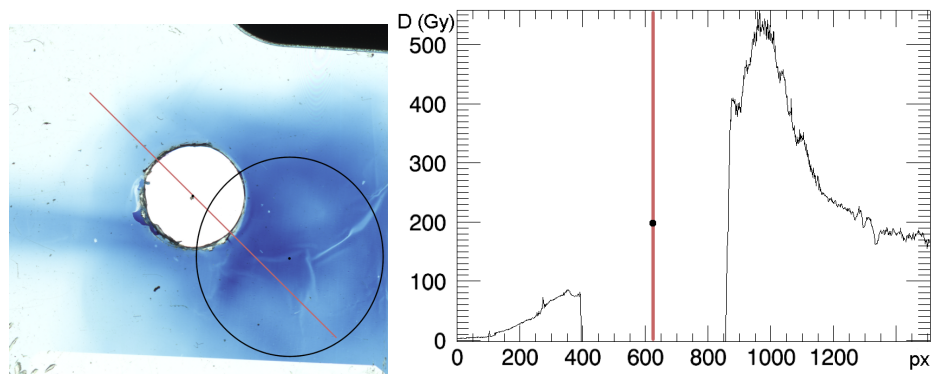
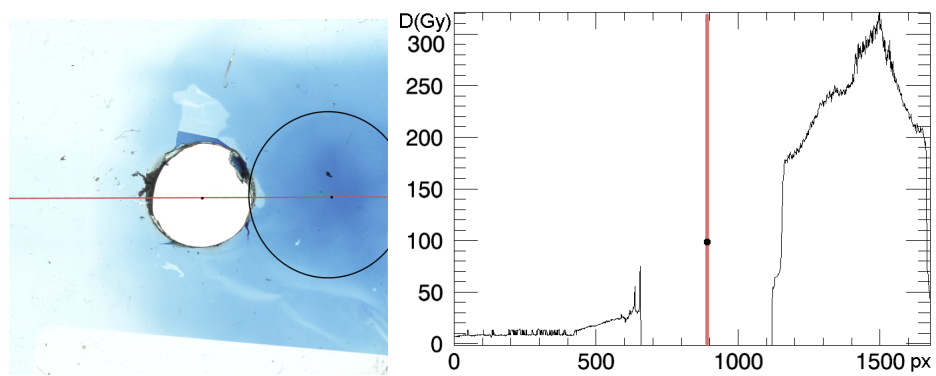
(a) nr 1, distance: ≈ 3.3 mm(b) nr 2, distance: ≈ 1.5 mm(c) nr 3, distance: ≈ 5.7 mm

Figure 7.11.: Left: top layers of the stack of RCF detectors. The approximate locations of beam and beam center are indicated with a black circle and dot respectively. Right: distributions of the absorbed dose along the red lines indicated in the images on the left. The approximate distance between the beam center and the center of the aperture is given for each shot.

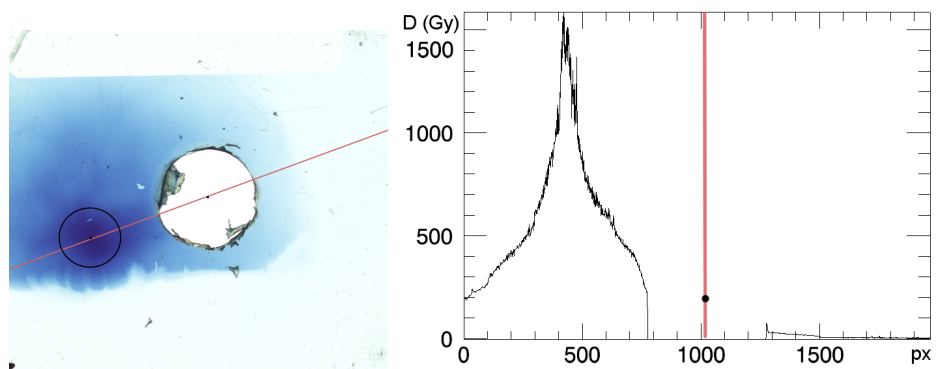
7. Spin polarization measurement



(a) nr 4, distance: ≈ 6 mm



(b) nr 5, distance: ≈ 6.3 mm



(c) nr 6, distance: ≈ 7 mm

Figure 7.12.: Same as Fig. 7.11 for three different shots.

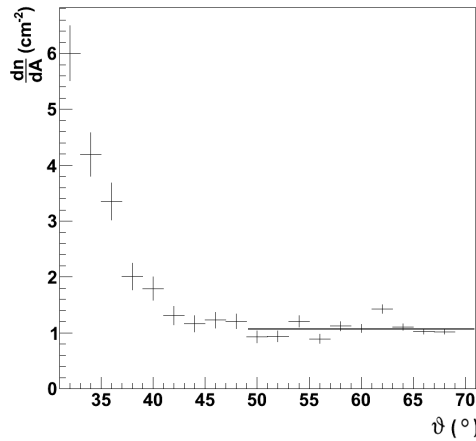
background dominates the signal from the scattered particles. An example is shown in Fig. 7.13(a).

The contribution of the Coulomb-scattered protons to the data is calculated with the help of Geant4. A high statistic simulation run was started with the program *slap*, where the hadronic interactions were switched off, so that the angular distribution is only given by the multiple-scattering protons. The results were scaled down to match the particle rate of each measurement and subtracted from the data.

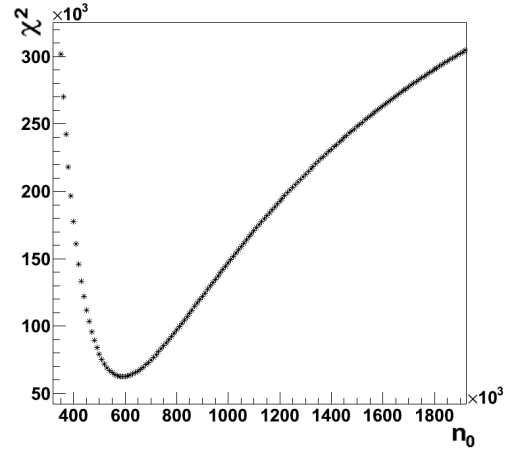
The number of the protons scattered by hadronic interaction is $n_{\text{hadronic}} = n_{\text{signal}} - n_{\text{cr39}} - n_c$ where n_{cr39} is the background level obtained by the fit, which is the dominant part of the background, and n_c the number of the Coulomb-scattered protons, obtained by the simulation. The statistical error of the track density after the background corrections is then given by

$$\left(\Delta \frac{n}{A}\right)_{\text{stat}} = \sqrt{\left(\frac{\sqrt{n}}{A}\right)^2 + 2 \cdot \left(\frac{\sqrt{n_{\text{cr39}}}}{A}\right)^2 + 2 \cdot \left(\frac{\sqrt{n_c}}{A}\right)^2}.$$

After this, the track density is converted to the number of protons per solid angle and the cross section is calculated according to Eq. (7.1) using the number of incident protons n_0 . This is compared to the available data from Cologne for a vertex energy of 3.3 MeV. Again the χ^2 between the two data sets is calculated for a range of n_0 and the minimum of the χ^2 distribution is determined, like it is depicted in Fig. 7.13(b).



(a) Raw data of a measurement with χ^2 fit for the estimation of the background level of the track density



(b) χ^2 distribution with a minimum at $n_0 = 580000$

Figure 7.13.: The diagrams for (a) the background estimation and (b) the estimation of n_0 are shown as an example in case of the measurement with shot number 3.

7. Spin polarization measurement

This procedure was performed for each shot individually, Fig. 7.14 shows the cross sections for each shot after the adjustment of n_0 by the χ^2 method and in Fig. 7.15 the calculated number of protons in the range of 2.8 to 3.5 MeV are compared. It can be seen that the estimation with the help of the RCF detectors is systematically higher. In case of the first shot the difference between both calculations is exceptionally high. This measurement was therefore excluded from the estimation of the cross section .

For both methods the number of protons $n_{2.8-3.5}$ in the energy range between 2.8 and 3.5 MeV that are expected to pass the aperture of the first collimator and arrive at the silicon target are given in Table 7.2. Figure 7.16 shows the comparison of

Table 7.2.: nr: shot number, n_{RCF} : number of incoming protons obtained from the RCF detectors, n_{CR39} : number of incoming protons obtained from the CR-39 detectors

nr	n_{RCF}	n_{CR39}
1	$880 \cdot 10^3 \pm 112 \cdot 10^3$	$260 \cdot 10^3$
2	$683 \cdot 10^3 \pm 195 \cdot 10^3$	$480 \cdot 10^3$
3	$880 \cdot 10^3 \pm 220 \cdot 10^3$	$840 \cdot 10^3$
4	$520 \cdot 10^3 \pm 188 \cdot 10^3$	$620 \cdot 10^3$
5	$260 \cdot 10^3 \pm 92 \cdot 10^3$	$220 \cdot 10^3$
6	$520 \cdot 10^3 \pm 188 \cdot 10^3$	$370 \cdot 10^3$

the Cologne data with the cross section that was averaged over five shots. Here, the data were not normalized to the Cologne cross section but rather the information on the particle fluxes obtained from the RCF detectors were used. The number of protons tends to be overestimated, however, this is well within the systematical error of approx. 20% from Table 7.2.

The most likely explanation for the strong deviation at an angle of 40° is, the high and irregular background level combined with the low statistic of the measurement.

7.3.6. Azimuthal angle asymmetries

For the estimation of the proton polarization the distribution of the differential cross section along the azimuth angle ϕ is obtained, which follows the function:

$$f(\phi) = \left(\frac{d\sigma}{d\Omega} \right)_0 \cdot (1 + AP \cdot \cos(\phi + \phi_0)) . \quad (7.2)$$

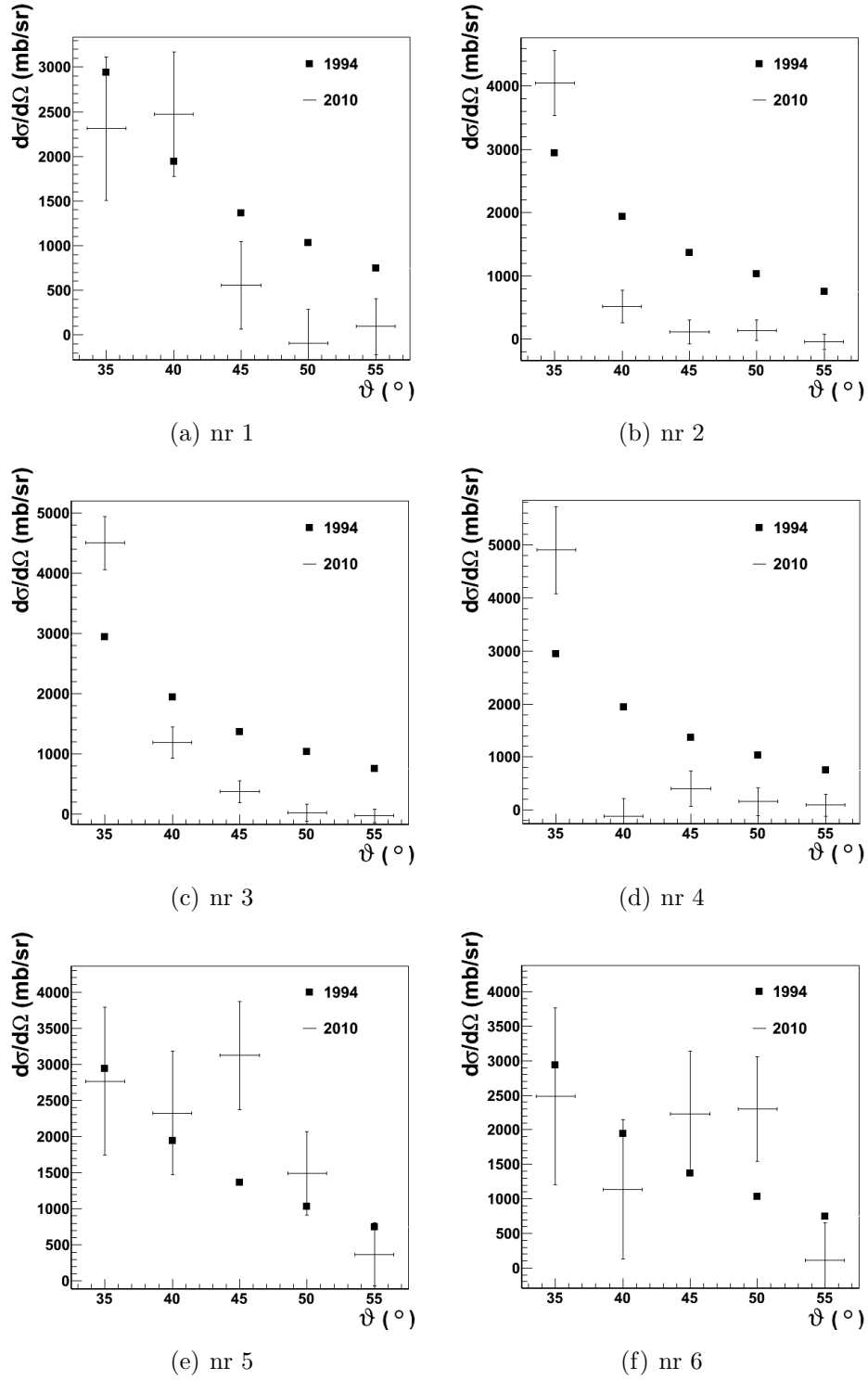


Figure 7.14.: Cross sections in dependence of the scattering angle ϑ in comparison to the Cologne data (1994) for six different shots.

7. Spin polarization measurement

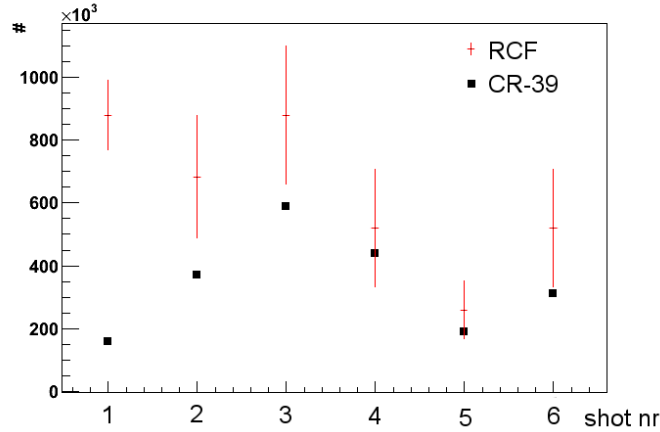


Figure 7.15.: Comparison of the numbers of incoming protons n_0 obtained by the RCF and CR-39 method, respectively.

The cross section of the unpolarized case $(d\sigma/d\Omega)_0$ is multiplied by a cosine term, which includes the polarization P , the analyzing power A and a phase shift ϕ_0 as parameters. At scattering angles of 60° and more, the analyzing power runs through a minimum at 2.9 MeV, see Fig. 4.4. However, these data points cannot be used since the signal-to-background ratio drops below one already at angles of approx. 40° to 45° , as seen in Fig. 7.13(a). The analyzing powers for scattering angles ϑ of 35° and 40° are shown in Fig. 7.17. The amount of data in case of 35° is very scarce and the absolute value of the analyzing power is rather small. By comparing the plots of both scattering angles and under the assumption, that the shape of the distribution is similar, one may assume that the analyzing power follows rather the dotted line indicated in the image, than the interpolation.

Therefore, the analyzing power in this region is assumed to be approx. 0.1. For a scattering angle of 40° the analyzing power changes the sign at approx. 3.3 MeV, while remaining relatively constant for lower energies and energies above 3.35 MeV. Therefore, it is useful to divide the data in two sets, depending on the vertex energy of the proton for the analysis of the data around 40° .

For several reasons some shots were rejected from the estimation of the asymmetries: if the background level exceeds the signal even for angles of less than 40° , if it was not possible to reliably determine the center of the angular distribution and if more than one third of the detector area had to be excluded from the analysis. For the remaining four measurements Fig. 7.18 shows the cross section in dependence of the azimuth angle ϕ for a scattering-angle range of the of 31° to 35° . The data was fitted with a constant $(d\sigma/d\Omega)_{const}$ as well as with the function in Eq. (7.2). In two of the four cases (shots nr. 1 and 5) the angular distribution is obviously compatible with a constant distribution. Table 7.3 summarizes the parameters obtained by the

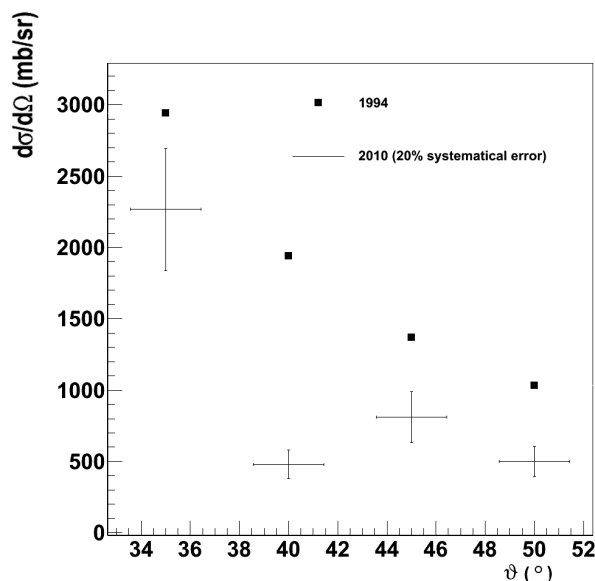


Figure 7.16.: Comparison of the average over 5 measurements from the laser data (2010) with the Cologne data (1994).

fit and the values of χ^2 for both, the fit with the constant functions and the cosine. The asymmetry in measurement nr. 6 is caused by the data point at $\phi = 315^\circ$. In

Table 7.3.: Fitted parameters and χ^2 for a constant and the cosine term for an angular range of $31^\circ - 35^\circ$.

nr	$(\frac{d\sigma}{d\Omega})_{const}$ (mb/sr)	$(\frac{d\sigma}{d\Omega})_0$ (mb/sr)	$ AP $	ϕ_0	$\chi^2_{constant}$	χ^2_{cos}
1	156 ± 66	161 ± 70	0.68 ± 0.62	-1.2	2.2	0.7
3	2822 ± 415	3621 ± 473	0.588 ± 0.15	1	14	1.4
5	1046 ± 385	1071 ± 386	0.61 ± 0.57	-1.66	1.7	0.4
6	204 ± 132	298 ± 147	1 ± 0.66	0.88	2.94	0.67

this measurement the signal to background ratio was disadvantageous and the value of the unpolarized cross section not in good agreement with the expectation.

Only in case of measurement number 3 a statistically significant asymmetry is observed. It is possible to analyze the angular region around $\vartheta \approx 40^\circ$. The data of the angular distribution was divided in the two energy regions below and above 3.3 MeV. If a polarization of the beam causes the asymmetry it is expected that the cosine functions of both distributions are phase-shifted by π due to the change of sign in A and the amplitude should be approximately of the same magnitude.

Figure 7.19(a) and 7.19(b) show the angular distributions for both sets of data and Table 7.4 the fit parameters and χ^2 . For Energies below 3.3 MeV the distribution is

7. Spin polarization measurement

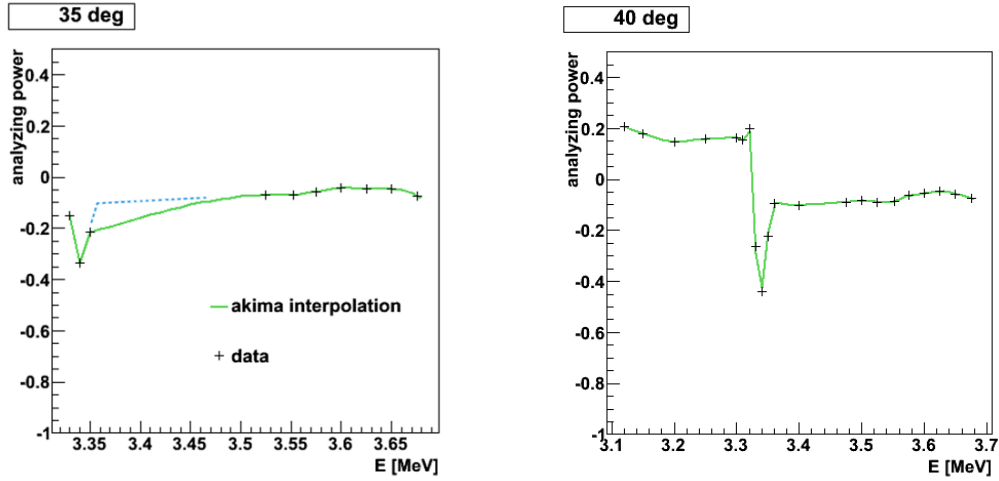


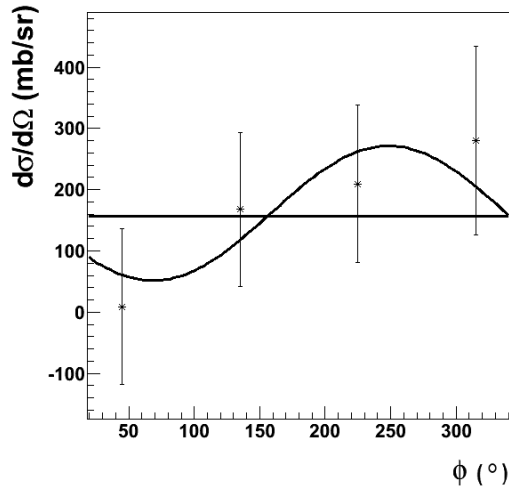
Figure 7.17.: Analyzing powers for 35° and 45° [49].

in good agreement with the constant function. The asymmetry seems not to change the sign between the two sets of data, the difference between the two values of ϕ_0 is only 0.9. If the obtained value for AP in the energy range of more than 3.3 MeV were taken at face value, with an assumed analyzing power of only 0.2 this would indicate a strong polarization. Therefore, it is necessary to clarify this possibility with additional data of higher statistical accuracy at a scattering angle of 60° where the analyzing power amounts to 0.8.

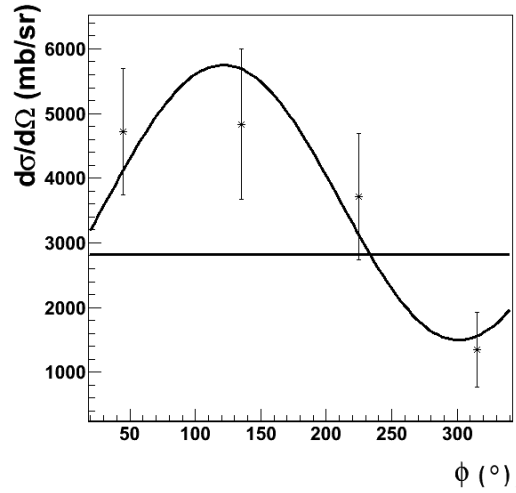
Table 7.4.: Fitted parameters and χ^2 for the constant and the cosine function for an angular range of $35^\circ - 45^\circ$.

energy	$\left(\frac{d\sigma}{d\Omega}\right)_{const}$ (mb/sr)	$\left(\frac{d\sigma}{d\Omega}\right)_0$ (mb/sr)	$ AP $	ϕ_0	$\chi^2_{constant}$	χ^2_{cos}
< 3.3 MeV	1135 ± 344	1200 ± 356	0.3 ± 0.4	0.3	1.0	0.49
> 3.3 MeV	959 ± 305	1329 ± 343	0.84 ± 0.32	1.2	6	0.02

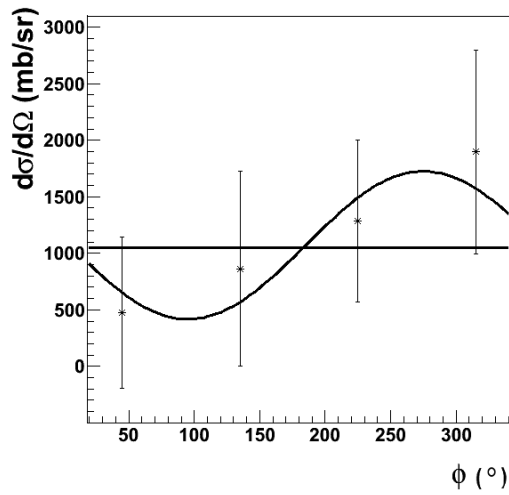
Consequently, the apparent asymmetry in the data is probably not caused by a polarization effect of the protons, but rather by systematical errors of the measurement. Note, however, that the interpretation is hindered by the poor statistical accuracy of the data. If the asymmetry were caused by a geometrical contortion, the amplitude of the asymmetry is not expected to change when a different range of track diameters is selected. The deviation from the constant function has therefore to be ascribed to the poor ratio between signal and background and the inhomogeneity of the background on the CR-39 detectors. Since every CR-39 detector can be used only once it is not possible to obtain a precise background pattern for each mea-



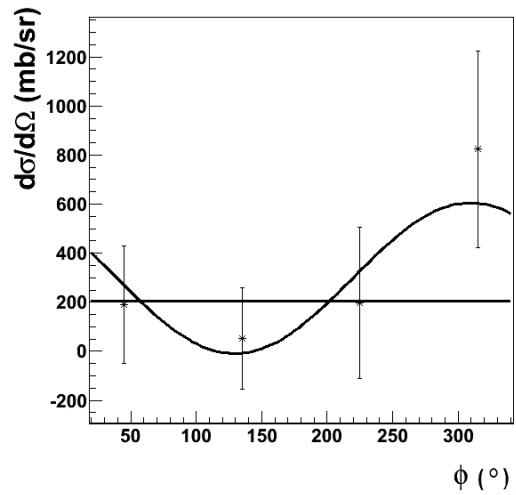
(a) nr 1



(b) nr 3



(c) nr 5



(d) nr 6

Figure 7.18.: Asymmetries in the angular region of $31^\circ - 35^\circ$ for four different shots.

7. Spin polarization measurement

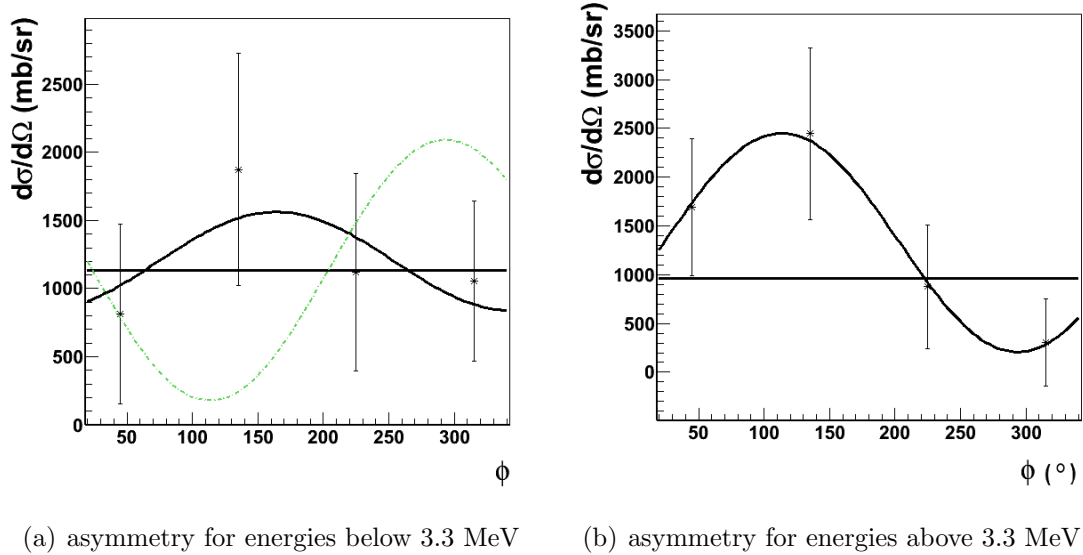


Figure 7.19.: Asymmetries in case of shot nr 3 for an angular range of $35^\circ < \vartheta < 45^\circ$.

surement, only the overall background level can be determined. If the fluctuations on the CR-39 plates exceed the signal false asymmetries can occur. Also, strong fluctuations between single shots are not surprising, since the angular distribution is not well reproducible from one shot to the other.

7.4. Conclusion

The cross section of the hadronic interaction was measured, albeit with high systematical uncertainties. Our data are in reasonable agreement with the data provided by the University of Cologne. In the first measurement no indication of beam polarization could be detected. The measurements were characterized by low particle rates in combination with high and irregular background. Systematical errors of the estimation of cross section and polarization can be ascribed to uncertainties of the background correction and fluctuations of the track density on the detectors. It was shown that false asymmetries, created by fluctuations in the background level of the track density can successfully be identified by comparison of two data sets of different energy ranges at a scattering angle of 40° .

For a quantitative determination of the polarization a better signal to background ration would be required.

8. Summary and outlook

In the first part of this thesis the influence of electromagnetic fields in a laser-generated plasma on the particle trajectories has been studied by simulations. A Particle-in-Cell code is used to model the interaction of a high intense short laser pulse with a gold foil target. The result is that no spatial separation of protons with different spin states and, therefore, no polarization build-up of the generated proton beams is expected for the particular choice of input parameters, which resemble the boundary conditions of our first experiments.

In the main part of this thesis, a method to measure the polarization of laser-generated proton beams has been developed. A secondary scattering target is used that exploits the dependence of nuclear scattering on the spin direction of the proton beam. As the most suitable scattering material silicon has been chosen. Experimental prestudies to obtain the energy spectrum of the protons have been carried out for which a magnetic spectrometer has been designed and built. With the help of Monte-Carlo simulations and using the obtained energy spectrum the experimental setup for the measurement of the polarization has been designed and optimized, and the procedures for the data analysis have been developed. Since the proton beams are expected to be unpolarized, a null-experiment has been carried out at the Düsseldorf ARCturus Laser Facility in which the feasibility of the method has been demonstrated.

As a short-term outlook a subsequent measurement with higher particle rates was carried out in Nov. 2010. These data is currently being analysed. The energy of the laser pulse was increased to 1.9 J, which boosted the proton rates by approximately an order of magnitude. Additionally, fine tuning of the experimental setup has been made and the CR-39 detectors have been pre-etched to reduce the background noise. From these data unambiguous statements about the degree of polarization of the laser-produced proton beam for this particular acceleration scheme (TNSA) can be expected. If one were able to verify the faint indication for beam polarization that has been seen in a single shot during the first measurement campaign, new light might be shed on the long-standing discussion whether the Stern-Gerlach effect is observable for charged particles.

Long-term plans include the study of ions from gas jet targets. In the underdense plasmas, produced in a gas jet the magnetic fields and their gradients extend further longitudinally than at the solid targets, which could lead to a stronger polarization-

8. Summary and outlook

dependent deflection of the particles.

Furthermore there is the possibility to use pre-polarized ^3He as target material. Acceleration of α particles from ^4He gas jet targets have already been observed [76], which is expected to work just as well for ^3He . This isotope can be polarized as a gas at room temperature with polarization relaxation times of days, since the coupling of the spins of the two valence electrons restrains the relaxation caused by collisions. Currently, no polarized sources for ^3He ions are available, since during the usual ionization process the electrons are removed consecutively, leaving an intermediate ion with a single electron, which reduces the relaxation time and destroys the nuclear spin polarization. The strong electric fields of a high intense laser, however, might be able to remove the two electrons within a ps or less, sustaining the nuclear spin during the acceleration process.

Bibliography

- [1] M. Borghesi, A. J. Mackinnon, D. H. Campbell, D. G. Hicks, S. Kar, P. K. Patel, D. Price, L. Romagnani, A. Schiavi, and O. Willi. Multi-MeV Proton Source Investigations in Ultraintense Laser-Foil Interactions. *Phys. Rev. Lett.*, 92(5):055003, Feb 2004.
- [2] T. Esirkepov, M. Borghesi, S. V. Bulanov, G. Mourou, and T. Tajima. Feasibility of using laser ion accelerators in proton therapy. *Plasma Phys. Rep.*, 28(5):453–456, Feb 2002.
- [3] M. Roth, T. E. Cowan, M. H. Key, S. P. Hatchett, C. Brown, W. Fountain, J. Johnson, D. M. Pennington, R. A. Snavely, S. C. Wilks, K. Yasuike, H. Ruhl, F. Pegoraro, S. V. Bulanov, E. M. Campbell, M. D. Perry, and H. Powell. Fast Ignition by Intense Laser-Accelerated Proton Beams. *Phys. Rev. Lett.*, 86(3):436–439, Jan 2001.
- [4] K. Kruschelnick et al. Ultra-high intensity laser-produced plasmas as a compact heavy ion injection source. *IEEE Trans. Plasma Sci.*, 28(4):1184–1189, Aug. 2000.
- [5] Bernhard Hidding (ILPP Düsseldorf). Private communication.
- [6] R. Wideröe. *Über ein neues Prinzip zur Herstellung hoher Spannungen*. PhD thesis, RWTH Aachen, 1927.
- [7] ILC. <http://www.linearcollider.org/>.
- [8] CLIC. <http://clic-study.web.cern.ch/clic-study/>.
- [9] S A Gaillard, K A Flippo, M E Lowenstern, J E Mucino, J M Rassuchine, D C Gautier, J Workman, and T E Cowan. Proton acceleration from ultrahigh-intensity short-pulse laser-matter interactions with cu micro-cone targets at an intrinsic 10^{-8} contrast. *Journal of Physics: Conference Series*, 244(2):022034, 2010.
- [10] W Gerlach and O. Stern. Der experimentelle Nachweis der Richtungsquantelung im Magnetfeld. *Z. Phys. A Hadrons and Nuclei*, 9(1):349–352, 1922.

Bibliography

- [11] B. M. Garraway and S. Stenholm. Does a flying electron spin? *Contemporary Physics*, 43(3):147–160, 2002.
- [12] W. Pauli and S. Flügge. *Handbuch der Physik 5*. Springer-Verlag, 1958.
- [13] T.H. Maiman. Stimulated optical radiation in ruby. *Nature*, 187:309–371, 1960.
- [14] Gerard A. Mourou, Toshiki Tajima, and Sergei V. Bulanov. Optics in the relativistic regime. *Rev. Mod. Phys.*, 78(2):309–371, Apr 2006.
- [15] P. Gibbon. *Short Pulse Laser Interactions with Matter an Introduction*. Imperial College Press, 2005. ISBN: 1-86094-135-4.
- [16] H.A. Bethe and E.E. Salpeter. Quantum mechanics of one- and two-electron atoms. *Plenum, New York*, 1977.
- [17] L. V. Keldysh. Ionization in the field of a strong electromagnetic wave. *Sov. Phys. JETP*, 20:1307, 1965.
- [18] A. M. Perelomov, V. S. Popov, and M. V. Terentev. Ionization of atoms in an alternating electric field I. *Sov. Phys. JETP*, 23:924, 1966.
- [19] A. M. Perelomov, V. S. Popov, and M. V. Terentev. Ionization of atoms in an alternating electric field II. *Sov. Phys. JETP*, 24:207, 1967.
- [20] R.Jung. *Laser-plasma interaction with ultrashort laser pulses*. PhD thesis, Heinrich Heine Universität Düsseldorf, 2007.
- [21] M. V. Ammosov, N. B. Delone, and V. P. Krainov. Tunnel ionization of complex atoms and of atomic ions in an alternating electromagnetic field. *Sov. Phys. JETP*, 64:1191–1194, 1986.
- [22] D. Bauer, P. Mulser, and W. H. Steeb. Relativistic ponderomotive force, uphill acceleration, and transition to chaos. *Phys. Rev. Lett.*, 75(25):4622–4625, Dec 1995.
- [23] Brice Quesnel and Patrick Mora. Theory and simulation of the interaction of ultraintense laser pulses with electrons in vacuum. *Phys. Rev. Lett.*, 58:3719, 1998.
- [24] F. Brunel. Not-so-resonant, resonant absorption. *Phys. Rev. Lett.*, 59(1):52–55, Jul 1987.
- [25] W. L. Kruer and K Estabrook. $J \times b$ heating by very intense laser light. *Phys. Fluids*, 28:430–432, Jul 1985.

- [26] B. Qiao, M. Zepf, M. Borghesi, B. Dromey, M. Geissler, A. Karmakar, and P. Gibbon. Radiation-pressure acceleration of ion beams from nanofoil targets: The leaky light-sail regime. *Phys. Rev. Lett.*, 105(15):155002, Oct 2010.
- [27] P. Mora. Plasma expansion into a vacuum. *Phys. Rev. Lett.*, 90(18):185002, May 2003.
- [28] P. Mora. Thin-foil expansion into a vacuum. *Phys. Rev. E*, 72(5):056401, Nov 2005.
- [29] H. Schworer, S. Pfotenhauer, O. Jäckel, K.-U. Amthor, B. Liesfeld, W. Ziegler, R. Sauerbrey, K. W. D. Ledingham, and T. Esirkepov. Laser-plasma acceleration of quasi-monoenergetic protons from microstructured targets. *Nature*, 439, 2006.
- [30] K. Uhlenbeck S. Goudsmit. *Naturwiss.*, 54, (1925) 593.
- [31] I. I. Rabi, S. Millman, P. Kusch, and J. R. Zacharias. The Molecular Beam Resonance Method for Measuring Nuclear Magnetic Moments. The Magnetic Moments of ${}_3\text{Li}^6$, ${}_3\text{Li}^7$ and ${}_9\text{F}^{19}$. *Phys. Rev.*, 55(6):526–535, Mar 1939.
- [32] P. Kusch, S. Millman, and I. I. Rabi. The Nuclear Magnetic Moments of N^{14} , Na^{23} , K^{39} and Cs^{133} . *Phys. Rev.*, 55(12):1176–1181, Jun 1939.
- [33] Lincoln Wolfenstein. Theory of proposed reactions involving polarized protons. *Phys. Rev.*, 75(11):1664–1674, Jun 1949.
- [34] M. Goeppert Mayer and J. H. D. Jensen. *Elementary Theory of Nuclear Shell Structure*, John Wiley u. Sons, Inc., New York; Chapman u. Hall, Ltd., London 1955. 1. Aufl. WILEY-VCH Verlag GmbH, 1956.
- [35] I. I. Rabi G. Breit. *Phys. Rev.*, 38, (1931) 2082.
- [36] Willis E. Lamb and Robert C. Retherford. Fine structure of the hydrogen atom. part i. *Phys. Rev.*, 79(4):549–572, Aug 1950.
- [37] G. Clausnitzer, R. Fleischmann, and H. Schopper. Erzeugung eines Wasserstoffatomstrahles mit gleichgerichteten Kernspins. *Z. Phys. A Hadrons and Nuclei*, 144, 1956.
- [38] H. Rudin, H.R. Stiebel, E. Baumgartner, L. Brown, and Huber. P. *Helv. Phys. Act.*, 34(58), 1961.

Bibliography

- [39] H. Dutz, R. Gehring, S. Goertz, D. Krämer, W. Meyer, R. Paulsen, L.A. Reichertz, G. Reicherz, W. Thiel, A. Thomas, and J. Weber. The new bonn frozen spin target for experiments with real photons. *Nucl. Instr. and Meth. in Phys. Res. Section A: Accelerators, Spectrometers, Detectors and Associated Equipment*, 340(2):272 – 277, 1994.
- [40] A.Imig. *Polarisationstransfer in der $D(d,p)^3H$ -Reaktion — Implikationen für Astrophysik und Reaktionsmechanismus*. PhD thesis, Universität zu Köln, 2005.
- [41] B. Frois, J. Birchall, R. Lamontagne, R. Roy, and R.J. Slobodrian. A high efficiency proton polarimeter with silicon detector analyser. *Nucl. Instr. and Meth.*, 96(3):431 – 436, 1971.
- [42] B. M. Garraway and S. Stenholm. Observing the spin of a free electron. *Phys. Rev. A*, 60(1):63–79, Jul 1999.
- [43] Paul Gibbon (JSC Jülich). Private communication.
- [44] P. Gibbon, A. Andreev, E. Lefebvre, G. Bonnaud, H. Ruhl, J. Delettrez, and A. R. Bell. Calibration of one-dimensional boosted kinetic codes for modeling high-intensity laser–solid interactions. *Physics of Plasmas*, 6(3):947–953, 1999.
- [45] M.Keldenich. Parallelisierung eines eindimensionalen Particle in Cell Codes mittels OpenMP. Master’s thesis, Fachhochschule Aachen, 2009.
- [46] Paul Gibbon and A. R. Bell. Collisionless absorption in sharp-edged plasmas. *Phys. Rev. Lett.*, 68(10):1535–1538, Mar 1992.
- [47] P. Schwandt, T. B. Clegg, and W. Haeberli. Polarization measurements and phase shifts for $p - {}^4He$ scattering between 3 and 18 MeV. *Nuclear Physics A*, 163(2):432 – 448, 1971.
- [48] Hans-Otto Meyer (Bloomington USA). Private communication.
- [49] B. Becker. data of a measurement of A_y and $\frac{d\sigma}{d\Omega}$ for Si(p, p)Si, unpublished data, Institut für Kernphysik, Universität zu Köln, 1994.
- [50] F. Sperisen, W. Grüebler, V. König, P.A. Schmelzbach, K. Elsener, B. Jenny, and C. Schweizer. A set of high efficiency proton polarimeters for proton energies between 2 and 20 MeV. *Nucl. Instr. and Meth. in Phys. Res.*, 190(2):301 – 307, 1981.
- [51] GEANT4 COLLABORATION. <http://geant4.web.cern.ch>.

- [52] Q. Zhang. Entwicklung eines ortsempfindlichen Detektors samt Ausleseelektronik zur Untersuchung laserinduzierter Beschleunigung. Diplom thesis, RWTH Aachen, 2009.
- [53] Borghesi M., Schiavi A., Campbell D.H., Haines M.G., Willi O., MacKinnon A.J., Gizzi L.A., Galimberti M., Clarke R.J., and Ruhl H. Proton imaging: a diagnostic for inertial confinement fusion/fast ignitor studies. *Plasma Physics and Controlled Fusion*, 43:267–276(10), 2001.
- [54] M. Borghesi, A. Schiavi, D. H. Campbell, M. G. Haines, O. Willi, A. J. Mackinnon, P. Patel, M. Galimberti, and L. A. Gizzi. Proton imaging detection of transient electromagnetic fields in laser-plasma interactions (invited). *Review of Scientific Instruments*, 74(3):1688 –1693, mar. 2003.
- [55] W. L. McLaughlin, A. Miller, S. Fidan, K. Pejtersen, and W. Batsberg Pedersen. Radiochromic plastic films for accurate measurement of radiation absorbed dose and dose distributions. *Radiation Physics and Chemistry (1977)*, 10(2):119 – 127, 1977.
- [56] T.Toncian. *Ultra fast laser driven micro-lens to focus and energy select MeV protons*. PhD thesis, Heinrich Heine Universität Düsseldorf, 2008.
- [57] Wolfgang Birkholz, Carola Winkler, and Hartmut Baumbach. Neutron sensitivity of CR-39 SSNTD. *Int. J. of Radiation Applications and Instrumentation. Part D. Nuclear Tracks and Radiation Measurements*, 19(1-4):453 – 456, 1991.
- [58] R. L. Fleischer, P. B. Price, and R. M. Walker. Ion explosion spike mechanism for formation of charged particle tracks in solids. *Journal of Applied Physics*, 36(11):3645 –3652, nov. 1965.
- [59] R.L. Fleischer, P.B. Price, and R.M. Walker. *Nuclear tracks in solids*. 1975.
- [60] R.P. Henke and E.V. Benton. On geometry of tracks in dielectric nuclear track detectors. *Nucl. Instr. and Meth.*, 97(3):483 – 489, 1971.
- [61] J. S. Yadav. Charged particle identification using CR-39(DOP) detectors. *Radiation Measurements*, 24(2):115 – 128, 1995.
- [62] H. S. Virk and A. K. Srivastava. Modification of optical, chemical and structural response of CR-39 polymer by 50 MeV lithium ion irradiation. *Radiation Measurements*, 34(1-6):65 – 67, 2001.
- [63] M.Blecher. Quantitative Analyse von Laser-produzierten Protonen. Bachelorarbeit, Heinrich-Heine-Universität Düsseldorf, 2009.

Bibliography

- [64] RANA Mukhtar A. and A QURESHI I. E. Studies of CR-39 etch rates. 198(3-4):129–134, 2002.
- [65] Dörschel B. and Fülle D. and Hartmann H. and Hermsdorf D. and Kadner and K. and Radlach Ch. Measurement of Track Parameters and Etch Rates in Proton-Irradiated CR-39 Detectors and Simulation of Neutron Dosimeter Responses. *Radiat. Protect. Dosim.*, 69:267 – 274, 1997.
- [66] C.C. Blatchley, Peter D. Zimmerman, O.E. Pruet, P. Sioshansi, and F. Wittel. Anomalous track development in CR-39: Effects of gamma irradiation. *Nucl. Instr. and Meth. in Phys. Res.*, 201(2-3):535 – 537, 1982.
- [67] A. H. Khayrat and S. A. Durrani. The effect of UV exposure on the track and bulk etching rates in different CR-39 plastics. *Radiation Measurements*, 25(1-4):163 – 164, 1995.
- [68] F. Abu-Jarad, M.A. Islam, I. Abu-Abdoun, and M.A. Khan. Ultraviolet and laser irradiation effects on various batches of CR-39. *International Journal of Radiation Applications and Instrumentation. Part D. Nuclear Tracks and Radiation Measurements*, 19(1-4):135 – 138, 1991.
- [69] Sangeeta Prasher and Surinder Singh. The effect of infrared radiation on etching characteristics of CR-39 plastic track recorder. *Radiation Measurements*, 36(1-6):105 – 106, 2003. Proceedings of the 21st International Conference on Nuclear Tracks in Solids.
- [70] *TASLIMAGE Radon and Neutron dosimetry System. A complete system for etching, scanning and analysing TASTRAK plastic nuclear detector*, <http://www.tasl.co.uk>.
- [71] R. Mishra, C. Orlando, L. Tommasino, S. Tonnarini, and R. Trevisi. A better understanding of the background of CR-39 detectors. *Radiation Measurements*, 40(2-6):325 – 328, 2005. Proceedings of the 22nd International Conference on Nuclear Tracks in Solids.
- [72] Ralph Jung (ILPP Düsseldorf). Private communication.
- [73] O. Willi et al. Particle and X-ray generation by irradiation of gaseous and solid targets with a 100 TW laser pulse. *Plasma Physics and Controlled Fusion*, 51(12):124049 (7pp), 2009.
- [74] T. Menniken. Simulation von Teilchentrajektorien in starken Magnetfeldern laser-induzierter Plasmen. Diploma thesis, Fachhochschule Aachen, 2010.

- [75] M. Händel. Computergestützte Weiterentwicklung eines Protonen-Transferpolarimeters für niedrige Energien. Diploma thesis, Universität zu Köln, 1996.
- [76] L. Willingale, S. P. D. Mangles, P. M. Nilson, R. J. Clarke, A. E. Dangor, M. C. Kaluza, S. Karsch, K. L. Lancaster, W. B. Mori, Z. Najmudin, J. Schreiber, A. G. R. Thomas, M. S. Wei, and K. Krushelnick. Collimated multi-mev ion beams from high-intensity laser interactions with underdense plasma. *Phys. Rev. Lett.*, 96(24):245002, Jun 2006.
- [77] A. Imig. Polarisationstransfer in der $D(d,p)^3H$ -Reaktion — Weiterentwicklung und Einsatz eines Transferpolarimeters. Diploma thesis, Universität zu Köln, 1996.
- [78] D. Fick. Einführung in die Kernphysik mit polarisierten Teilchen, 1991.
- [79] R. Engels. *Entwicklung eines universellen Lambshift-Polarimeters für polarisierte Atomstrahl-Targets wie an ANKE/COSY*. PhD thesis, Universität zu Köln, 2002.

A. Measurements April 2010

Table A.1.: Overview of all 16 shots of the measurement. The dose on the first layer of the RCF stack is given and the number of protons that are expected to pass the apertures based on this. Note that the numbering differs from Sect. 7, the corresponding shot numbers are given in the comment column.

nr	dose on 1st layer (Gy)	$n_{protons}(2.8 - 3.6\text{MeV})$ in setup	comment
1			spectrometer measurement
2	400 ± 50	$880 \cdot 10^3 \pm 112 \cdot 10^3$	nr 1 in Sect. 7
3	350 ± 100	$683 \cdot 10^3 \pm 195 \cdot 10^3$	nr 2 in Sect. 7
4	600 ± 300	$132 \cdot 10^3 \pm 660 \cdot 10^3$	
5	-	-	faint signal, no silicon target
6	500 ± 100	$1100 \cdot 10^3 \pm 220 \cdot 10^3$	no silicon target
7	300 ± 100	$660 \cdot 10^3 \pm 220 \cdot 10^3$	
8	500 ± 100	$880 \cdot 10^3 \pm 220 \cdot 10^3$	nr 3 in Sect. 7
9	100 ± 50	$220 \cdot 10^3 \pm 112 \cdot 10^3$	
10	300 ± 100	$660 \cdot 10^3 \pm 220 \cdot 10^3$	
11	200 ± 100	$520 \cdot 10^3 \pm 188 \cdot 10^3$	nr 4 in Sect. 7
12	100 ± 50	$260 \cdot 10^3 \pm 92 \cdot 10^3$	nr 5 in Sect. 7
13	200 ± 100	$520 \cdot 10^3 \pm 188 \cdot 10^3$	nr 6 in Sect. 7
14	100 ± 50	$260 \cdot 10^3 \pm 92 \cdot 10^3$	
15	80 ± 40	$208 \cdot 10^3 \pm 76 \cdot 10^3$	no silicon target
16	150 ± 50	$388 \cdot 10^3 \pm 92 \cdot 10^3$	no silicon target

Danksagung

Zum Schluss möchte ich mich auf diesem Weg bei allen bedanken, die zum Gelingen dieser Arbeit beigetragen haben:

Bei Prof. Dr. Rudolf Maier bedanke ich mich dafür, dass er mir die Möglichkeit gegeben hat diese Arbeit am Institut für Kernphysik anzufertigen.

Dr. Markus Büscher möchte ich die interessante Aufgabenstellung, sowie für die Hilfs- und Diskussionsbereitschaft sagen: Vielen Dank, Chef.

Danke auch an Prof. Dr. Jan Jolie, der das Koreferat meiner Arbeit übernommen hat.

Herrn Prof. Dr. Oswald Willi möchte ich für die Möglichkeit danken, Experimente am ARCTurus Laser durchführen zu dürfen.

Ebenso bedanke ich mich bei allen Kollegen des Instituts für Kernphysik für die Zusammenarbeit, insbesondere natürlich bei den Mitgliedern der Laser-Beschleuniger-Gruppe: Dr. Andreas Lehrach, Ilhan Engin und Mohammad Hessian.

Dr. Paul Gibbon möchte ich für die Bereitstellung des PIC codes BOPS3.2 danken und auch Dr. Anupam Karmakar für die Hilfe bei der Anwendung.

Mein Dank gilt auch Monica und Dr. Toma Toncian, ohne die die Experimente nicht möglich gewesen wären, sowie allen weiteren Mitarbeitern am Institut für Laser und Plasmaphysik der Universität Düsseldorf vor allem Dr. Ralph Jung, Dr. Mirela Cerchez und Marco Swantusch.

Bei den Mitarbeitern der Werkstätten, sowohl des IKP als auch des ILPP, bedanke ich mich, vor allem bei Stefan Manderla für einige last-minute Anfertigungen und den Weckdienst morgens um sieben im Laserlabor.

Thomas Sagefka und Markus Küven, die sich vermutlich mehr als einmal die Finger an Todesmagneten geklemmt haben, bin ich für den Zusammenbau und die Vermessung des Spektrometers sehr dankbar.

Dr. Henner Ohm danke ich für Nachhilfe in Chemie und Thomas Krings für die praktische Hilfe im Labor.

Danke auch an Dr. Ralf Engels, der bei Fragen zum Thema Polarisation weiter geholfen hat.

Melanie und Patrick danke ich für das last-minute Korrekturlesen.

Schließlich gilt mein Dank meiner Familie und vor allem meinen Nichten und Neffen für die Motivation ("Nana, wann wirst Du denn jetzt Doktor...? ") und die konstruktiven Vorschläge (siehe Fig. A.1).

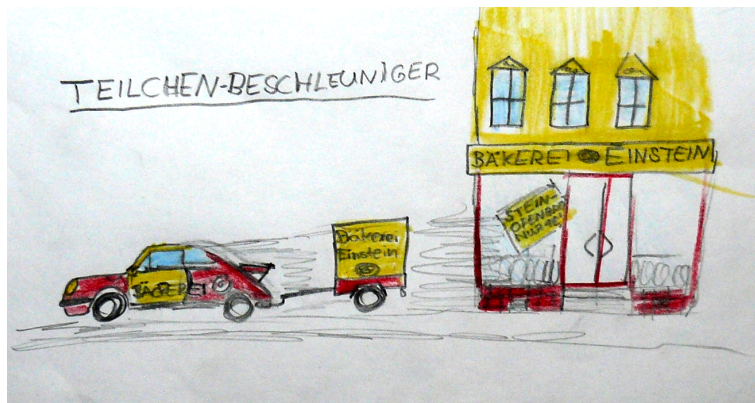


Figure A.1.: Teilchenbeschleuniger entworfen von Tim Raab

Von ganzem Herzen möchte ich mich besonders bei meiner Mutter Gerda Raab für ihre Unterstützung bedanken.

Erklärung

Ich versichere, daß ich die von mir vorgelegte Dissertation selbstständig angefertigt, die benutzten Quellen und Hilfsmittel vollständig angegeben und die Stellen der Arbeit — einschließlich Tabellen, Karten und Abbildungen —, die anderen Werken im Wortlaut oder dem Sinn nach entnommen sind, in jedem Einzelfall als Entlehnung kenntlich gemacht habe; daß diese Dissertation noch keiner anderen Fakultät oder Universität zur Prüfung vorgelegen hat; daß sie — abgesehen von unten angegebenen Teilpublikationen — noch nicht veröffentlicht worden ist sowie, daß ich eine solche Veröffentlichung vor Abschluß des Promotionsverfahrens nicht vornehmen werde.

Die Bestimmungen dieser Promotionsordnung sind mir bekannt. Die von mir vorgelegte Dissertation ist von Priv.-Doz. Dr Markus Büscher betreut worden.

Lebenslauf

Name: Raab
Vorname: Natascha
Geboren: 03.06.1981 in Bonn

Schulbildung:
1991 - 2000 Sankt-Adelheid-Gymnasium in Bonn
Juni 2000 Abitur

Studium:
Oktober 2000 Beginn des Physikstudiums an der RWTH Aachen
März 2006 Beginn der Diplomarbeit am 3. Physikalischen Institut B
der RWTH Aachen mit dem Thema: "Aufbau eines Teststandes
für das Triggersystem des Double Chooz Experiments"
März 2007 Abschluß der Diplomarbeit

Oktober 2007 Beginn der Promotion in Experimentalphysik
am Institut für Kernphysik des Forschungszentrums Jülich